![Skoltech logo]

Skolkovo Institute of Science and Technology

Skolkovo Institute of Science and Technology

VOLTAGE FEASIBILITY BOUNDARIES

Doctoral Thesis

by

MAZHAR ALI

DOCTORAL PROGRAM IN ENGINEERING SYSTEMS

Supervisor

Professor Janusz Bialek

Moscow 2019

© Mazhar Ali 2019.

Abstract

Modern power systems are facing a new grand challenge in the grid management due to an increase in electricity demand, imminent disturbances, and uncertainties associated with the distributed energy resources (DERs), like wind farms, photovoltaics, which can compromise the stability of the network. Such transformations in the grid have also made it difficult to validate the feasibility of an operating regime for power system security assessment. Therefore, power flow solution boundaries or feasibility boundaries must be considered for better security assessment. Also, to reduce the chance of disturbance, to maximize the power transfer and to take full advantage of transmission capabilities. Calculation of such voltage feasibility boundaries is a computationally challenging task linked to the nonlinear nature of the power flow equations, technological constraints, and complex structure of the grid. Calculations are also computationally intensive as the operating regime changes rapidly with time.

The mathematical framework in this thesis address this problem with an emphasis on the computational part. To calculate the power flow solution boundaries with a set of proposed algorithms that allow fast convergence, smaller computational burden along with ease of programming. The first part of the thesis introduces a novel modification referred here as "Transversality Enforced Newton Raphson" (TENR) to the conventional Newton-Raphson load flow solver, for faster computation of the points corresponding to the boundary of power flow space. A methodology for including technological constraints is also provided. The performance of the TENR algorithm is validated on several IEEE test networks. A comprehensive comparison is also presented with the algorithms proposed in the literature.

The latter part of the thesis extends the problem from just finding a point on the boundary to construct the 1-manifold curve and also 2-manifold surfaces in power injection space. An adaptive "Spherical Continuation" procedure is presented. The algorithm was further complemented with additional improvements to trace the boundary curve with good convergence, flexibility, and computational speed. A detailed numerical analysis was conducted to understand the complexity associated with the power flow feasibility boundaries. Numerical experiments also cover a wide range of practical scenarios.

Publications

1. **Ali, Mazhar**, Anatoly Dymarsky, and Konstantin Turitsyn. "Transversality Enforced Newton–Raphson Algorithm for Fast Calculation of Maximum Loadability." IET Generation, Transmission & Distribution 12, no. 8 (2017): 1729-1737.

2. **Ali, Mazhar**, Elena Gryazina, and Konstantin S. Turitsyn. "Fast Calculation of the Transfer Capability Margins." In 2019 IEEE Milan PowerTech, pp. 1-6. IEEE, 2019.

3. Sajjad Asefi, **Ali, Mazhar** , Elena Gryazina, "Optimal Energy Management for Off-Grid Hybrid System using Hybrid Optimization Technique." In 2019 IEEE PES Innovative Smart Grid Technologies Europe, Bucharest, Romania.

4. Ahmed, Tanvir, Mazhar Ali, and Dawar Awan. "Techno-Economic Study of Electricity Generation from Wind at Kallar-Kahar Region in Pakistan." In 2018 International Conference on Frontiers of Information Technology (FIT), pp. 275-280. IEEE, 2018.

5. **Ali, Mazhar**, Elena Gryazina, and Konstantin S. Turitsyn. "Methodology for Computation of Online Voltage Stability Assessment." In 2018 IEEE International Conference on Environment and Electrical Engineering and 2018 IEEE Industrial and Commercial Power Systems Europe (EEEIC/I&CPS Europe), pp. 1-5. IEEE, 2018.

6. **Ali, Mazhar**. "Computation of Loadability Limit in Power System based on Newton-Bisection Algorithm." In 2016 IEEE International Conference on Power System Technology (POWERCON), pp. 1-6. IEEE, 2016.

Acknowledgments

I would like to express my sincerest gratitude to Prof. Janusz Bialek, Prof. Elena Gryzina and Prof. Konstantin Turitsyn for their excellent academic guidance and support throughout this research work. I would also like to thank Prof. Anatoly Dymarsky for his help in publications and valuable theoretical suggestions. It was a prestigious opportunity for me to work under the supervision of these distinguished professors.

I wish to express my special thanks to my great friend Md Mahbubur Rahman, brother Muhammad Ali, and my Uncle Shahzad Ali who helped me throughout my doctoral studies. I would like to dedicate this thesis work to my parents Mahmood Ali and Abida Bibi, for their support, dedication, and understanding during this study.

Contents

List of Figures

List of Tables

Chapter 1

Introduction

This chapter provides a general description of power systems and a brief discussion of power system security assessment. It also covers the details on notable contributions from the past, research motivations, and composition of the thesis.

1.1 Power Systems History

Over the last century, the size of the power system has grown from fewer elements to a scale consisting of thousands of miles transmission lines, hundreds of generating units, with a substantial amount of several types of equipment to facilitate and maintain a secure operation [1, 2, 3].

Let us consider the architecture of a conventional power grid. The overall layout of the power system is outlined in Fig.1-1 [4]. The first block is the generation unit consisting of power plants that produce electrical energy from various options as mechanical, hydro, chemical, solar, wind, nuclear, and others. This electrical energy is transported to longer distances by the transformation into high-voltage electrical power. The second block is the transmission grid that carries the high voltage electrical power to long distances to the consumer units. Then finally, the distribution grid transforms this high voltage power into lower voltage levels suitable for commercial, residential, and industrial consumption [5]. Although an actual power system is much more complicated, the layout is somewhat similar to Fig.1-1. The
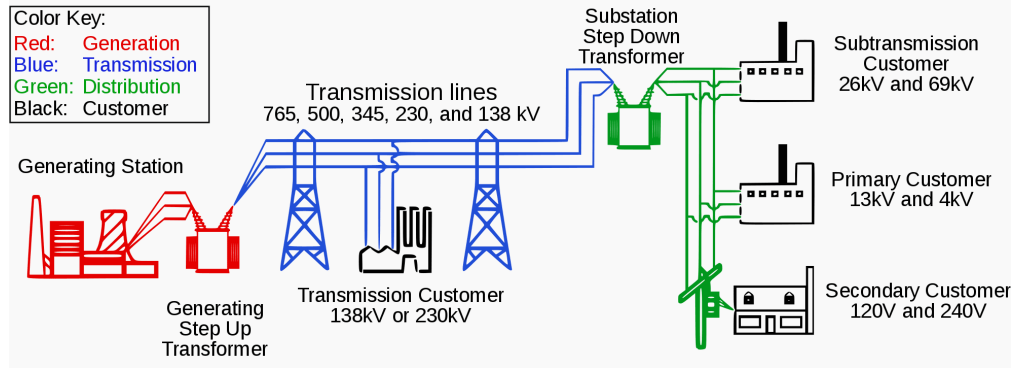
Figure 1-1: Electric power system layout.
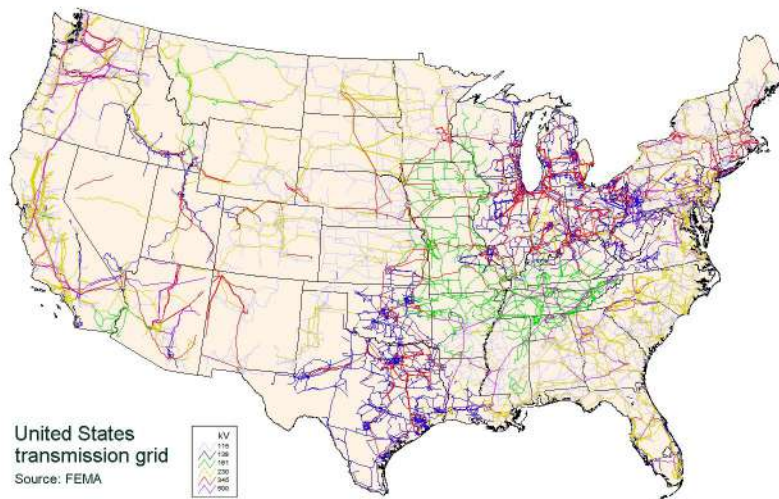
Figure 1-2: Transmission grid of the United States.

complexity and massive evolution of the power network is depicted in Fig.1-2, It shows a map of the current transmission grid for the United States [6]. It is fascinating to see such a massive transformation of the power network over the last century. The birth of the modern electric grid started precisely in 1882 by the Thomas Edison in the New-York City [7, 8]. Nevertheless, this grid had a limited capacity of only 250 hp (horsepower), with higher losses and inability to transfer power for long distances, it opened the possibility to a new bridge for electrification of cities, to countries, and even to continents. The credit for such a remarkable transformation of the modern grid goes to the work of Thomas Edison and Nikola Tesla and many other inventors of the 20th century, who laid the foundation for commercial use of electricity through an electric grid.

1.2 Power Systems Security Assessment

Power system security has become an important subject, as the modern power systems are going through several changes to suffice with the increase in demands and also to facilitate the integration of the distributed energy resources (DERs) like wind farms, photovoltaics, electric vehicles and other renewables in the grid [9, 10]. Although all these changes in the power system have assisted in the operations and markets, at the same time has raised grave concern for system security [11, 12]. In general, security assessment is described as the capability of the grid to maintain a stable operation after some imminent disturbance, such as changes in load, uncertainties with renewable generation, and outage of line or generation units [12]. The system security assessment is linked to the robustness of operating point or regime, which depends on the operational conditions as well as the contingent probability of disturbances [13, 12].

The secure and stable operation has always been a priority for the safe and economic prospect. During the period of the vertically integrated architecture of the grid, power systems were more secure and reliable due to several factors like governess by government bodies, integrated planning, which allowed a balance between growing demand and generation [12]. But in the last few decades, the complexity of the grid architecture and operation has increased, which made maintaining the stable operation of the grid a challenging task. Prominently, the recent major blackouts and similar electricity outage incidents observed in Asia, USA, and Europe (see Table.1.1) have elevated interest for better security assessment of the grid and need for more

Table 1.1: Summary for different blackouts.

No #	Locations	Year	Duration (hours)	Effected People (millions)
1	India	2012	48	620
2	Bangladesh	2014	10	150
3	USA, Canada	2003	72	55
4	Italy, Switzerland	2003	15	56

efficient computational techniques for security analysis as well.

In the subsequent discussion, we look at power system security analysis and the necessity for efficient computational tools.

1.2.1 Power System Security Analysis

Security analysis is crucial to determine the robustness of an operating point or regime for secure and economical operation. Transmission System Operator (TSO) performs the following tasks to assess the security of the grid. i) First, to determine how secure is the operating regime. ii) Secondly, to which degree security will be affected if the current regime changes in real-time, and finally iii) if an operating point is not secure, then what control action should be taken to make the system safe for operation [13, 12]. From the economic side, information about the robustness of an operating regime can assist in the energy trading agreements and distorting locational energy prices [13]. Therefore, the power system security analysis is not just critical from the security assessment but also assists in maintaining price stability.

Before we go further, it is crucial to understand how the robustness of an operating point is evaluated in terms of the feasible region of operation. Figure.1-3 shows a geometrical illustration for steady-state security assessment in $\lambda_1 - \lambda_2$ space (i.e., power injections or state-space). Different regions in Fig.1-3 represent the feasible injection in $\lambda_1 - \lambda_2$ with different technological or feasibility constraints (like voltage limits, active and reactive generation limits, and line thermal limits). In the feasible region, not just real solutions of power flows should exist, but the technological constraints are also valid [14].

Figure.1-3a describes the solvability region; it means outside this region there is no real solution to power flows exist. This boundary of the solvable region in Fig.1-3a is expressed as "stability or solvability boundary" [15, 16], which separates the real-valued solution of the power flows. While the Fig.1-3b also considers limits on voltage levels on load buses, we can see that this region is a bit smaller than the one in Fig.1-3a. The area described by Fig.1-3c also considers the active power generation limits along with solvability and constraint on voltage levels. Finally, the region in Fig.1-3d
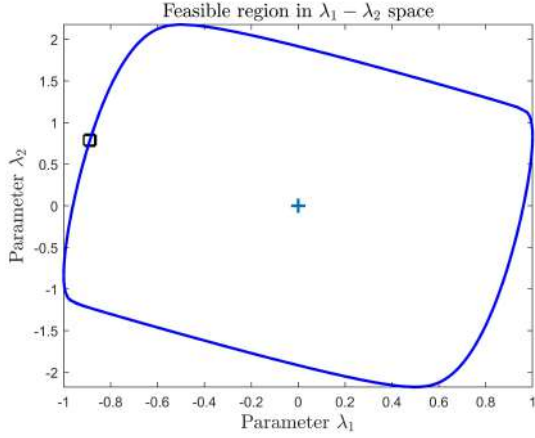
(a) Without any constraints.
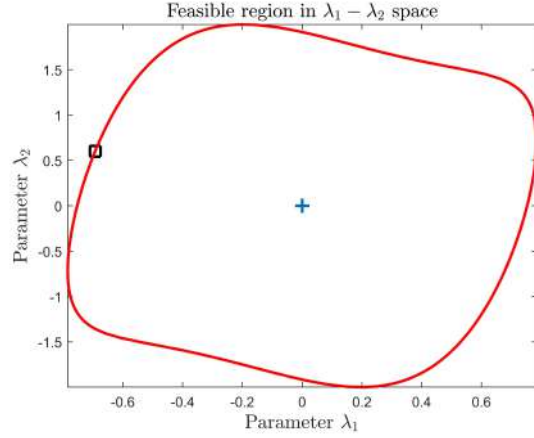
(b) Voltage magnitude constraints.
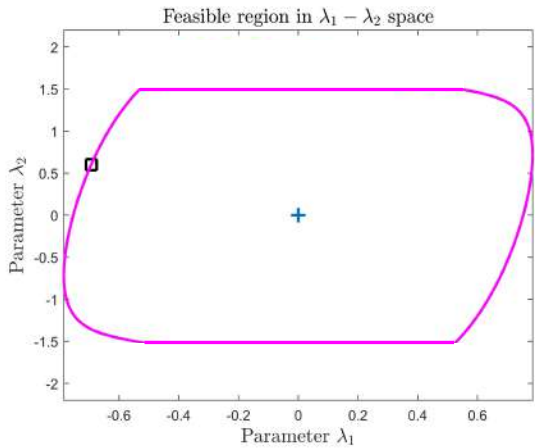
(c) Voltage & active generation constraints.
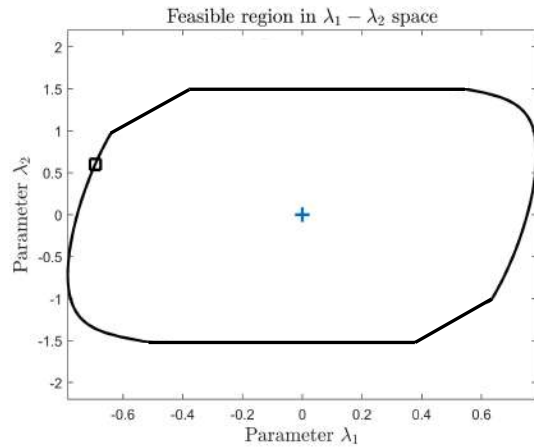
(d) All technological constraints.

Figure 1-3: Feasible region of operation in $\lambda_1 - \lambda_2$ space, in which the TSO can determines the security, maneuverability or required control actions to bring the operating regime back to the feasible domain.

describes a feasible region of operation in which all the technological limitations are considered with the condition on solvability as well.

It is interesting to see that with such information the TSO can determine, i) the degree of security for an operating point, ii) the acceptable maneuverability if it changes and, iii) can also decide what actions should be taken if the operating regime is violating some technological constraints or if it is outside the solvability domain. It is also clear from Fig.1-3 that with the addition of constraints, the structure of feasible region changes and becomes smaller.

5

The boundary that confines the feasible region in which not just real solution to power flows exist but also the operational or technological constraints are valid is referred to as "feasibility or voltage feasibility boundary" [14, 17]. The framework of this thesis studies the shape of voltage feasibility boundaries. Generally, such boundaries are convex [18, 19], but examples of non-convex boundaries are also presented in [13]. The work here contributes to the computational part as well and provides a detailed mathematical structure for determining the voltage feasibility boundaries with precision, speed and computational efficiency.

1.2.2 Computational Tools

The computational part of the power system has an important role to play toward its reliability and security assessment. The power flow analysis came into existence since the early 20$^{\text{th}}$ century. In the early days, the main goal of the power flow solver was to find the solution of power flows irrespective of time and also didn't consider any instabilities phenomenon. But with the evolution of the electric grid, the requirement for not just calculating power flows but also solving instabilities has become crucial with precision, computational speed, and efficiency. In literature, several algorithms have been introduced, which are based on numerical techniques [20]. Most of them are some alterations of the Newton-Raphson method [21, 22, 23]; this is a widely used method in the power system analysis to compute power flows and state variables.

Here, the goal is to look at the computational part of the power system security assessment, which can be divided into a steady-state and dynamic security assessment. In the case of dynamic security assessment, the dynamic model of the electric grid is considered, and the analysis is performed to find the feasible region of operation by examining the transient stability limit and technological constraints such as transient voltage limits, damping limits, and such [24, 25]. Several algorithms are proposed which rely on either full simulations or using approximate methods [11]. Examples of comprehensive simulation methods include time-domain simulation for transient security and eigenvalue analysis for small signal stability [12]. Approximate methods include techniques such as the direct energy methods for transient stability evaluation.

The steady-state security assessment considers a steady-state model. The system dynamics influencing voltage stability are usually slow, so many aspects of the system can be effectively analyzed by using the static method [26]. The analysis is performed for calculating voltage stability limits (also pointed as solvability boundary in Fig.1-3), with technological constraints like voltage magnitude limits on load buses, active and reactive generation capabilities for generator buses, and line thermal limits, etc. In the steady-state security analysis, examples of full simulation methods include power flow solution of PV curves, and approximate methods include techniques such as sensitivity methods for voltage assessment [11]. In this research, we will deal with the steady-state security assessment.

As described earlier, the modern electric grids are quite complex and may contain thousands of elements. This raises several concerns with the computational part of the security analysis in terms of scalability of the proposed method to large networks, flexibility to solve with technological and economic constraints, the precision of computed results, and the most important one is computational speed. Although the approximate techniques for security analysis may have advantage in terms of computational speed but they lack with precision in results and may not be flexible to include constraints, on the other side full simulation methods may suffer from computation speed but can provide better results and room for flexibility as well to include additional limits or constraints.

1.3   Power System Stability

Power system stability analysis is one of the cores involved in power system security assessment, and it is defined as the ability of the system to regain operating equilibrium when the initial operating regime is disturbed by physical disturbance [27]. Generally, stability in the power system is divided into steady-state and dynamic stabilities.

Nowadays, power systems are being operated proximity of their stability limits due to uncertainties associated with renewable generation and the rapid increase in

system load, etc. It resulted in real-time operation in a continuously changing environment, and any imminent disturbance can cause some catastrophic effect in the grid [28]. Normally, the response to disturbances depends upon the initial operating regime and nature of the disturbance. Factors like the non-linear nature of the power flow, complex network topology, the response of electric equipment in the network, can affect the stability profile of the grid dramatically [29, 30]. Therefore, for optimal grid management, it's is crucial to assess the system response to different disturbances. Figure 1-4 provides an overall view of the power system stability, a more comprehensive discussion is provided in [27]. This thesis work studies solvability, and voltage feasibility spaces from the voltage stability context.
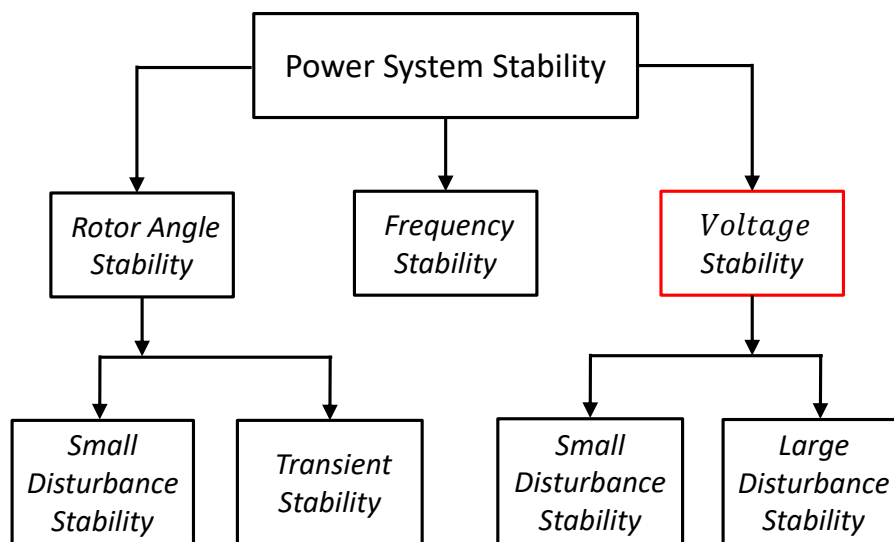
Figure 1-4: Power system stability classification.

1.3.1 Voltage Stability

Voltage stability analysis is regarded as one of the major areas of interest in the power system community as it led to many power blackouts in recent years (see Table.1.1) [31]. The voltage stability evaluation determines if a given operating condition is voltage secure. Furthermore, it is desirable to know how far the system can move

8

away from its current operating point and remain safe. Voltage stability can be classified into small disturbance and large disturbance categories.

We can classify small-disturbance voltage stability as the system's ability to maintain steady-state voltages when subjected to small perturbations such as incremental changes in system load [11, 32]. As this happens relatively slowly, it is also referred to as steady-state voltage or long-term voltage stability. Continuation Power Flow (CPF) method is standard for studying this type of instabilities [32, 33].

Whereas, large-disturbance voltage stability refers to the system's ability to maintain steady-state voltages following large disturbances such as transmission line, generation outage, or circuit contingencies [11]. The time frame of interest is in the order of several seconds. That's why; it is also referred to as short-term voltage stability. This set of voltage stability analysis requires the solution of the appropriate system, differential equations that need time-domain simulation solutions of the nonlinear response of the system after being subjected to a large disturbance. The Runge Kutta method is quite useful for studying this type of instabilities [34].

1.4   Notable Contributions

A number of works are carried out over the years to study, analyze, and compute the power flow solution space. Most of these works are limited to just characterizing a point on power flow solution space or feasible space such as [32, 33, 35] and [36]. Works from [13, 37], and [17] have also explored the feasible space in multi-dimensional parametric space.

The computational part for calculating either a point or to complete the entire solution space is a difficult task. The problem is NP-hardness (non-deterministic polynomial-time hardness) due to the non-linear power flows, technological inequality constraints, and complex topology of the network. Figure.1-5 shows the feasible space for a small 3-bus test network in power injection space. The complexity of power flow solution space is clear from Fig.1-5. A summary of the notable contributions is described in the subsequent sections.

9
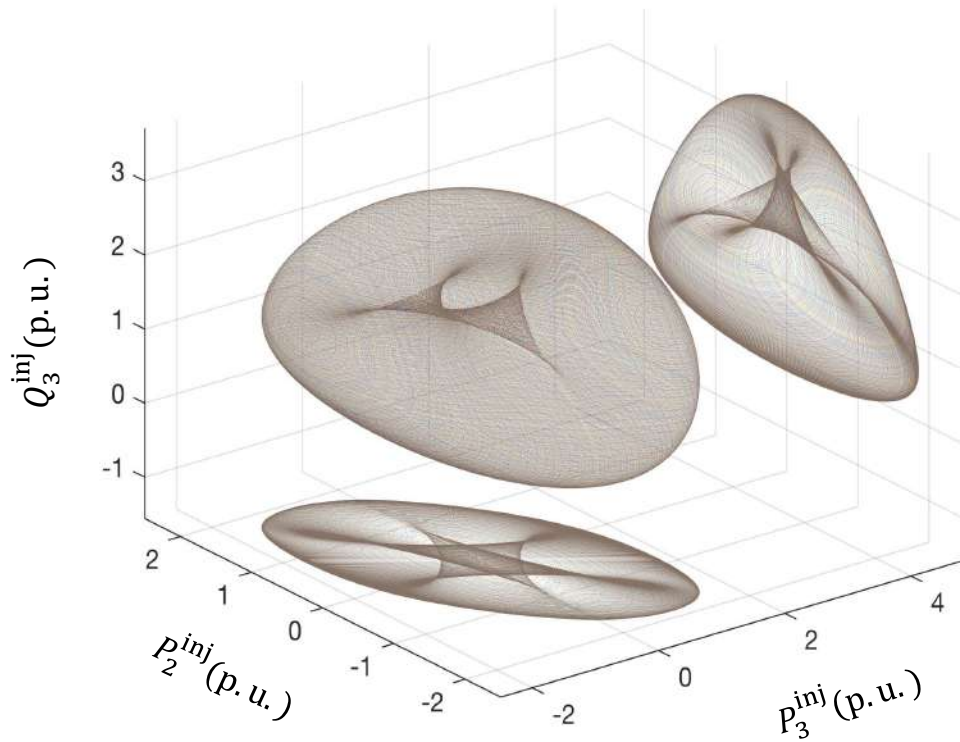
Figure 1-5: Power flow feasible space for a 3-bus network. Here P_2^{inj}, P_3^{inj} represents active power injection at bus 2 and 3. While Q_3^{inj} is the reactive power injection at bus 3. Also, projection of the feasible manifold is provided in P_2^{inj}, P_3^{inj} as contours of Q_3^{inj}. Another projection of the feasible manifold is in P_2^{inj}, Q_3^{inj} space as contours of P_3^{inj}

1.4.1 Characterizing a Point on the Feasible Space

First, we look at strategies for calculating just point on the solution manifold. Perhaps, the most popular approach to this problem is based on the continuation of power flow equations as described in [33, 38, 39]. Within this technique, the parameters of the power flow equations are adjusted gradually until the limit or solvability or constraints is reached. Although these types of algorithms are the most robust in terms of their convergence properties, they may require an unacceptably high number of computationally prohibitive matrix inversion operations. Some cheaper alternatives based on heuristic search algorithms have been proposed in the literature as well [40].

Over the last several decades multiple algorithms have been proposed to deal with the problem of the large number of iterations. Some of the earliest works on the subject were proposed in the 80s in the Soviet Union. The so-called Kontorovich method [41] enforces the Jacobian singularity condition by extending the system of power flow equations with extra equations on the zero eigenvectors of the power flow Jacobian. Conceptually similar technique based on predictor-corrector iterations was also developed in [13]. Although this approach requires a substantial increase in the number of variables of the system, the solution can be acquired in only a small number of iterations.

State of the art algorithms used for loadability analysis are discussed for example in [42, 43, 30]. In the most recent years, the academic community has proposed several innovative extensions to the traditional approaches to this problem and introduced several novel ones. Holomorphic Embedding Load Flow method (HELM) described in [44] builds upon the idea of continuation power flow equations by using polynomial and rational approximations of the homotopy between the base and saddle-node solutions. It exploits the analytic dependence of the homotopy on the loadability parameter. This property allows for construction of the full homotopy curve based only on local structure of the solution manifold around the base operating point. In [35], four different algorithms based on HELM were presented for the loadability problem, with the "Root Method" among the most computationally efficient.

In another recent study, [36] non-conventional Factored Load Flow (FLF) representation of the power flow equations have been shown to improve convergence of Newton algorithms allowing it to converge to nonphysical complex solutions when the loadability limits are exceeded. Finally, a novel algorithm based on nonlinear programming was proposed in [45]. The equivalence between optimization and continuation based approaches has been discussed in reference in [46]. Application of modern power flow relaxation (see e.g. [47]) to the problem of loadability has been discussed [48]. Finally, it is worth mentioning a complementary effort on providing sufficient conditions for solution existence reported in [49, 50] and a number of follow-up works [16, 51].

Recently, there has been significant effort focused on characterizing the maximize loadability with multiple binding constraints [52, 53]. The contribution from [53] examine the problem of maximizing the distance to a loadability limit, i.e., the loadability margin of a power system, by tuning a set of control parameters, to provide insight into the geometry of the loadability surface and classify the different types of loadability limits that can be encountered.

1.4.2 Calculating the Feasible Space

With respect to constructing the power flow feasible space, different methods have been introduced in the last decade. One of the major contributions is from [13], the work describes an implementation of predictor-corrector continuation based on hyperplanes as correctors, for tracing the solution boundaries of power flow equations in the given multi-dimensional parameter space. However, the drawbacks of the approach from [13] are as follows. i) The first proposed "Euler Homotopy" procedure is based on hyperplane predictor-corrector, which suffers from convergence issues near sharp edges and non-convexity boundaries. ii) Also, it requires a complex implementation. iii) The major disadvantage is the right eigenvector transversality condition, which increases the size of system variables by twice (additional computational burden). iv) And right eigenvector condition is also sensitive to the initial guess of the eigenvector corresponding to the null space of power flow Jacobian. Finally, the proposed

algorithm is also not computationally tractable and also not scalable for large test cases.

Whereas work proposed in [54] describes a non-iterative method referred to as a new "Δ plane" method to trace the feasibility boundaries in the state space. The method is based on the rotation of a vector in the Δ plane and subsequent computations of all singularities of the power flow Jacobian on each direction defined by this vector using the so-called X-Ray theorem [9]. The method exploits some quadratic and linear properties of the load flow equations and state matrices written in rectangular coordinates and provides a noniterative solution (except for the QR algorithm) for finding power flow singular points. The proposed Δ plane suffers from the precision of results, lacks to include technological constraints, and is also sensitive to an initial point on the boundary.

The work from [37] also highlights a new innovative approach that requires reformulating the power flow equations into sets of polynomial equations, which is then solved through Numerical Polynomial Homotopy Continuation (NPHC) method from [55] which guarantees to find all the solutions. Although the NPHC method can guarantee to find all solution boundaries, it lacks in terms of computational speed and scalability. Also, the work proposed in [37] does not consider any technological or economic constraints. In the next section, the motivations for this work and thesis structure are presented.

1.5   Original Contributions

The main research question is to calculate power flow solution space or feasible space with computational tractability, higher speed, better convergence, and scalability to large networks". Original contributions of the thesis are as follows;

1. Developing mathematical strategy to reformulate technological inequality constraints (limits on voltage levels, active and reactive generation limits, and line thermal limits). The thesis presents a slack variable methodology that allows us to represents constraints into the polynomial equation form suitable to consider

in the power flow model. This formulation preserves the sparsity structure of the power flow model.

2. Developing a novel algorithm for calculating solution (just a point) on the boundary of power flow solution space. The proposed algorithm is referred here as "Transversality Enforced Newton-Raphson" that is more robust and has better computational efficiency in comparison to alternatives. In addition, the algorithm can naturally incorporate a variety of constraints like voltage and current limits making it applicable to a broader set of problems.

3. The main idea proposed in mathematical framework of the algorithm reopens the question of auxiliary (or transversality) constraints for direct methods to find fold bifurcation points of the power flow equations. The key contribution of this method in comparison to the existing literature devoted to direct methods are as follows.

   (a) We introduce new scalar transversality conditions to supplement power flow equations to compute fold bifurcation points with small computational effort in comparison with the methods like continuation of Newton-Raphson or vector transversality conditions used previously.

   (b) We derive analytic expressions for the gradient of the proposed scalar transversality conditions allowing for a computationally efficient implementation of the algorithm.

   (c) A detailed performance analysis and comparison of the new transversality conditions, together with the clear conclusions concerning the best option.

   (d) Finally, algorithm also allows incorporation of feasibility constraints, leading to loadability problem formulated in the space of only technically acceptably solutions.

4. The later part of the thesis extends the problem to calculate the power flow feasible space in multi-dimensional parametric space. A robust continuation homotopy procedure is presented to trace the boundaries of feasible space with

ease of implementation, better numerical stability, and scalability to large networks. The proposed continuation is based on a Euler-Homotopy approach that uses a predictor-corrector path tracking procedure. Contributions within this part are as follow,

(a) Typically, the predictor-corrector approach uses tangents as predictors and hyperplanes as a corrector. Such continuation procedure suffers from difficult implementation and poor convergence for tracing curves with non-convex parts or sharp turns. In this work, we use spheres or hyperspheres as correctors referred to as "spherical continuation", which allow us to trace solution curves with sharp edges or with non-convexities.

(b) Although, the spherical continuation is rather simple, computationally efficient, with ease of implementation. Still, some modifications are required to improve the robustness and computational time. An adaptive sphere strategy is proposed based on variable radius of the spheres at each continuation step. This improves the overall computational speed of the continuation process.

(c) Another problem apprehended here was the "reversion phenomenon," i.e., tracking the backward solution. A systematic approach was presented to avoid tracing the backward solution during the continuation process.

(d) A detailed performance comparison is provided with the traditional predictor-corrector approach based on hyperplanes.

5. Finally, power flow feasible space was explored in multi-dimensional spaces. The results presented in the numerical section cover a wide range of networks that confirm the computational capability of the proposed algorithmic framework.

1.6   Thesis Structure

The key contributions of the thesis are organized as follows. Chapter 2 discuss the power flow solution spaces and operational boundaries. This chapter limits the dis-

cussion to only two bus system and describes an analytical understanding of the power flow solution space, it also provides motivations for a comprehensive computational tool for constructing solution space boundaries. In chapter 3, a detailed mathematical model is discussed. Here we also present system of equations and variables to be solved within this problem. The novel contribution "Transversality Enforced Newton-Raphson" (TENR) algorithm toward finding a point on the solution boundary is presented in chapter 4. This chapter discusses the different version of the TENR algorithm and also provides detailed numerical studies. We extend our discussion from determining just a point on the solution boundary to construct the solution boundaries in multi-dimensional parametric space in chapter 5; this chapter provides an adaptive spherical continuation techniques that can calculate boundary curves fast, with precision and scalability to a large network. Finally, we summarize the outcomes of this research work in chapter 6.

Chapter 2

Power Flow Solution Spaces

This chapter develops an understanding of the power system security regions and boundaries for robust operation. The discussion here is confined to a small two-bus system; a complete review of the solution space for this network is also presented.

2.1 Security Regions and Boundaries

The importance of calculating power flow solution space can be illustrated using the well-developed notion of security regions. Figure.2-1 shows three distinct security regions in the space of $\lambda_1 - \lambda_2$ (which are system parameters, like power injections, voltage set-points, etc.). This figure can be viewed as a slice of the solution or feasible space in $\lambda_1 - \lambda_2$ plane. In Fig.2-1, the feasibility region describes the set of points or regimes where not just real solutions to power flows exist but also all system values line flows, bus voltages, generation's capabilities are within their limits [14]. The boundary of the feasibility region is highlighted by $\boldsymbol{\beta}$ stated as a feasibility or voltage feasibility boundary. The infeasible region or solvable region in Fig.2-1 defines a domain of points where power flow equations have a real solution, but any operating points in this region violate one or more technological constraints of the systems [14]. Therefore, it is possible to operate in this region, but the controllable actions are required to bring the system back to the feasible region. The boundary of the infeasible region is denoted by $\boldsymbol{\gamma}$ referred to as solvability boundary.
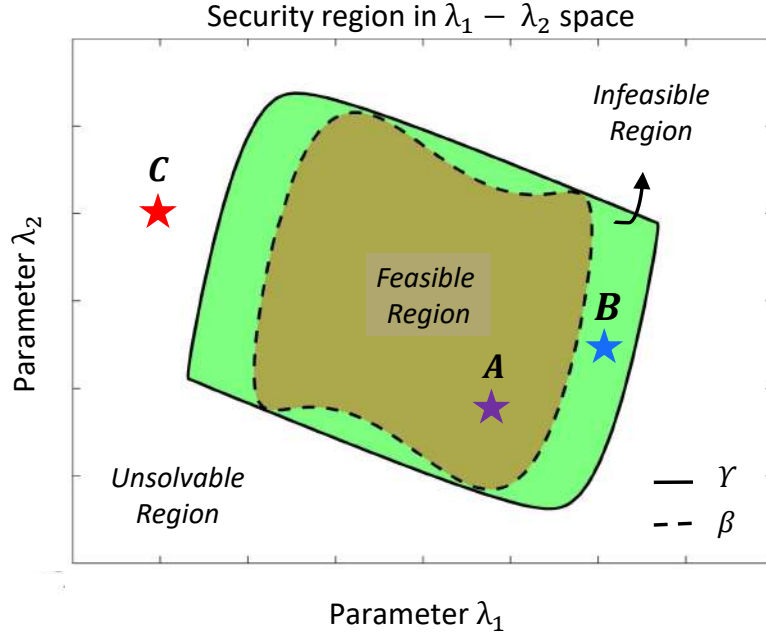
Figure 2-1: Security regions of operation.

The unsolvable region is the domain where the power flow equations have no real solution, also operating in the vicinity of the unsolvable area will result in system instability or voltage blackout. Prior knowledge about security regions (as depicted in Fig.2-1) plays a key role in determining the robustness of an operating regime for the security assessment. Figure,2-1 also shows three different operating points i.e., A, B and C in the space of $\lambda_1 - \lambda_2$. System operator can perform following tasks,

- A relative measure of security can be performed. Operating point or regime A lies within the feasible region. Thus, it is relatively more secure than B and C. While regime B is more reliable than C, as it is the infeasible region and system can still operate. While any attempt to operate with regime C will result in system instability or voltage blackout.

- If in real-time, operation of the grid moves to infeasible point B or unsolvable point C then system operator can also determine the controllable actions required to bring the operating points back to the feasible region using the information about security regions.

18

Thus, quantification of the solvability boundary γ and voltage feasibility boundary β is crucial for secure and feasible operation. The next section presents a brief discussion of the power solution space for a two-bus system.

2.2 Two Bus System

In a complete AC model power flow equations are nonlinear, and it's not practical to seek an analytical solution when the network is larger than two bus system. Even in the two-bus case, the exact solution is rarely discussed, except in the particular case where the resistance (R) is equal to zero or relatively small in comparison with reactance (X) (i.e., line is lossless). A two bus system is shown in Fig.2-2, the bus one is a slack bus with voltage as $V_s\angle 0°$, whereas bus 2 can act as either a voltage controlled bus or load bus with voltage defined as $V\angle\delta°$. Both bus 1 and bus 2 are connected by a simple inductive line with reactance equal to X.
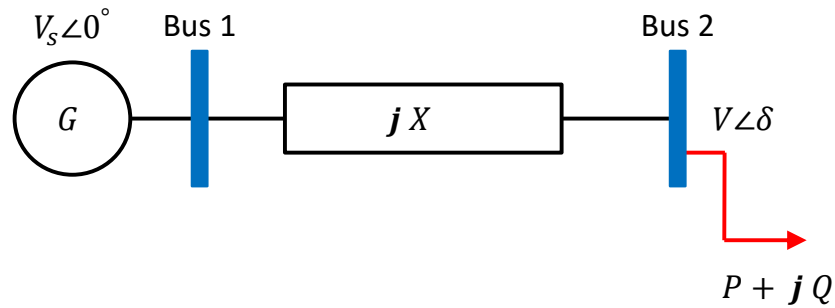
Figure 2-2: Two-bus system

2.2.1 Analytical Solutions

The Kirchhoff's Law one can represents the current following from Bus 1 to Bus 2 as follow:

$$I_{12} = \frac{V e^{\boldsymbol{j}\delta} - V_s}{\boldsymbol{j}X} \tag{2.1}$$

Thus, power injection can be represented as,

$$S = P + jQ = Ve^{j\delta} \times (I_{12})^* \tag{2.2a}$$

$$= (V\cos\delta + jV\sin\delta) \times \left(\frac{(V\cos\delta - V_s) + jV\sin\delta}{jX}\right)^* \tag{2.2b}$$

After some algebraic manipulation we can reduced to,

$$S = P + jQ = \frac{VV_s\sin\delta}{X} + j\left(\frac{V^2}{X} - \frac{VV_s\cos\delta}{X}\right) \tag{2.3}$$

Thus,

$$P = \frac{VV_s\sin\delta}{X}, \qquad Q = \left(\frac{V^2}{X} - \frac{VV_s\cos\delta}{X}\right) \tag{2.4}$$

From expressions (2.4) we can develop an equation that will form the basis for understanding the solutions spaces in different parametric space. Rewriting the (2.4) to eliminate δ,

$$cos\delta = \frac{V^2 - QX}{VV_s}, \qquad sin\delta = \frac{PX}{VV_s} \tag{2.5}$$

Applying trigonometric expression: $\sin\delta^2 + \cos\delta^2 = 1$,

$$\left(\frac{PX}{VV_s}\right)^2 + \left(\frac{V^2 - QX}{VV_s}\right)^2 = 1 \tag{2.6}$$

In (2.6) the parameters, voltage magnitude at slack bus V_s and line reactance X is usually defined. In other words, the (2.6) is a function of active power injection P, reactive power injection Q and voltage magnitude V at bus 2. Therefore, we can look at solution space boundaries in two-dimensional parametric space by keeping the third parameter as free to vary.

2.3 Solution Space in PQV

Now, we will try to establish an understanding of solution space and solution boundaries for this two bus system in PQV parameter space. First, we will try to have a look in the space of PQ and then in the space of PV. Finally, we will connect these

spaces to represents the full picture of the power flow solution space.

2.3.1 Solution Space in PQ

In this scenario, a PQ solution space and it's outer boundary is considered while keeping V as a free parameter to vary. One can rewrite the (2.6) more appropriately,

$$(PX)^2 + (V^2 - QX)^2 = (VV_s)^2 \tag{2.7a}$$

$$P^2 + \frac{V^4}{X^2} + Q^2 - \frac{2V^2Q}{X} = \left(\frac{VV_s}{X}\right)^2 \tag{2.7b}$$

$$\tag{2.7c}$$

Finally,

$$P^2 + \left(\frac{V^2}{X} - Q\right)^2 = \left(\frac{VV_s}{X}\right)^2 \tag{2.8}$$

Further, assuming $X = V = 1.0$ p.u.,

$$P^2 + (V^2 - Q)^2 = V^2 \tag{2.9}$$

The above equation is an equation of a circle in PQ, It means in PQ space solution space is a circle of radius V centered at $(0, V^2)$. To further our investigation, let us write the (2.9) in the quadratic form,

$$Q^2 - 2V^2Q + P^2 + V^4 - V^2 = 0, \tag{2.10}$$

The roots of Q for above equation can be expressed as,

$$Q_{1,2} = V^2 \pm \sqrt{V^2 - P^2} \tag{2.11}$$

Here, Q_1 describes the upper branch of the solution curve while Q_2 as the lower branch. Figure.2-3 shows the PQ circle with upper and lower branch for a particular value of $V = 0.2$ p.u..

21
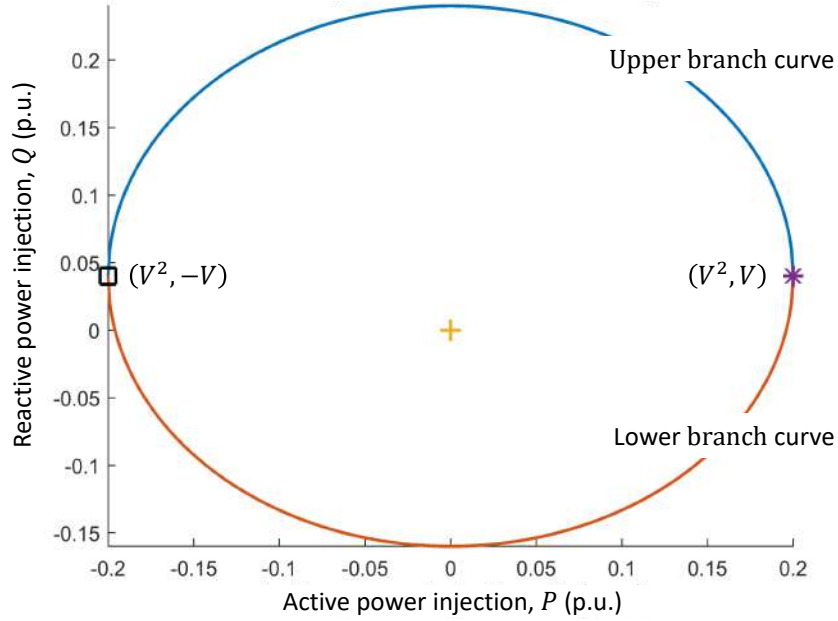
Figure 2-3: Solution space in PQ with $V = 0.2$ p.u.

Whereas the points at which upper and lower branch meets are defined as,

$$Q_1 = Q_2 = V^2, \quad P = \pm V \tag{2.12}$$

To, summarize solution space in PQ is a circle with $(-V, V^2)$ and (V, V^2) are the points where at which solution curve for Q_1 and Q_2 meet as depicted in Fig.2-3. We can quantify the solvability boundary $\boldsymbol{\gamma}$ in the this space as follow, the Fig.2-4 shows contours of PQ solution space with different values of V (dashed curves) and the solid curve in the Fig.2-4 describes the solvability boundary $\boldsymbol{\gamma}$ in PQ space. We can quantify the boundary curve $\boldsymbol{\gamma}$ by first rewriting the power flows from (2.4) with assumption that $X = V_s = 1.0$ p.u.,

$$P = V \sin \delta = V^m \quad \text{and} \quad Q = V^2 - V \cos \delta = (V^r)^2 + (V^m)^2 - V^r \tag{2.13}$$

In the above equation $V^r = V \cos \delta$ and $V^m = V \sin \delta$ are the real and imaginary part of the complex voltage phasor at the second bus. Let us consider if $f = [P, Q]^\top$ represents the vector of power flows and $x = [V^r, V^m]^\top$ is the vector of state variables

22
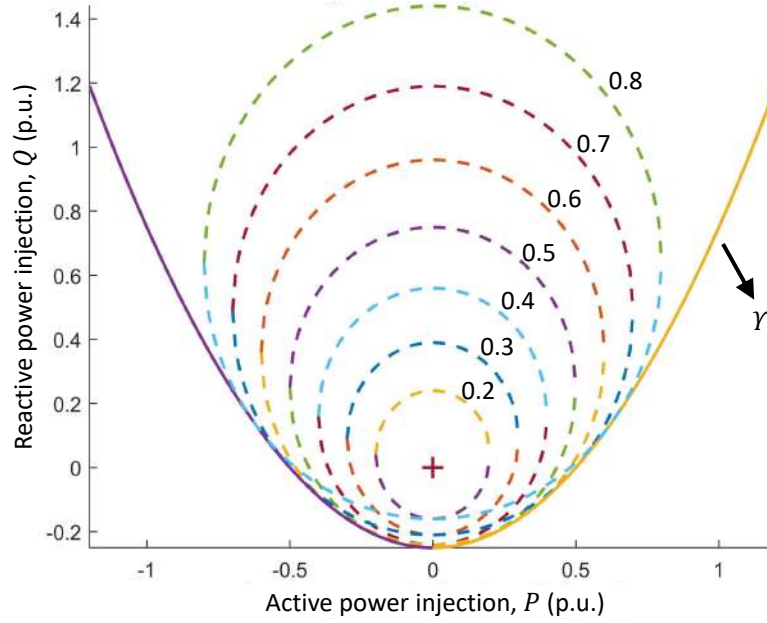
Figure 2-4: Power flow solution space in PQ contours of V.

then the gradient of f is can be described as,

$$\partial_x f = \begin{bmatrix} 0 & 1 \\ 2V^r - 1 & 2V^m \end{bmatrix} \tag{2.14}$$

At the boundary $\boldsymbol{\gamma}$ the gradient of power flow equations is degenerate thus,

$$\det[\partial_x f] = 0 \rightarrow V^r = \frac{1}{2} \tag{2.15}$$

Using the above conditions and power flows described by (2.13) we can conclude the curve $\boldsymbol{\gamma}$ in PQ space as,

$$Q = P^2 - \frac{1}{4} \tag{2.16}$$

From (2.16) it is clear that the solvability boundary $\boldsymbol{\gamma}$ is parabolic shifted by $1/4$, as shown in Fig.2-4 as well. At this boundary, the real solution to power flows exists, and the real solution disappears outside this boundary. It's an open boundary with no maximum bound on the value of Q, while the minimum bound on Q is -0.25 p.u.

23
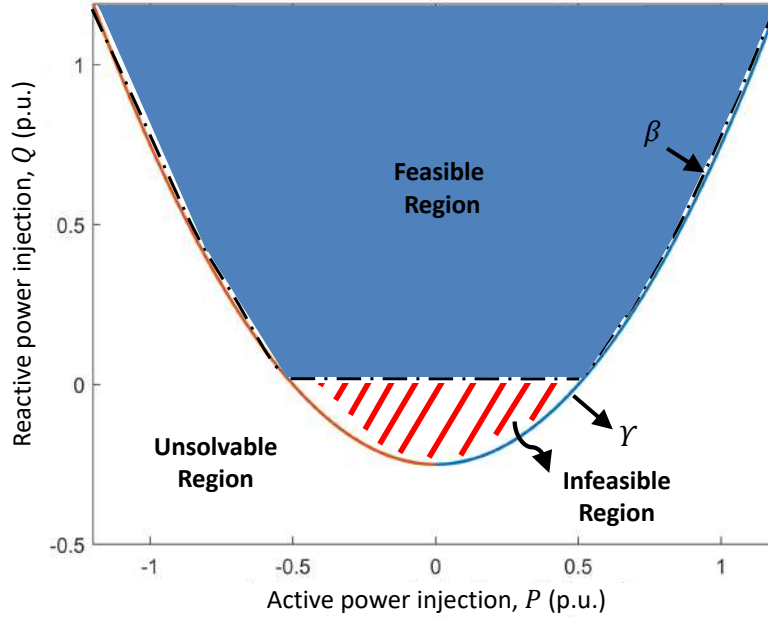
Figure 2-5: Power flow operational boundaries in PQ space.

2.3.1.1 Feasibility space in PQ

Here, we also consider the feasibility boundary $\boldsymbol{\beta}$ in PQ space. We can introduce a condition that $Q \geq Q_{\min}$. Here $Q_{\min}$ is a lower bound on value of Q. We can quantify the feasibility boundary using the (2.16) and the condition $Q \leq Q_{\min}$ as follow,

$$Q = \begin{cases} Q_{\min} & -(\sqrt{1+4Q_{\min}})/2 \leq P \leq (\sqrt{1+4Q_{\min}})/2 \\ P^2 - (1/4) & P \geq (\sqrt{1+4Q_{\min}})/2 \\ P^2 - (1/4) & P \leq -(\sqrt{1+4Q_{\min}})/2 \end{cases} \qquad (2.17)$$

Figure.2-5 shows different operational boundaries and regions with feasibility constraint $Q \geq 0 \ p.u$. All the points within the region confined by boundary $\boldsymbol{\beta}$ satisfy (2.17). Therefore, this region is the feasible region and boundary $\boldsymbol{\beta}$ is the feasibility boundary. Whereas the region enclosed by $\boldsymbol{\gamma}$ is the infeasible region as highlighted in Fig.2-5. The curve $\boldsymbol{\gamma}$ is the solvability boundary it separates the infeasible region with the unfeasible region.

2.3.2 Solution Space in PV

Here we explore the solution space in PV space, and keeps Q as a free parameter to vary. Let us rewrite the (2.6) here,

$$\left(\frac{PX}{VV_s}\right) + \left(\frac{V^2 - QX}{VV_s}\right) = 1 \tag{2.18}$$

We can reformulate above equation in the quadratic form with $X = V = 1 p.u.$,

$$V^4 - V^2(2Q + 1) + P^2 + Q^2 = 0, \tag{2.19}$$

Replacing V^2 by new variable y,

$$y^2 - y(2Q + 1) + P^2 + Q^2 = 0 \tag{2.20}$$

The roots for above equation are,

$$y_{1,2} = \frac{(2Q + 1) \pm \sqrt{4Q + 1 - 4P^2}}{2} \tag{2.21}$$

From the above equations, it is clear that V has four possible solutions. But, out of four roots, only the two have physical meaning. These two physical solutions correspond to a high voltage and a low voltage solution. If we consider, $P = 0$ then we will get $V = 1$ or 0 as can be observed from Fig.2-6, the higher voltage operating point $V = 1$ is stable, and the lower voltage operating point $V = 0$ is unstable [13, 32]. The power system can only operate on the upper- half of the PV curve, where the system dynamics act to restore the state to the operating point when it is perturbed. On the other hand, any slight disturbances from the low voltage operating point on the lower half of the PV curve result in the operating state moving away from the operating point towards the origin. Another thing is worth noticing, which is that both states (stable and unstable) will collide only at one point, which is known as a critical point (i.e., knee point of this nose curve or saddle-node bifurcation point).
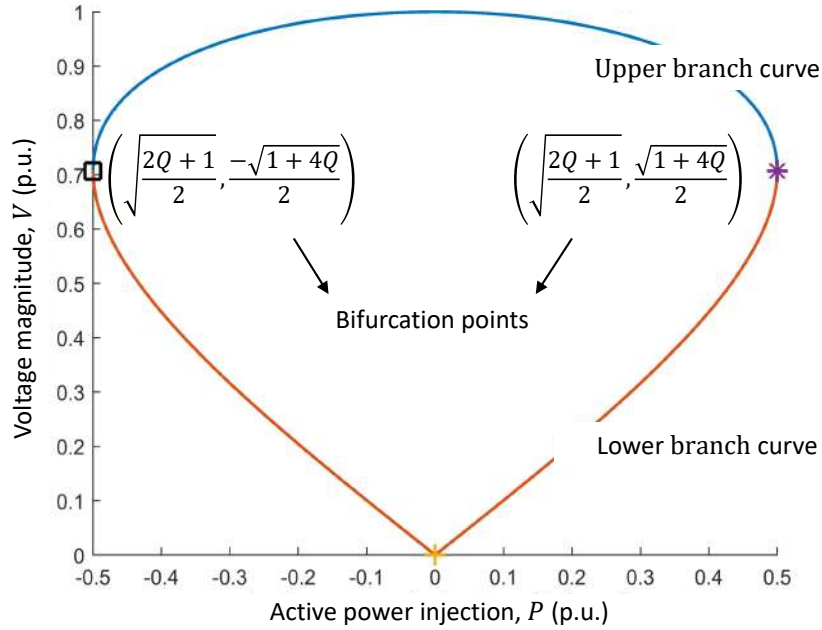
Figure 2-6: Solution space in PV with $Q = 0.0$ p.u.

At at the critical or saddle-node bifurcation point:

$$V_{1,2} = \sqrt{\frac{2Q + 1}{2}}, \quad \text{with} \quad P = \pm\frac{\sqrt{1 + 4Q}}{2}, \tag{2.22}$$

The limiting value of Q for which $P = \pm(\sqrt{1 + 4Q})/2$ is equal to -0.25 p.u. and the corresponding $V_2 = 0.5$ p.u.. From fig.2-4 we can observe the minimum bound on value of Q is -0.25 p.u.. Figure.2-7 shows contours of solution space in PV for different values of Q. In Fig.2-7 the dashed curves correspond to the solution space in PV for distinct values of Q, whereas the solid in Fig.2-7 depicts the outer boundary $\boldsymbol{\gamma}$ in the PV space. The boundary $\boldsymbol{\gamma}$ is determined by using the (2.13) and (2.15)

$$P = V^m, \quad Q = V^2 - V^r \tag{2.23a}$$

$$V^r = \frac{1}{2} \tag{2.23b}$$

From above expression,

$$P = \sqrt{V^2 - (V^r)^2} = \sqrt{V^2 - \frac{1}{4}} \tag{2.24}$$

26
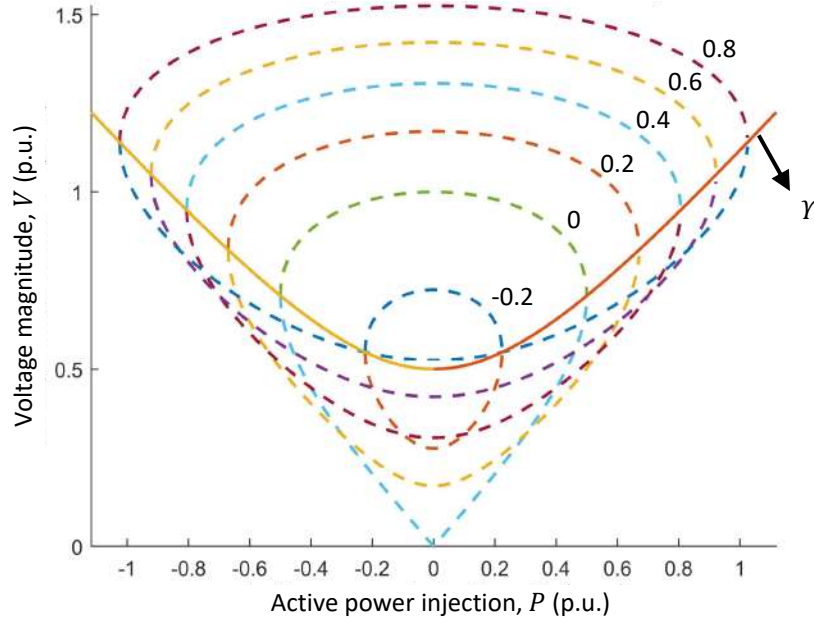
Figure 2-7: Power flow solution space in PV contours of Q.

Thus finally the expression for boundary $\boldsymbol{\gamma}$ in this case is,

$$V = \frac{\sqrt{4P^2 + 1}}{2} \tag{2.25}$$

It is also an open boundary with no maximum bound on the value of V, while the minimum bound on V is 0.5 p.u..

It is also worth noticing that contours of Fig.2-4 corresponds to the horizontal slices through Fig.2-7, while the contours of Fig.2-7 are the horizontal slices through Fig.2-4. Thus, both Fig.2-4 and Fig.2-7 provide a complete understanding of the solution space in PQV space.

2.3.2.1 Feasibility space in PV

Here we also consider a feasibility constraint and try to distinguish different operational regions and corresponding boundaries, by enforcing a feasibility constraint as follow $V \geq V_{\min}$. Here $V_{\min}$ is a lower bound on the voltage value, usually such constraint is important from power quality context. We can now quantify the feasibility
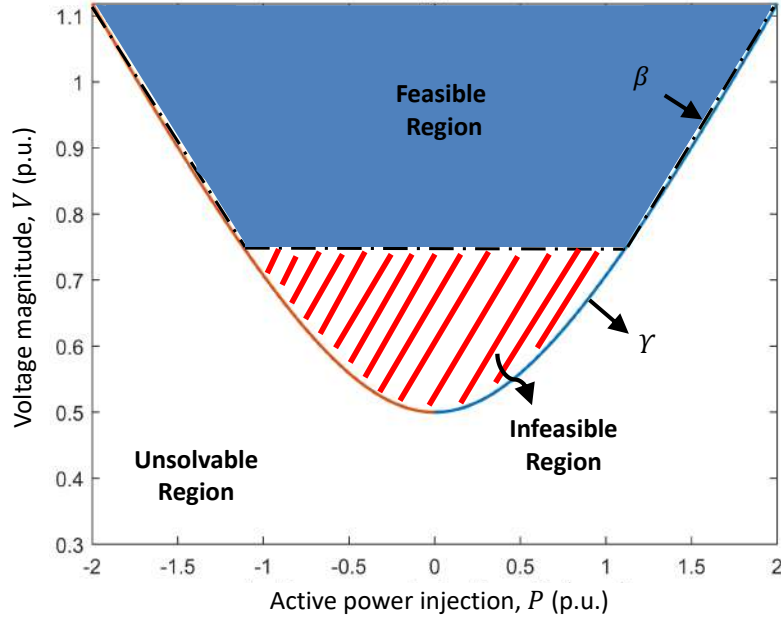
Figure 2-8: Power flow operational boundaries in PV space.

domain by using (2.25) and condition $V \geq V_{\min}$.

$$
V = \left\{
\begin{array}{ll}
V_{\min} & -\sqrt{V_{\min}^2 - (1/4)} \leq P \leq \sqrt{V_{\min}^2 - (1/4)} \\
(\sqrt{4P^2 + 1})/2 & P \geq \sqrt{V_{\min}^2 - (1/4)} \\
(\sqrt{4P^2 + 1})/2 & P \leq -\sqrt{V_{\min}^2 - (1/4)}
\end{array}
\right\} \tag{2.26}
$$

Figure.2-7 shows different operational boundaries and regions with condition $V \geq 0.7$ *p.u.* All the points in the region confined by boundary $\boldsymbol{\beta}$ satisfy (2.26). Therefore, this region is the feasible region and boundary $\boldsymbol{\beta}$ is the feasibility boundary. Whereas the region enclosed by $\boldsymbol{\gamma}$ is the infeasible region as highlighted in Fig.2-8. The curve $\boldsymbol{\gamma}$ is the solvability boundary it separates the infeasible region with the unfeasible region.

Although characterizing the solution space for this two-bus system using analytical expressions was somewhat demanding, but it demonstrates the complexity of the problem and the need for robust numerical tools to solve for large test networks.

2.4 Summary

The summary of the chapter is as follow. A general description of power flow operational regions, and solution boundaries is provided in terms of power system security assessment. This chapter also provides a complete analytical solution for a two bus network to demonstrate the complexity of the problem and even highlights the importance of numerical methodologies.

Chapter 3

Mathematical Formulation

In this chapter, we develop a general mathematical description of the power flow feasible space, the mathematical model of the power system, power flow equations, and reformulation of the technological constraints are also described here.

3.1 Problem Statement

The general steady-state equilibrium model for power system is expressed in the following standard way:

$$f_i(x, \lambda) = 0, \qquad i = 1, ...n. \tag{3.1}$$

Here, $x \in \mathbb{R}^n$ is the vector of system variables, while $\lambda \in \mathbb{R}^p$ is the parameter that defines boundedness on free parameter, and $f_i : \mathbb{R}^{n+p} \times \mathbb{R} \to \mathbb{R}^n$ is the system of nonlinear algebraic equations representing both the power flow equations and the technological constraints. More details on system of equations and variables considered in (3.1) are provided in Section.3.3. First, we will establish an abstract understanding of the power flow solution space boundaries as follow; system in (3.1) defines the n number of equations in $(n + p)$ variables, as there are p free parameters the solution space is a p-manifold. Let us consider Fig.3-1 in which each contour curve is obtained by releasing a free parameter λ_1 i.e., injected power while observing state x such as voltage set points.

31
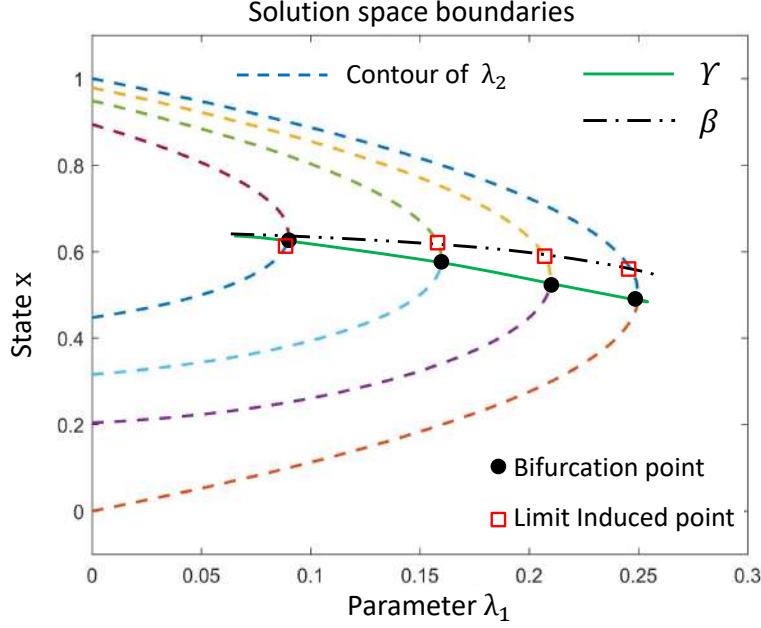
Figure 3-1: Power flow solution space and boundaries in $\lambda_1 - \lambda_2$ space.

Assuming, there is only one parameter free to vary i.e., $p = 1$, solution of (3.1) defines a $1-$manifold curve or similar to each contour curves in Fig.3-1. If we release a second parameter λ_2 as well then $p = 2$ and the solution of (3.1) is a $2-$manifold surface, as an example the dashed curves in Fig.3-1 defines the contours of such surface.

The goal here is to construct the solvability $\boldsymbol{\gamma}$ or voltage feasibility boundary $\boldsymbol{\beta}$ of (3.1) as highlighted in Fig.3-1. For which either at the $\boldsymbol{\gamma}$ or $\boldsymbol{\beta}$ boundary, the real solution of the system considered in (3.1) disappears either due to violation of some constraint or due to the solvability of the power flows. Thus, at such boundaries the gradient of $f_i(x, \lambda)$ becomes degenerate [13, 56],

$$g(x) = \det \ \partial_x f(x, \lambda) = 0 \tag{3.2}$$

Equation (3.2) is referred as transversality condition describing the degeneracy of the Jacobian $\partial_x f(x, \lambda)$. It corresponds to a disappearance of the power flow solution due to the singularity of Jacobian or violation of any technological constraints. There are several ways to enforce condition $g(x)$, we will comeback to this point later.

32

Introducing (3.2), makes number of equations $(n+1)$ in $(n+p)$ variables. Again the generalization is the following, if p free variables the solution boundary is a $(p-1)$-manifold. If we consider $p=1$ then we have $(n+1)$ equations with $(n+1)$ variables and solution of (3.1) is just a point on the solution boundary, denoted as bifurcation point in case of γ and limit induced point in case of β (as in Fig.3-1). However, the context of this work explore the structure of solution boundary with $p=2$, thus resulting in $1-$manifold curve. Points on the solution space boundary are therefore described by,

$$f_i(x, \lambda) = 0, \qquad i = 1 \ldots n \tag{3.3a}$$

$$g(x) = 0. \tag{3.3b}$$

In general, one can construct solution boundary by interpolating between limit induced or bifurcation points of contour curves of λ_2 , but due to complex structure of the solution space topology, nonlinear model of the power flows and operational constraints this is rather difficult and also computationally expensive. In this work a more systematic approach is presented.

The subsequent section describes, the general model of power system like type of buses, and power system network model.

3.2   Power System Model

Describing a general structure of the power system model is essential for power flow analysis. Although a real power system is rather complicated, for analysis, such complex systems can be realized by a network structure. A graphical representation of a three bus system is presented in Fig.3-2, which is modeled as a network of buses (nodes) connected by the transmission lines (edges). In the equivalent circuit representation, a bus is electrically equal to a single point on a circuit, and it marks the location of one of two things: a generator that injects power, or a load that consumes power [57]. Each bus in this three bus network is connected by the edges
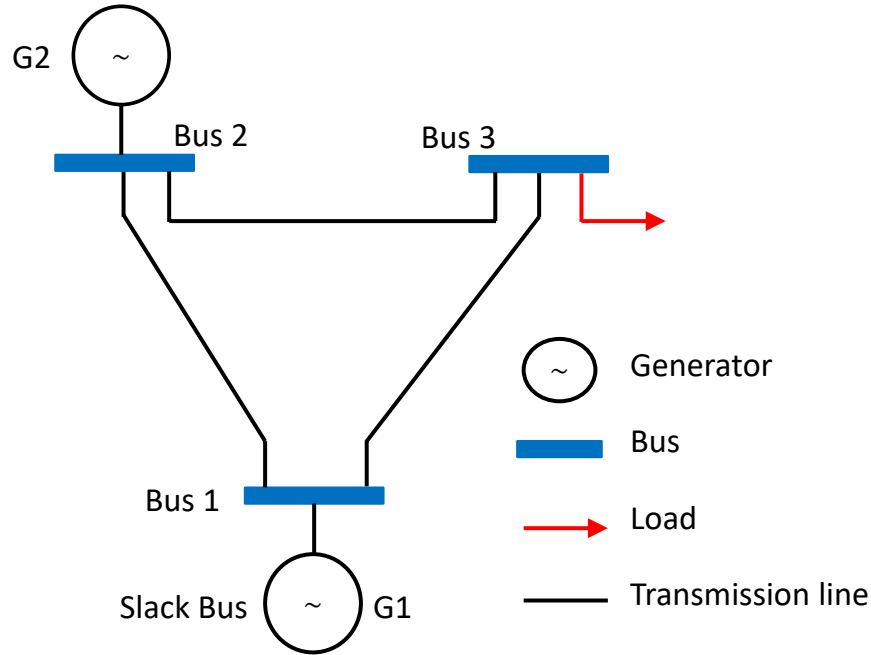
Figure 3-2: Graph representation of the three bus system.

referred to as transmission lines. These lines have some impedance, which is based on the physical characteristics of the line conductors and from the equipment like transformers, shunt capacitors, etc.

For each bus i in the network (except for the slack bus), four electrical quantities are of importance; $|V_i|$ Voltage magnitudes, δ_i voltage phase angle, P_i injected active power, Q_i injected reactive power. Based on these electrical quantities, power system buses can be classified as follows,

3.2.1 Network buses

In a conventional power network setting, there are three main types of buses, slack bus, load and generator bus.

- From a mathematical context, slack bus (or swing bus) serves the purpose of keeping active and reactive power balance in the system. Thus, at this slack bus, voltage phase angle and voltage magnitude are defined. The slack bus also sets the phase angle reference against all the other types of buses in the

network. The slack bus can be seen as a "distributed slack," representing a group of generators corresponding to slack power-sharing. This bus is usually connected by a generator, as shown in Fig.3-2.

- The second type is the load bus or PQ bus, at which given power consumption is determined by the consumer. The real and reactive powers drawn at the load buses i are defined by the $-P_i^{\text{load}}$ and $-Q_i^{\text{load}}$ respectively, the negative sign accommodates for the power flowing out of the bus. The objective of the power flow analysis is to find the voltage magnitude $|V_i|$ and angle δ_i at the load buses in the network.

- Finally, the generator bus is also identified as voltage controlled or PV bus. This type of bus is connected by a generator as in Fig.3-2. Values of active generation P_i^{gen} and voltage magnitude $|V_i|$ are specified , while the reactive generation Q_i^{gen} and phase angle δ_i at this bus are treated as unknowns. Thus, in power flow analysis the goal is to determine the phase angle δ_i at generator buses.

Table.3.1 provides the summary of physical quantities related to the each type of bus in the network.

Table 3.1: Summary of the physical parameters in the network .

Type	Given parameters	Variables x
Generator Bus or PV Bus	P_i^{gen}	δ
Load Bus or PQ Bus	P_i^{load}, Q_i^{load}	$|V|,\ \delta$

3.2.2 Admittance Matrix Y_{bus}

The network description of the interconnected power system is described by the admittance matrix $\boldsymbol{Y}_{\text{bus}}$. It relates the nodal quantities current injections at each bus in the network by the voltages at each node. The sense of the injected current is similar to the injected power at a bus, positive if it is following in and negative for flowing
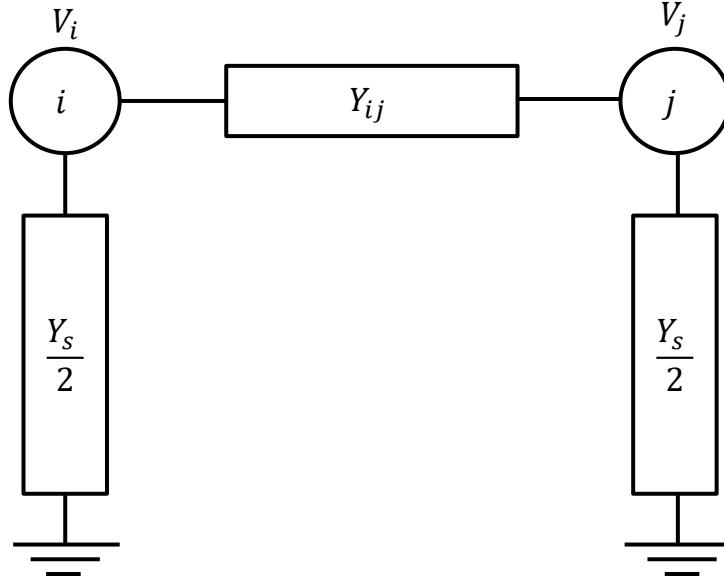
Figure 3-3: Transmission line model

out of the bus. There are two ways to relate the current injections to the bus volt-ages, one based on node-branch equations, and another is through nodal equations. Here, nodal equation representation is utilized as it results in a small number of inde-pendent equations comparing to the node-branch representation, Nodal description is described as follow,

Transmission line model:

$$I = Y_{\text{bus}}V \tag{3.4}$$

Transmission model is shown in Fig.3-3 that connects a node i with a node j. The general mathematical description of this transmission model is stated through (3.4), which describes the Ohm's law in matrix form. In (3.4) $I \in \mathbb{C}^n$ denotes the vector of complex current injections at bus i, whereas $V \in \mathbb{C}^n$ is the vector of complex voltage phasors at each bus i. In (3.4), $Y_{\text{bus}} \in \mathbb{C}^{n \times n}$ describes a complex square matrix referred as bus admittance matrix, that relates I with V. Generally, Y_{bus} preserves the sparsity structure of the network as it defines the network topology through lines-buses connectivity [58]. We can calculate entries in the admittance matrix as follow,

Let I_{ij} denote the current flowing (see Fig.3-3) from bus i toward bus j (such that $j \neq i$), or flowing toward the ground (in case of a shunt). One can apply Kirchhoff's current law here to calculate the current injection at bus i,

$$I_i = \sum_j I_{ij} \tag{3.5}$$

If Y_{ij} denotes the value of admittance of the line between bus i and j, then without the inclusion of shunt Ohm's law states that:

$$I_{ij} = y_{ij}(V_i - V_j) \quad \text{and} \quad I_{ji} = -I_{ij} \tag{3.6}$$

In matrix form, it can be described as follows:

$$\begin{bmatrix} I_{ij} \\ I_{ji} \end{bmatrix} = Y_{ij} \begin{bmatrix} 1 & -1 \\ -1 & 1 \end{bmatrix} \begin{bmatrix} V_i \\ V_j \end{bmatrix} \tag{3.7}$$

Normally y_{ij} is a complex entry with both real and imaginary parts, the real part shows quantify conductance, and imaginary part specifies susceptance. In case of no connection (or line) between i and j, value of $y_{ij} = 0$.

Shunt model

The common network model also considers shunt element, now suppose that there is a shunt y_s also connected to bus i (as in Fig.3-3). Then, one can describe the connection of shunt element to the bus i by the additional term,

$$I_{is} = Y_s(V_i - 0) = Y_s V_i \tag{3.8}$$

Based on Fig.3-3, for a transmission line between the buses i and j half of the line shunt admittance i.e., $Y_s/2$, has to be added to both Y_{ii} and Y_{jj} in the admittance
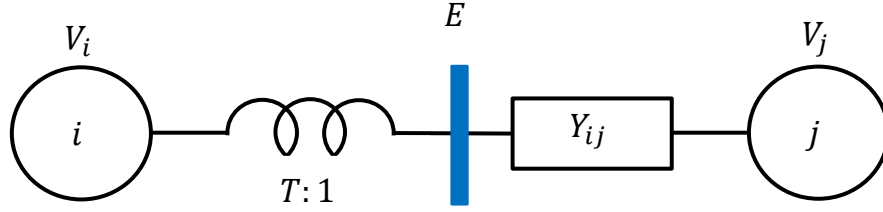
Figure 3-4: Transformer model.

matrix. Thus, we can define the following matrix form:

$$\begin{bmatrix} I_{ij} \\ I_{ji} \end{bmatrix} = \left(Y_{ij} \begin{bmatrix} 1 & -1 \\ -1 & 1 \end{bmatrix} + Y_s \begin{bmatrix} \frac{1}{2} & 0 \\ 0 & \frac{1}{2} \end{bmatrix} \right) \begin{bmatrix} V_i \\ V_j \end{bmatrix} \tag{3.9}$$

Transformer Model

The transformer model is represented in Figure (3-4), it shows a transformer between bus i and j. While the transformer ratio is described by $T : 1$. The modulus of T determines the change in voltage magnitude. One can write the relation for induced voltage E by transformer as follow,

$$V_i = TE \tag{3.10}$$

Thus, the current flowing in the direction of bus i from the bus j (i.e., I_{ji}) to the transformer device can be written as,

$$I_{ji} = y_{ij}(V_j - E) = Y_{ij}\left(V_j - \frac{V_i}{T}\right) \tag{3.11}$$

Whereas the relation between I_{ij} and I_{ji} can be derived by applying conservation of power between transformer,

$$V_i I_{ij}^* = -E I_{ji}^* \Leftrightarrow T I_{ij}^* = -I_{ji}^* \Leftrightarrow T^* I_{ij} = -I_{ji} \tag{3.12}$$

38

Therefore, the current from bus i to the transformer device and thus in the direction of j is:

$$I_{ij} = -I_{ji}/T = Y_{ij}\left(\frac{V_i}{|T|^2} - \frac{V_j}{T}\right) \tag{3.13}$$

The total contribution to the admittance matrix, of a branch between bus i and bus j, thus becomes:

$$\begin{bmatrix} I_{ij} \\ I_{ji} \end{bmatrix} = \left(Y_{ij} \begin{bmatrix} \frac{1}{|T|^2} & -\frac{1}{T} \\ -\frac{1}{T} & 1 \end{bmatrix} + Y_s \begin{bmatrix} \frac{1}{2} & 0 \\ 0 & \frac{1}{2} \end{bmatrix} \right) \begin{bmatrix} V_i \\ V_j \end{bmatrix} \tag{3.14}$$

Where $T = 1$ if the branch is not a transformer. A more general representation of the the admittance matrix $\boldsymbol{Y}_{\text{bus}}$ can now be constructed as follow.

$$\boldsymbol{Y}_{\text{bus}} = \boldsymbol{G}_{\text{bus}} + j\boldsymbol{B}_{\text{bus}} = \begin{bmatrix} Y_{11} & Y_{12} & Y_{13} & \dots & Y_{1n} \\ Y_{21} & Y_{22} & Y_{23} & \dots & Y_{2n} \\ \vdots & \vdots & \vdots & \ddots & \vdots \\ Y_{n1} & Y_{n2} & Y_{n3} & \dots & Y_{nn} \end{bmatrix} \tag{3.15}$$

In matrix $\boldsymbol{Y}_{\text{bus}}$ the diagonal entries y_{ii} denote self admittance of node i, while the off-diagonal entries y_{ij} describes the mutual admittance of node i and j node (negative sum of all admittance between i and j). While the $\boldsymbol{G}_{\text{bus}}$ and $\boldsymbol{B}_{\text{bus}}$ represents $(n \times n)$ real and imaginary part of the $\boldsymbol{Y}_{\text{bus}}$ matrix as follow,

$$\boldsymbol{G}_{\text{bus}} = \begin{bmatrix} G_{11} & G_{12} & G_{13} & \dots & G_{1n} \\ G_{21} & G_{22} & G_{23} & \dots & G_{2n} \\ \vdots & \vdots & \vdots & \ddots & \vdots \\ G_{n1} & G_{n2} & G_{n3} & \dots & G_{nn} \end{bmatrix} \tag{3.16a}$$

$$\boldsymbol{B}_{\text{bus}} = \begin{bmatrix} B_{11} & B_{12} & B_{13} & \dots & B_{1n} \\ B_{21} & B_{22} & B_{23} & \dots & B_{2n} \\ \vdots & \vdots & \vdots & \ddots & \vdots \\ B_{n1} & B_{n2} & B_{n3} & \dots & B_{nn} \end{bmatrix} \tag{3.16b}$$

In the next section, we will define the system of equations and variables considered

in $f_i(x, \lambda)$, the section will discuss modified power flows, and a methodology for the reformulation of technological inequalities into set of polynomial equations suitable to considered in (3.1).

3.3   System of Equations and Variables

First, we will consider the power flow model in Section.3.3.1 and then the reformulated technological constraints are discussed in Section.3.3.2.

3.3.1   Power Flow Model

Power flow model can be described in both polar and rectangular coordinates. Here, we consider the formulation in rectangular coordinates for the following reasons. i) Ease of implementation/programming. ii) Furthermore, this formulation also simplifies the system of equations by neglecting the higher-order terms in Taylor series [59]. And finally, it allows formulating the inequality constraints into a quadratic form [60] suitable to consider in (3.1). Let us consider the real representation of the power flow equations in terms of complex voltage phasor $\hat{V}_i \in \mathbb{C}$ at bus i in terms of its real and imaginary part as $\hat{V}_i = V_i^r + \boldsymbol{j}V_i^m$.

For a n bus system, with $\mathcal{N} = \{1, 2, \ldots, n\}$ represents the set of all buses, $\mathcal{L}$ is the set of load (PQ) buses, and $\mathcal{G}$ is the set of generator (PV) buses. For each bus $i \in \mathcal{N}$ in the network except slack bus $\mathcal{S}$ the complex voltage phasor is expressed as $\hat{V}_i = V_i^r + \boldsymbol{j}V_i^m$. The complex power injected vector $\boldsymbol{S} \in \mathbb{C}^n$ in a n bus system can be stated as follow,

$$\boldsymbol{S} = \boldsymbol{V}(\boldsymbol{Y}_{\text{bus}}\boldsymbol{V})^* \tag{3.17}$$

Here, $\boldsymbol{V} \in \mathbb{C}^n$ is the vector of complex voltage phasor $\boldsymbol{V} = [\hat{V}_i]^\top$, and $\boldsymbol{Y}_{\text{bus}} \in \mathbb{C}^{n \times n}$ is the complex admittance matrix such that $\boldsymbol{Y}_{\text{bus}} = [Y_{ij}] = [G_{ij} + \boldsymbol{j}B_{ij}]$, one can write

40

the (3.17) for each bus i in the system as,

$$S_i^{\text{inj}} = P_i^{\text{inj}} + \boldsymbol{j}Q_i^{\text{inj}} = \hat{V}_i \times I_i^* \tag{3.18a}$$

$$= \hat{V}_i \times \left(\sum_{j \in i} Y_{ij} \hat{V}_j \right)^* \tag{3.18b}$$

In above expression, $j \in i$ denotes connection of j node to node i, even when $j = i$. While Y_{ij} represents the $(ij)^{\text{th}}$ entry of the admittance matrix Y_{bus}. We can separate the real and imaginary part of the (3.18) as follow,

$$P_i^{\text{inj}} = P_i^{\text{gen}} - P_i^{\text{load}} = \text{Re}\left(\hat{V}_i \times \left(\sum_{j \in i} Y_{ij} \hat{V}_j \right)^* \right) \tag{3.19a}$$

$$Q_i^{\text{inj}} = Q_i^{\text{gen}} - Q_i^{\text{load}} = \text{Im}\left(\hat{V}_i \times \left(\sum_{j \in i} Y_{ij} \hat{V}_j \right)^* \right) \tag{3.19b}$$

Here subscripts load, gen describe bus load and generation levels respectively. After some algebraic manipulation and introducing parameter λ we can write the (3.19) in the following from,

$$\sum_{j \in i} \left\{ V_i^r (G_{ij} V_j^r - B_{ij} V_j^m) + V_i^m (G_{ij} V_j^m + B_{ij} V_j^r) \right\}$$
$$-\lambda P_i^{\text{inj}} = 0 \tag{3.20}$$

$$\sum_{j \in i} \left\{ V_i^m (G_{ij} V_j^r - B_{ij} V_j^m) - V_i^r (G_{ij} V_j^m + B_{ij} V_j^r) \right\}$$
$$-\lambda Q_i^{\text{inj}} = 0 \tag{3.21}$$

Here λ denotes boundedness on the real and reactive power injected at bus i. We consider the problem with $\lambda_k \in \mathbb{R}^p$, value of p defines degree of freedom for free parameters. In comparison to the polar formulation, the rectangular formulation of the power flow model requires additional equations related to constant voltage magnitude at PV buses. Therefore, the rectangular formulation results in extra equations and variables relative to the polar with the difference equal to the number of the PV buses present in the system.

Thus, for each generator $i \in \mathcal{G}$ the fixed voltage levels are characterised by an additional equation,

$$(V_i^r)^2 + (V_i^m)^2 - |\hat{V}_i|_{\text{ref}}^2 = 0 \tag{3.22}$$

Here, $|\hat{V}_i|_{\text{ref}}$ denotes the specified constant voltage magnitudes at PV buses.

3.3.2 Technological Constraints

The goal is to extend the problem formulation for the boundary of the feasibility space, by extending the power flow model considered in (3.20), (3.21) and (3.22) with a set of additional equations. The steady-state security assessment also requires evaluating the robustness of an operating point, subject to constraints on voltage magnitudes, reactive power generations, and current levels. If the system in (3.1) consist of only of (3.20), (3.21) and (3.22), then the problem formulation described by (3.3) is limited to the boundary of the solvability space. As stated above, a real system operation also considers one or more technological constraints, which can be included in (3.1) such that system in (3.3) describes the formulation to the voltage feasibility boundary. In practice, these constraints are expressed in the inequality form. The following discussion shows how inequality constraints can be reformulated in the polynomial equation form suitable to consider in (3.1).

3.3.2.1 Voltage magnitude limits

Voltage magnitude limits are one of the important technological constraints in the power system operation, it's given by a very strict standards. Too high or too low voltages could cause problems with respect to end user power apparatus damage or can cause instability in the power system [61]. For each load bus $i \in \mathcal{L}$ in the network, voltage magnitudes are remained within specified bounds as,

$$|\hat{V}_i|_{\text{min}} \leq |V_i|_{\text{cal}} \leq |\hat{V}_i|_{\text{max}} \tag{3.23}$$

In (3.23), $|V_i|_{\text{cal}}$ defines the calculated voltage magnitude level, while $|\hat{V}_i|_{\text{max}}$ and $|\hat{V}_i|_{\text{min}}$ presents the maximum and minimum bound on the operational voltage magnitudes levels at PQ buses. In order to represents (3.23) in the quadratic form consistent with our (3.1), we formulate (3.23) by set of equality equations by introducing new variables as,

$$(V_i^r)^2 + (V_i^m)^2 - |\hat{V}_i|_{\text{max}}^2 + (\overline{s}_i)^2 = 0 \tag{3.24a}$$

$$(V_i^r)^2 + (V_i^m)^2 - |\hat{V}_i|_{\text{min}}^2 - (\underline{s}_i)^2 = 0 \tag{3.24b}$$

Such formulations were first suggested by the author in [56]. If the voltage levels on the load bus i lie within acceptable limits, the system (3.24) has real solutions for the slack variables $\overline{s}_i, \underline{s}_i \in \mathbb{R}$. And vice-versa, such a solution does not exist in situations where the voltage levels exceed the acceptable limits [56]. This methodology allows us to turn the solvability problem of finding solutions satisfying some feasibility inequalities into a solvable problem of the traditional power flow equations extended with additional equations and variables.

Introducing (3.24), we are constructing a boundary of the feasible region in which boundness on power flows described by (3.20) and (3.21) make sure voltage levels on load buses are also valid, such a boundary can assist transmission system operator to bring unsolvable or infeasible operating points back to the feasible space.

3.3.2.2 Active generation constraints

Active generation plays a crucial role in balancing the demand in the network. Type of different generators may behave differently, but in general, e generator bus $i \in \mathcal{G}$ in the network limits its operation with the following constraint,

$$(P_i^{\text{gen}})_{\text{min}} \le P_i^{\text{gen}} \le (P_i^{\text{gen}})_{\text{max}} \tag{3.25}$$

In (3.25) P_i^{gen} is the calculated amount of active generation, and $(P_i^{\text{gen}})_{\text{max}}$ and $(P_i^{\text{gen}})_{\text{min}}$ denote the maximum and minimum bound on the active generation at each

PV bus. Normally the lower limit is zero, but the renewable generators can also act as a load. We can also express the inequality (3.25) by the set of quadratic equations consistent with (3.1).

$$P_{\text{gen},i} - (P_{\text{gen},i})_{\max} + (\bar{r}_i)^2 = 0 \tag{3.26a}$$

$$P_{\text{gen},i} - (P_{\text{gen},i})_{\min} - (\underline{r}_i)^2 = 0 \tag{3.26b}$$

Expression (3.26) states that real solution of slack variables $\bar{r}_i$ and $\underline{r}_i \in \mathbb{R}$ exists only if (3.25) holds. Next we introduce limit on reactive generation at each generator bus.

3.3.2.3 Reactive generation constraints

It's one of the important constraint, as the system becomes more vulnerable to instabilities when the reactive power limits are encountered [62]. Each generator have some limits on the reactive power they can produce,

$$(Q_i^{\text{gen}})_{\min} \leq Q_i^{\text{gen}} \leq (Q_i^{\text{gen}})_{\max} \tag{3.27}$$

Q_i^{gen} is the calculated amount of reactive generation, and $(Q_i^{\text{gen}})_{\min}$ and $(Q_i^{\text{gen}})_{\max}$ are the maximum and minimum bound respectively. Using the same slack variable approach, the above inequality (3.27) can be expressed in form of equality equations with new slack variables $\bar{c}_i$ and $\underline{c}_i$,

$$Q_{\text{gen},i} - (Q_{\text{gen},i})_{\max} + (\bar{c}_i)^2 = 0 \tag{3.28a}$$

$$Q_{\text{gen},i} - (Q_{\text{gen},i})_{\min} - (\underline{c}_i)^2 = 0 \tag{3.28b}$$

In (3.26) $Q_i^{\text{inj}} = \text{Im}(S_i^{\text{inj}})$ from (3.18). Unlike the previous constraints the generator bus can switch it's type from PV to PQ bus once (3.27) is violated, to facilitate this switching behavior an additional slack variable t_i is introduced for the equation (3.22) that describes the constant voltage magnitude of PV buses,

$$(V_i^r)^2 + (V_i^m)^2 - |\hat{V}_{\text{ref}}|^2 - t_i = 0 \tag{3.29}$$

such that:

$$t_i.\bar{c}_i.\underline{c}_i = 0 \tag{3.30}$$

We can summarize the reactive generation constraints formulated by (3.28), (3.29) and (3.30) as follow,

- If only $t_i = 0$ in (3.30) such that both $\underline{c}_i$ and $\bar{c}_i \neq 0$, then it means reactive generation constraints (3.28) holds and the generator bus i remains PV.

- Generator bus i status will remain PV even when $t_i = 0$ and also either $\bar{c}_i$ or $\underline{c}_i$ will be equal to zero in (3.30). This means corresponding generator i has reached either at the $(Q_i^{\text{gen}})_{\text{max}}$ or $(Q_i^{\text{gen}})_{\text{min}}$ but didn't violate these limits.

- Generator i switch from PV to PQ: In (3.30) $t_i \neq 0$ and $\bar{c}_i = 0$ which means generator violates the limit on minimum reactive generation bound. Other possibility if $t_i \neq 0$ but $\underline{c}_i = 0$ which represents violation of maximum bound on reactive generation. Also, for more realistic consideration and flexibility of switching the right hand side of (3.30) is replaced by ϵ rather than equal to zero, value of ϵ was suggested is 10^{-4} from [56].

For more realistic consideration and flexibility of switching the right hand side of (3.30) is replaced by ϵ rather than equal to zero, value of ϵ was suggested is 10^{-4},

$$t_i.\bar{c}_i.\underline{c}_i = \epsilon \tag{3.31}$$

3.3.2.4   Line thermal limits

Finally, another import constraint considered here is the thermal limits on the line. Thermal limits restrict the operation of the network in a safe region such that transmission lines will not be overloaded and thus avoids tripping of the lines in the network. This constraint is specified as by keeping the complex power flowing from node i to j not to exceed some maximum bound,

$$S_{ij} \leq (S_{ij})_{\text{max}} \tag{3.32}$$

For each line $(i, j) \in \mathcal{T}$, the complex power transmitted is denoted by $S_{ij} = P_{ij} + \boldsymbol{j}Q_{ij}$. While $(S_{ij})_{\max}$ is the maximum bound on the transmitted power. One can formulate this inequality individually for both active and reactive powers flowing through the line as,

$$P_{ij} - (P_{ij})_{\max} + (m_i)^2 = 0 \tag{3.33a}$$

$$Q_{ij} - (Q_{ij})_{\max} + (n_i)^2 = 0 \tag{3.33b}$$

In above expression, m_i and n_i describe the slack variables corresponding to limit on P_{ij} and Q_{ij} respectively.

Most of the calculations include only the constraints discussed above, but the generalization presented here can be used to include any other technological constraints. It is also worth noticing that the methodology presented here to include constraints preserve the sparsity characteristic of the power flow problems. We may summarize the system of equations and variables considered in (3.1).Details about the system of equations and variables considered in (3.1) are provided in Table.3.2.

Table 3.2: Summary of equations and variables in $f_i(x, \lambda) = 0$.

Type	Equations $f_i(x, \lambda)$	Variables x
Generator Bus	(3.20), (3.26), (3.28), (3.29), (3.30)	V_i^r, V_i^m, $\bar{r}_i$, $\underline{r}_i$, $\bar{c}_i$, $\underline{c}_i$, t_i
Load Bus	(3.20), (3.21),(3.24)	V_i^r, V_i^m, $\bar{s}_i$, $\underline{s}_i$
Transmission line	(3.33)	m_i, n_i

3.4 Summary

This chapter first provides a general formulation for characterizing the solution of power flow model on the boundary of solvability and also on the boundary of the feasibility region. The network topology of a conventional electric grid is also discussed. In the last, a methodology is presented that allows converting technological inequality constraints into a set of non-algebraic equations; this formulation allows us to incorporate operational limits in a natural way such that it preserves the general structure of the power flow model.

Chapter 4

Characterizing a Point on the Feasible Space

In this chapter, we will describe a novel algorithm for calculating the points on the solvability and voltage feasibility boundary. A proof of convergence is depicted on a two-bus network. The chapter also covers the details of different choices of transversality conditions.

4.1 Problem Formulation: Boundary Points

From previous chapter, the steady-state equilibrium model of power system is expressed as follow,

$$f_i(x, \lambda) = 0, \qquad i = 1 \ldots n \tag{4.1}$$

$$f_i : \mathbb{R}^n \times \mathbb{R} \to \mathbb{R}^n, \qquad x \in \mathbb{R}^n, \text{ and } \quad \lambda \in \mathbb{R}^p$$

To characterize the solution on the feasible space (just a point) such that $\lambda = \lambda^*$, we will use $p = 1$ such that only one parameter is free to vary. Here λ^* denotes the value of free parameter λ related to the to point on the boundary. System in (4.1) is underdetermined as there are $n + 1$ variables with only n equation thus solution of (4.1) describes a 1-manifold curve. One way to solve (4.1) for λ^* is to parametrize the solution manifold with λ and use continuation based techniques from
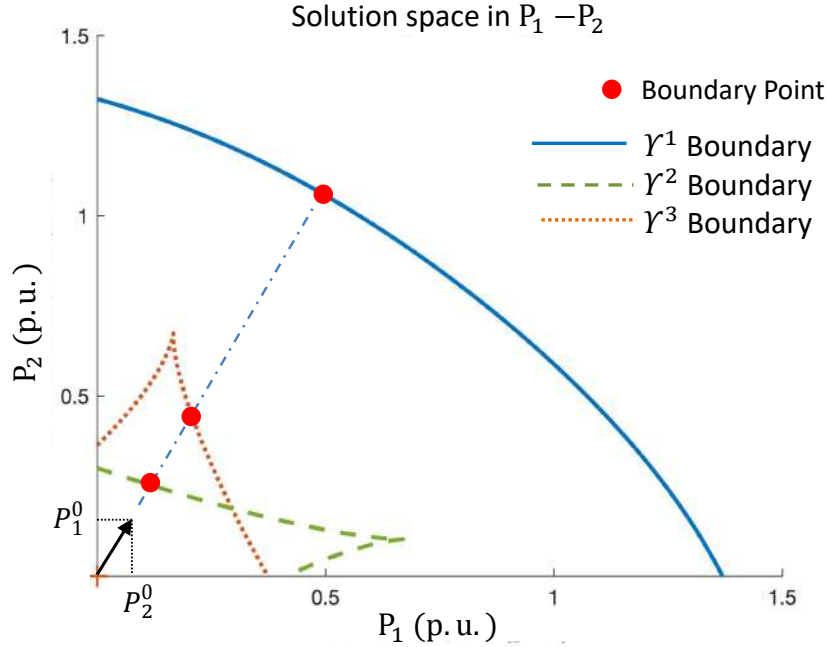
Figure 4-1: Power flow solution space and boundaries in $P_1 - P_2$ space.

[33]. Continuation approaches are well explored and robust, but are less attractive in terms of computational tractability and speed of convergence. Another way is to directly compute solution of (4.1) corresponding to $\lambda = \lambda^*$ without explicit tracking of the solution manifold. At $\lambda = \lambda^*$ the real solution of system of equations considered in (4.1) will disappear, earlier this condition was introduced as transversality condition $g(x)$. Thus, we introduce one more condition such that at the solution boundary the real solution to the system (4.1) exists only for all $\lambda \leq \lambda^*$, and the solution to (4.1) disappears for $\lambda > \lambda^*$. Extended system representing the solution of (4.1) on the solution space boundary is,

$$f_i(x, \lambda) = 0, \qquad i = 1 \ldots n \tag{4.2a}$$

$$g(x) = 0. \tag{4.2b}$$

An important point to consider here is the following. Given the non-linear nature of the power flow model, there might exist more than one solution for the system in (4.2) with respect to $\lambda \leq \lambda^*$ for a given space. Each of these solutions corresponds to the different solution branches of the solution space. As an example, consider a

solution boundary in the space of some active power injections $P_1 - P_2$ for a network. An illustration of different solution branches in $P_1 - P_2$ space is provided in Fig.4-1. Given a starting point $(P_2^0,\ P_1^0)$, the solution can end up either on the $\boldsymbol{\gamma}^1, \boldsymbol{\gamma}^2$ or $\boldsymbol{\gamma}^3$ boundary, these boundaries represents the different branches of the solution space in the $P_1 - P_2$. Thus, tracing the boundary curve depends upon the initial/starting point. This chapter focuses only on how to compute an initial point on the boundary curve, while in chapter 6, we will discuss the boundary curves and solution space in general.

4.2   Transversality Condition $g(x)$

Coming back to condition $g(x)$ i.e., (3.2) from last chapter, as stated earlier at the boundary of solvability or feasibility region, λ approaches λ^* and the real solution to system in (4.1) disappears. Thus, at the boundary the gradient of $f_i(x, \lambda)$ also referred to as Jacobian matrix

$$J_{ij} = [\partial_x f(x, \lambda)]_{ij} = \frac{\partial f_i}{\partial x_j} \tag{4.3}$$

becomes degenerated. Thus, finding the solution of system (4.1) is rather difficult as value of λ approaches λ^*. In this case the size of the Newton-Raphson step defined by $J^{-1}(x)f(x)$ becomes very large in magnitude and compromises the stability of the algorithm. Classic implementations of the Newton algorithm fail to converge or require too many steps to obtain the solution [56]. In this work we will extend the original system of equations (4.1) with an extra equation enforcing the degeneracy of the Jacobin J at the $\boldsymbol{\gamma}$ or $\boldsymbol{\beta}$ boundary and will treat the free parameter λ as an unknown variable. In this case the solutions of the extended system belong to the boundary in the space of solutions of the original system [56]. This is exactly the boundary of the feasibility set of power flow equations including technological constraints discussed in last chapter.

Following mathematical terminology, we refer to the Jacobian singularity condi-

tion as the "transversality" condition. Mathematically the transversality condition can be expressed in many different ways. For example, in [13] it was enforced by adding a system of $n + 1$ equations $Jy = 0$ and $y^\top y = 1$ for a new vector variable $y \in \mathbb{R}^n$, representing the existence of zero eigenvalue of the Jacobian. In this work, we consider several possible choices of transversality condition $g(x)$, that do not require any additional variables, and at the same time are numerically robust.

4.3 Transversality Enforced Newton-Raphson

Here we can represent the extended system in more compact notation. Thus, the problem of computing solvability boundary $\boldsymbol{\gamma}$ or voltage feasibility boundary $\boldsymbol{\beta}$ of solution space can be defined as,

$$f_i(x, \lambda) = 0, \quad i = 1, 2, \ldots, n \tag{4.4a}$$

$$g(x) = 0 \tag{4.4b}$$

$$f_i(x, \lambda) \in \mathbb{R}^{n+1}, \quad \text{and} \quad x \in \mathbb{R}^n, \lambda \in \mathbb{R}^1$$

we have $(n + 1)$ equations with $(n + 1)$ variables and solution of (4.1) is just a point on the solution boundary, representing either a limit induced or bifurcation point. From now, Numerically the system in (4.4) can be solved using traditional Newton-Raphson iterations in the space of x and λ. We can describe the steps of Newton iterations as follow,

$$f + \partial_x f \ \Delta x + \partial_\lambda f \ \Delta \lambda = 0 \tag{4.5a}$$

$$g + (\partial_x g)^\top \ \Delta x = 0 \tag{4.5b}$$

From (4.5), we can assemble the extended Jacobian $\mathcal{J}$ for this enforced Newton-Raphson in the following manner:

$$\mathcal{J} = \begin{bmatrix} \partial_x f & \partial_\lambda f \\ \partial_x g & \partial_\lambda g \end{bmatrix} = \begin{bmatrix} \partial f_i/\partial x_j & \partial f_i/\partial \lambda \\ \partial g/\partial x_j & 0 \end{bmatrix} \tag{4.6}$$

The next correction x', λ' in Newton iteration is then computed as follow,

$$x' = x + \alpha \Delta x \tag{4.7a}$$

$$\lambda' = \lambda + \alpha \Delta \lambda \tag{4.7b}$$

Steps size α plays a key role in the convergence of Newton algorithms. Normally α is chosen small enough for global convergence, but an optimal selection of α is described in [59, 63]. In our experiments, we observed some test cases required adjustment of step size α for convergence. Also, as the Newton-type algorithms are locally convergent, it means with different step size α, it is also possible to trace multiple roots of the given system of equations. After updating corrections x', λ' through (4.7) the tolerance limit is checked,

$$\left\| \, [f_i(x, \lambda), \; g(x)]^\top \, \right\| \leq \epsilon \tag{4.8}$$

At each iteration, tolerance is checked through (4.8). While the ϵ value in above equation denotes the desired precision level. Here, the results were achieved with a 6 to 8 digit precision.

To summarize, we describe a Newton algorithm to find a solution of the system in (4.1) when the solution disappears, and the J matrix becomes degenerate. Normal Newton-Raphson will fail to converge due to the singularity of the J. But, we reformulate the system in (4.1) with (4.4) such that solution can be computed with the condition J is degenerate/singular. Therefore, the proposed Newton here is stated as "Transversality Enforced Newton-Raphson" (TENR) algorithm. In the next section, definite proof of convergence is provided.

4.4 Extended Jacobian $\mathcal{J}$

From (4.5), we can assemble the extended Jacobian $\mathcal{J}$ for this TENR algorithm as follow,

$$\mathcal{J} = \begin{bmatrix} \partial_x f & \partial_\lambda f \\ \partial_x g & \partial_\lambda g \end{bmatrix} = \begin{bmatrix} \partial f_i / \partial x_j & \partial f_i / \partial \lambda \\ \partial g / \partial x_j & 0 \end{bmatrix} \tag{4.9}$$
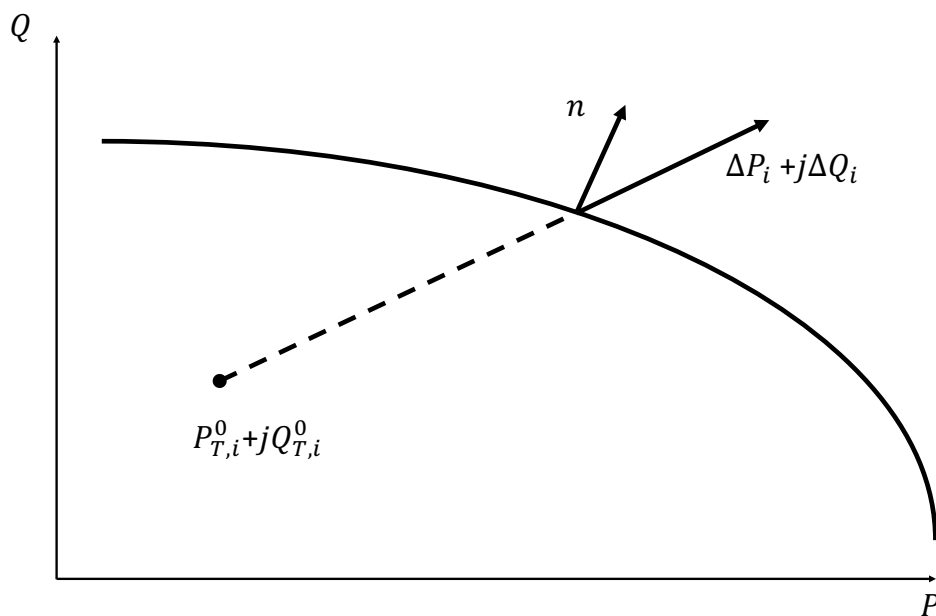
Figure 4-2: Graphical illustration of the solution boundary and power direction vector. In a typical situation, the power direction vector is not tangential to the boundary (equivalently non-orthogonal to surface normal vector n), so the extended Jacobian $\mathcal{J}$ is not singular.

The main advantage of the TENR algorithm is that even the Jacobian J of the original system is degenerate at the solution boundary, the extended Jacobian $\mathcal{J}$ remains regular. To prove this, we rewire the (4.5) in the space of Δx and $\Delta \lambda$ as,

$$f + J\Delta x + (\partial_\lambda f)\Delta \lambda = 0 \tag{4.10a}$$

$$g + (\partial_x g)^\top \Delta x = 0 \tag{4.10b}$$

Let us assume that the $\mathcal{J}$ is singular and there is $\Delta x, \Delta \lambda$ such that $\mathcal{J}[\Delta x^T, \Delta \lambda^T]^T =$

0, or from (4.10) it is equivalent to,

$$J\Delta x + (\partial_\lambda f)\Delta\lambda = 0 \tag{4.11a}$$

$$(\partial_x g)^\top \Delta x = 0 \tag{4.11b}$$

The (4.11b) means the motion along the solution boundary of the original system in the x space (i.e., voltage space) it is clear from the (4.10b). Whereas $J\Delta x$ is the direction in the PQ-space that is tangential to the boundary of solvability. Consequently, from (4.11a) it follows that $(\partial_\lambda f)\Delta\lambda$ would correspond to a degenerate choice of the power transfer direction vector which is tangential to the solution boundary, this is also evident from (4.10a). In other words, as long as the power direction vector in power space is not tangential to voltage feasibility or solvability boundary, the extended system of equations is well behaved near the boundary. The general non-degenerate case is illustrated in Fig. 4-2. Consider the following power direction vector, same notation as in [64],

$$P_{\mathrm{T},i} = P_{\mathrm{T},i}^0 + \lambda\Delta P_i, \tag{4.12a}$$

$$Q_{\mathrm{T},i} = Q_{\mathrm{T},i}^0 + \lambda\Delta Q_i \tag{4.12b}$$

Here $P_{\mathrm{T},i}^0 + \boldsymbol{j}Q_{\mathrm{T},i}^0$ denotes the initial point (i.e. $\lambda = 0$), while $\Delta P_i, \Delta Q_i$ is the power direction vector. For example, in the equations (3.20,3.21) we consider the special case $P_{T,i}^0 = \Delta P_i = P_i^{\mathrm{gen}} - P_i^{\mathrm{load}}$, $Q_{T,i}^0 = \Delta Q_i = Q_i^{\mathrm{gen}} - Q_i^{\mathrm{load}}$. As illustrated in Fig.4-2, the power direction vector $\Delta P_i + \boldsymbol{j}\Delta Q_i$ is generally not tangential to the boundary. Henceforth the Jacobian $\mathcal{J}$ remains regular. The next section illustrates this general point by going in steps through the general proof presented above in a simple case of 2-bus system.
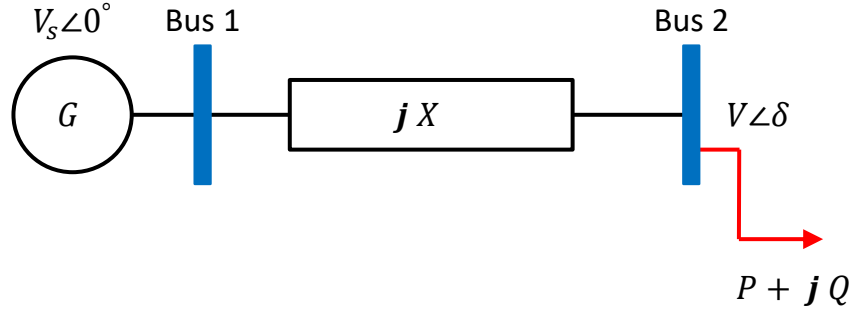
Figure 4-3: Two-bus system

4.5 Non-degeneracy of $\mathcal{J}$: an illustration

Here we can demonstrate our conjecture that extended Jacobian $\mathcal{J}$ in TENR remains non-degenerate unless the power direction vector is tangential to the solution boundary in power injection space (i.e., PQ space). Figure.4-3 shows a two-bus system with reactance $X = 1\ p.u.$ (per unit), bus 1 is a slack bus with $V_s\angle 0° = 1\angle 0°$. Bus 2 is the load bus with $V\angle\delta = V^r + \boldsymbol{j}V^m$, while P and Q denote the real and reactive power injection at bus 2. Writing the power flow equations in the following form,

$$P = V \sin\delta = V^m \tag{4.13a}$$

$$Q = V^2 - V\cos\delta = (V^r)^2 + (V^m)^2 - V^r. \tag{4.13b}$$

Based on (4.13), one can write the power flow Jacobian J as follow,

$$J \equiv \frac{\partial f}{\partial x} = \begin{pmatrix} \frac{\partial P}{\partial V^r} & \frac{\partial P}{\partial V^m} \\ \frac{\partial Q}{\partial V^r} & \frac{\partial Q}{\partial V^m} \end{pmatrix} = \begin{pmatrix} 0 & 1 \\ 2V^r - 1 & 2V^m \end{pmatrix}. \tag{4.14}$$

From transversality condition $g(x) = \det\ J = 0$, we can conclude $V^r = 1/2$. And thus solvability boundary in $V^r\ V^m$ given by $g(x) = 0$ is just a straight line $V^r = 1/2$ as depicted in Fig.4-4. Now we can have a look at the solvability boundary described

56
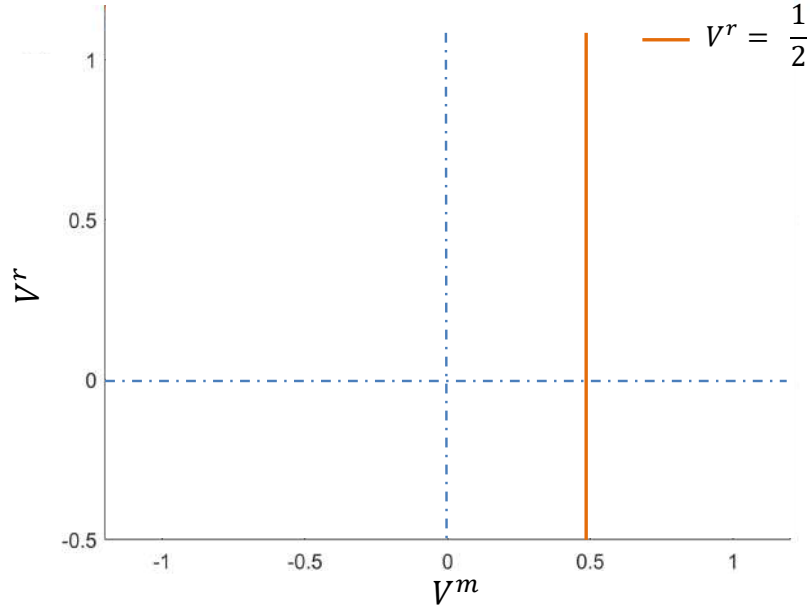
Figure 4-4: Solvability boundary (solid line) $V^r = 1/2$ in the V^r V^m plane.

in PQ plane. using the transversality condition i.e., $V^R = 1/2$ and (4.13) we can write can conclude solvability boundary as,

$$Q = P^2 - \frac{1}{4} \tag{4.15}$$

The parabolic solvability boundary define by (4.15) is shown in Fig.4-5. Now let us find the boundness on power injection P and Q defined by λ in the direction specified by an angle θ.

$$P = \lambda \cos \theta , \quad Q = \lambda \sin \theta . \tag{4.16}$$

For convenience the starting point is chosen as $P^0 = Q^0 = 0$ (i.e., origin in PQ space),

$$P = \lambda \cos \theta = V^m \tag{4.17a}$$

$$Q = \lambda \sin \theta = (V^r)^2 + (V^m)^2 - V^r \tag{4.17b}$$

$$g(x) = 1 - 2V^r \tag{4.17c}$$

57
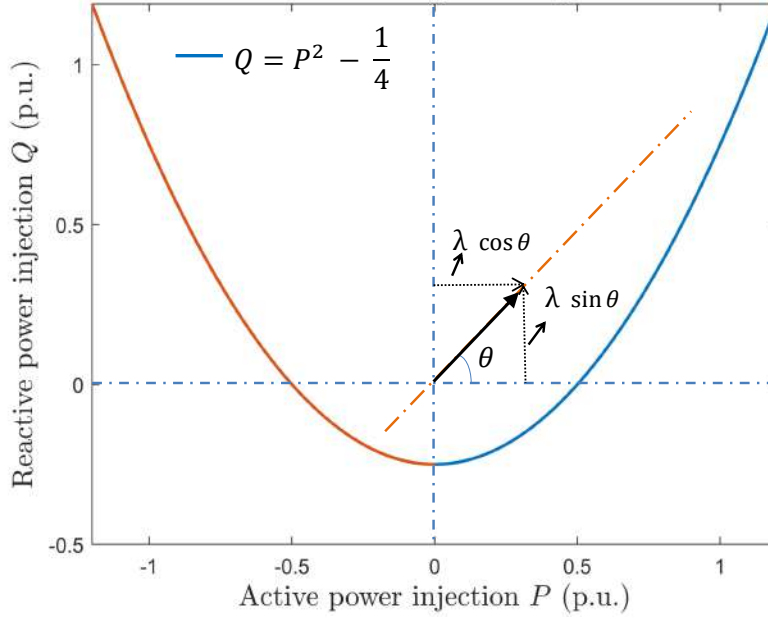
Figure 4-5: Solvability boundary (solid line) $Q = P^2 - 1/4$ in the PQ plane and the direction vector (dashed line) $P = \lambda \cos \theta$, $Q = \lambda \sin \theta$. For any θ dashed line never crosses the solvability boundary (solid line) tangentially. Accordingly $\mathcal{J}$ is never degenerate on the solvability bounary $g(x) = \det \ J = 0$.

The extended Jacobian $\mathcal{J}$ is readily found,

$$
\mathcal{J} = \begin{pmatrix} 0 & 1 & -\cos \theta \\ 2V^r - 1 & 2V^m & -\sin \theta \\ -2 & 0 & 0 \end{pmatrix} . \tag{4.18}
$$

It is clear that at the solvability boundary, where $V^r = 1/2$ and the Jacobian $g = \det(J) = 0$, the determinant of full Jacobian is in general not equal to zero.

$$
\det (\mathcal{J}) = 2(\sin \theta - 2V^m \cos \theta) . \tag{4.19}
$$

The full Jacobian becomes degenerate only at one special point $V^m = (\tan \theta)/2$. Together with other equations (4.17) this represents a system of equations which has no solutions. This means in our example $\mathcal{J}$ is never degenerate at the solvability boundary $g = \det(J) = 0$. Geometrically this is easy to understand, any straight line

in the PQ plane, which passes through the origin

$$P = \lambda \cos \theta, \quad Q = \lambda \sin \theta, \tag{4.20}$$

crosses the solvability boundary $Q = P^2 - 1/4$ at some angle, but never tangentially (see Fig. 4-5). Finally, we can make an explicit connection with our discussion in previous section. Let us assume $\mathcal{J}$ is degenerate, $V^m = (\tan \theta)/2$, and hence there is a vector $[\Delta V^r, \Delta V^m, \Delta \lambda]^T \propto [0, \cos \theta, 1]^T$ such that

$$\mathcal{J} \begin{pmatrix} 0 \\ \cos \theta \\ 1 \end{pmatrix} \propto \mathcal{J} \begin{pmatrix} \Delta V^r \\ \Delta V^m \\ \Delta \lambda \end{pmatrix} = 0 \ . \tag{4.21}$$

In particular this means $[0, \cos \theta](\partial_x g) = 0$, where $(\partial_x g) = [-2, 0]^T$. In other words, vector $[\Delta V^r, \Delta V^m] = [0, \cos \theta]$ is along the solvability boundary in the $V^r \ V^m$ plane. Accordingly, vector

$$\begin{pmatrix} \Delta P \\ \Delta Q \end{pmatrix} \equiv J \begin{pmatrix} 0 \\ \cos \theta \end{pmatrix} = \tag{4.22}$$

$$\cos \theta \begin{pmatrix} 1 \\ 2V^m \end{pmatrix} = \cos \theta \begin{pmatrix} 1 \\ 2P \end{pmatrix} \tag{4.23}$$

is tangential to the solvability boundary $Q = p^2 - 1/4$. At the same time this vector has to be proportional to the loadability direction (4.20),

$$\begin{pmatrix} 1 \\ 2p \end{pmatrix} \propto \begin{pmatrix} \cos \theta \\ \sin \theta \end{pmatrix} \ . \tag{4.24}$$

In our example this does not happen, i.e. the system of equations (4.17), supplemented by the equation $g = 0$ and (4.24) has no solutions.

59

4.6 Types of Transversality Conditions

There are various ways to enforced transversality condition $g(x)$ that guarantee that the Jacobian matrix J is singular at point x if and only if $g(x) = 0$. From algorithmic purposes, it is essential that both the function $g(x)$ and its derivatives $\partial g / \partial x_i$ can be efficiently computed with high accuracy. Moreover, it is desirable for function $g(x)$ to possess well-behaved gradients that would increase the region of convergence of iterative Newton-based algorithms. Some of the contribution toward transversality choices was first explored in [65, 66, 67] by the author, here will briefly discuss some of the proposed options from [65, 66] and some new ones proposed here as well. In this work we consider following possible choices of transversality constraints.

4.6.1 Eigenvector transversality condition

Normally, $g(x)$ Jacobian singularity condition is enforced through the "vector transversality condition", where the power flow equations are complemented with an additional vector equation for the Jacobian kernel, as explained in [13] and [65, 67]. This condition is defined by the introduction of an additional vector variable y that is required to be a normalized eigenvector with zero eigenvalue [13]. In this case, the function g_{eig} that defines this transversality condition becomes multi-dimensional, defined in the following way:

$$g_{\text{eig}}(x, y) = \begin{bmatrix} (\partial_x f) y \\ y^\top y - 1 \end{bmatrix}. \tag{4.25}$$

Here $y \in \mathbb{R}^n$ and the equation $g_{\text{eig}}(x, y) = 0$ ensures that $(\partial_x f)$ has non-trivial kernel i.e. it is degenerate. The details about the extended Jacobian of this transversality condition are provided in [13]. The key advantage of this approach is that it preserves sparsity. However, the convergence is achieved at the price of increasing the number of variables by approximately a factor of two. Moreover, the algorithm is also reliant on additional heuristic producing a good initial guess for the eigenvector. An algorithm

based on g_{eig} might work well in combination with CPF algorithm, as the convergence depends mainly on the good initial guess of y, as shown in [13].

Another type of algorithm that can be classified as eigenvector transversality algorithm is based on the nonlinear formulation of the loadability problem [45]. The approach also introduces a vector y, which is Lagrangian-dual to the power flow equations with the full Lagrangian taking the form

$$L(\lambda, x, y) = \lambda + y^\top f(x, \lambda) . \tag{4.26}$$

At the optimal point, the KKT conditions $\partial_x L = (\partial_x f)^\top y = 0$, $\partial_\lambda L = 1 + y^\top(\partial_\lambda f) = 0$ and $\partial_y L = f = 0$ are satisfied. Thus solving the KKT system is equivalent to imposing additional transversality constraints $(\partial_x f)^\top y = 0$ and $1 + y^\top(\partial_x f) = 0$ on top of the usual power flow equations $f = 0$. Moreover, at the optimum y coincides with the left eigenvector (corresponding to zero eigenvalue) of the power flow Jacobian $\partial_x f$. Hence, in the language of this work, the non-linear programming formulation is equivalent to introduction of the following transversality condition

$$g_{\text{nlp}}(x, y) = \begin{bmatrix} (\partial_x f)^\top y \\ 1 + y^\top(\partial_\lambda f) \end{bmatrix} . \tag{4.27}$$

The formulation based on g_{nlp} has a natural advantage of being linked to the well-developed theory of nonlinear programming, hence the opportunity to utilize the modern nonlinear programming solvers. However, from the theoretical perspective it falls into the same category as the g_{eig} based approach described above with the same intrinsic deficiency of nearly doubling the number of involved variables. The expressions for calculating gradient of g_{eig} are provided in [13].

4.6.2 Determinant Transversality $g_{\text{det}}(x)$

Our first and most obvious choice, denoted as $g_{\text{det}}(x)$ is simply the determinant of the matrix J, i.e. $g_{\text{det}}(x) = \det(J)$. Given the Jacobian of the original system of equations, it's determinant can be efficiently acquired using one of the usual matrix

decomposition. For example, given the eigenvalue decomposition $J = O\Lambda O^{-1}$ with diagonal eigenvalue matrix , the value of $\det(J(x))$ is given by:

$$g_{\det}(x) = \prod_k \lambda_k \tag{4.28}$$

In practice, a more efficient implementation of the determinant calculation procedure can be based on the LU or QR decompositions of the matrix J. The determinant of the Jacobian is the most natural measure of singularity, and algorithms based on this choice of transversality condition are relatively easy to implement and show respectable performance as demonstrated in this chapter. At the same time, as the value of the determinant is a product of all eigenvalues, the gradients of $g(x)$ may not necessarily point to the direction of the closest singular boundary. Instead, they may reflect the direction of highest average sensitivity of system eigenvalues. It is therefore, useful to derive other transversality conditions with potentially better behavior. Here we consider how gradient of the determinant i.e., $g'_{\det}$ can be efficiently computed using the well-known Jacobi's formula:

$$\frac{\partial g(x)}{\partial x} = \lim_{x \to 0} \frac{\det(J + \delta J) - \det(J)}{\delta x} = \tag{4.29a}$$

$$\lim_{x \to 0} \frac{\det(J(1 + J^{-1}\delta J)) - \det(J)}{\delta x} \tag{4.29b}$$

$$= \lim_{x \to 0} \det(J)\mathrm{Tr}\left(J^{-1}\frac{\partial J}{\partial x}\right) \tag{4.29c}$$

And finally, we can conclude,

$$\frac{\partial g(x)}{\partial x} = \mathrm{Tr}\left(\mathrm{adj}(J)\frac{\partial J}{\partial x}\right) \tag{4.30}$$

Expression (4.30) also contains the adjugate matrix of the Jacobian $\partial_x f$. Implementation of adjugate matrix construction algorithm is given in next section. We explain two approaches for calculation of the adjugate matrix.

4.6.2.1 Classical Approach for $\text{adj}(J)$:

Normally, the adjugate of Jacobian $\text{adj}(J)$ of a square matrix is defined as the transpose of its cofactor matrix,

$$\text{adj}(J) = C^\top \tag{4.31}$$

Here, $J = [J_{ij}]$ is an $n \times n$ Jacobian matrix. For each entry J_{ij} the corresponding entry in cofactor matrix is,

$$C_{ij} = (-1)^{i+j} |M_{ij}| \tag{4.32}$$

In (4.32), M_{ij} is a $(n-1) \times (n-1)$, which is defined by removing i^{th} and j^{th} row of matrix J. Calculating adjugate through 4.31 suffers from higher computational burden, therefore in the next section a more scalable approach is presented.

4.6.2.2 Modified LU Decomposition for $\text{adj}(J)$

The dilemma with $\text{adj}(J)$ is that we need to compute the adjugate matrix for Jacobian, i.e., $\text{adj}(J)$ which is defined via an inverse of Jacobian. At the feasibility boundary, as the Jacobian becomes singular, calculating the inverse of Jacobian near that point is computationally challenging. Here, the LU decomposition approach is used as an efficient approach for inverting the J matrix by factoring into lower and upper triangular matrices. This decomposition allows us to formulate a simple linear algebraic strategy that avoids computing inverse of the Jacobian matrix. $PJ = LU$ gives the LU decomposition of J. We can adjust the LU decomposition of J by introducing an additional intermediate diagonal matrix D such that $PJ = \hat{L}D\hat{U}$ with following entries:

$$D = [L_{ii}U_{ii}] \quad \text{and} \quad \hat{L}_{ii} = \hat{U}_{ii} = 1 \tag{4.33a}$$

$$\hat{L} = [L_{ji}/L_{ii}] \quad \text{and} \quad \hat{U} = [U_{ij}/U_{ii}], \quad i \neq j \tag{4.33b}$$

One can easily show that the determinants of matrices J and D will be the same: $\det(J) = \det(D) = \prod_i D_{ii}$. The adjugate of matrix J can be naturally expressed through adjugate of D which itself is diagonal with simply defined matrix elements:

63

$\mathrm{adj}(D)_{kk} = \prod_{i \neq k} D_{ii}$, or more formally:

$$\mathrm{adj}(J) = \det(J)J^{-1} \tag{4.34a}$$

$$J^{-1} = \hat{U}^{-1}D^{-1}\hat{L}^{-1}P, \quad \det(J) = \det(D) \tag{4.34b}$$

Thus:

$$\mathrm{adj}(J) = \hat{U}^{-1}\mathrm{adj}(D)\hat{L}^{-1}P \tag{4.35}$$

We can summerize the algorithm for calculating sensitivity of det J as follow,

---

Algorithm 1 Sensitivity of g_{det}

---

    function $\mathrm{RS}(J', L, U, P)$
        $\hat{L} \leftarrow [L_{ji}/L_{ii}]$
        $\hat{U} \leftarrow [U_{ij}/U_{ii}]$
        $D \leftarrow [L_{ii}U_{ii}]$
        adj $J \leftarrow \hat{U}^{-1}\mathrm{adj}(D)\hat{L}^{-1}P$
        $g'_{\mathrm{det}} \leftarrow ((\mathrm{adj}\ J)J')$
        return g'_{det}
    end function

The determinant of a matrix is the most natural measure of singularity. Hence obvious choice of transversality is through (3.2). This condition is easy to implement, but at the same time computationally expensive and sensitive to numerical perturbation, according to [56, 65] this condition is also not scalable for large systems. Thus, work proposed here explore possible choices.

4.6.3 LU based Transversality

The condition $g_{\mathrm{LU}}(x) = 0$ based on the LU decomposition is defined using the very same $\hat{L}D\hat{U}$ decomposition from (4.33). Whenever J is singular, the LU decomposition has a zero pivot on the diagonal of U or D in this case [68]. Using the pivoting strategy from [68] it is possible to ensure that the zero pivot will appear in the lower right element of D, i.e. $D_{nn} = U_{nn} = 0$. Thus, D_{nn} can be used as insolvability criteria as $g_{\mathrm{LU}}(x) = D_{nn}$. To simplify the notations we consider the sensitivity with respect to some arbitrary parameter μ such that $J' = dJ/d\mu$. For $PJ = \hat{L}D\hat{U}$ the element D'_{nn}

is defined as follows:

$$P'J + PJ' = \hat{L}'D\hat{U} + \hat{L}D'\hat{U} + \hat{L}D\hat{U}' \tag{4.36}$$

We can rewrite above expression using following properties: P' is a null matrix and $\hat{L}^{-1}\hat{L} = \hat{U}\hat{U}^{-1} = 1$:

$$\hat{L}^{-1}PJ'\hat{U}^{-1} = \hat{L}^{-1}\hat{L}'D + D' + D\hat{U}'\hat{U}^{-1} \tag{4.37}$$

It can be understood from matrix algebra that expression $\hat{L}^{-1}\hat{L}'D$ and $D\hat{U}'\hat{U}^{-1}$ are lower and upper triangular matrices respectively with zeros on the diagonal. Thus, D'_{nn} is equal to:

$$g'_{\text{LU}} = D'_{nn} = (\hat{L}^{-1}PJ'\hat{U}^{-1})_{nn} \tag{4.38}$$

Hence, the full algorithm for finding D_{nn} can be summarized as:

Algorithm 2 Sensitivity of D_{nn}

---
    function RS(J', L, U, P)
        $\hat{L} \leftarrow [L_{ji}/L_{ii}]$
        $\hat{U} \leftarrow [U_{ij}/U_{ii}]$
        $D \leftarrow [L_{ii}U_{ii}]$
        $D'_{nn} \leftarrow (\hat{L}^{-1}PJ'\hat{U}^{-1})_{nn}$
        return D'_{nn}
    end function

4.6.4 QR based Transversality

Third transversality condition $g_{\text{QR}}(x) = 0$ is based on the $J = QR$ decomposition of the Jacobian. Here the matrix Q is an orthogonal matrix composed of n orthonormal vectors $Q = [q_1 \cdots q_n]$. R is an upper-triangular matrix. The QR decomposition is simply a matrix representation of the Gram-Schmidt orthogonalization procedure, that transforms the basis composed of the columns of the matrix J defined by a_k in an orthonormal basis defined by the columns of Q denoted as q_k. The orthogonalization is performed by choosing $q_1 = a_1/|a_1|$ and consequent projection of the vectors a_k on

the subspace normal to the span of $q_1 \ldots q_{k-1}$. Whenever the Jacobian matrix $[\partial_x f]$ is close to being singular, the lower right element R_{nn} of the matrix R is close to zero.

Since the value R_{nn} becomes zero at the solvability boundary it is natural to use it as insolvability criterion, i.e. $g_{\mathrm{QR}} = R_{nn}$. The QR decomposition is an extremely thoroughly studied algorithm, selected to be one of the 20 most important algorithms of 20th century [69]. The value of R_{nn} can be efficiently computed for sparse matrices J appearing in power system context [70]. In comparison to other decompositions, QR is especially appropriate for dealing with nearly singular matrices where the more popular LU decomposition may be overly sensitive to numerical errors [71].

Considering the same notation as from previous section i.e. $J' = dJ/d\mu$ we can define sensitivity of R'_{nn} as follows. Assuming that $J = QR$ we have

$$J' = Q'R + QR' \tag{4.39}$$

Here the matrix R is not singular, this relation can be rewritten in the following form:

$$Q^\top J' R^{-1} = Q^\top Q' + R' R^{-1} \tag{4.40}$$

Note, that the first term $Q^\top Q'$ in the right hand side of (4.40) is antisymmetric as can be easily seen by differentiation of the relation $Q^\top Q = 1$. Since both R' and R^{-1} are upper triangular one has $(R'R^{-1})_{nn} = R'_{nn} R_{nn}^{-1}$ and $R_{nn}^{-1} R_{nn} = 1$. Hence we have

$$R'_{nn} = (Q^\top J' R^I)_{nn}, \quad R^I = R^{-1} R_{nn}. \tag{4.41}$$

The nn element of $Q^\top J' R^I$ is a product of the bottom row of $Q^\top J'$ and the last column of R^I. Although R^I is defined through R, crucially, the last column of R^I is independent of R_{nn}. This follows from the geometric meaning of $R^I_{kn} = r_k$ as a vector orthogonal to all rows of R except the bottom one, with the total length of r normalized such that $r_n = 1$. This definition does not involve R_{nn}, and r remains regular even if $R_{nn} \to 0$. One can either calculate r iteratively, or define an auxiliary

non-singular matrix

$$\tilde{R}_{ij} = \begin{cases} 1 & \text{if } i = j = n \\ R_{ij} & \text{otherwise} \end{cases} \tag{4.42}$$

Then r is the last column of $\tilde{R}^{-1}$ and $g'_{\text{QR}} = (Q^\top J' \tilde{R}^{-1})_{nn}$.

Algorithm 3 Sensitivity of R_{nn}

    function RS(J', Q, R)
        $R'_{nn} \leftarrow (Q^\top J' \tilde{R}^{-1})_{nn}$
        return R'_{nn}
    end function

4.6.5 SVD based Transversality

Finally, the most natural, though computationally expensive choice of the transversaility condition is the condition based on the singular value decomposition (SVD): $g_{\text{svd}}(x) = 0$. For Jacobian J, we can define the SVD decomposition as follows:

$$J = U\Sigma V^\top = \sum_{i=1}^{n} \sigma_i u_i v_i^\top \tag{4.43}$$

Here U and V are $n \times n$ orthogonal matrices. The matrix Σ is a $n \times n$ diagonal consisting of singular values (i.e $\sigma_i \geq 0, i = 1, 2, \cdots, n$) of J on the main diagonal [72].

Also, for any real symmetric matrix A, the individual singular values are the positive square roots of the eigenvalues of $A^\top A$ or $AA^\top$. Additionally, the smallest singular value of J is the $l_2 - \text{norm}$ distance of J to the set of all rank-deficient matrices [73]. Thus, when J becomes singular near the solvability boundary the minimum singular value becomes equal to zero i.e. $\sigma_{nn} = 0$. Hence, we can use σ_{nn} based on SVD as an alternative transversality condition. We can derive an expression for the sensitivity of minimum singular value (i.e. σ'_{nn}) as given below

$$J' = dJ/d\mu = U'\Sigma V^\top + U\Sigma' V^\top + U\Sigma V'^\top, \tag{4.44}$$

67

and rewrite the above expression in the following form:

$$U^\top J'V = U^\top U'\Sigma + \Sigma' + \Sigma V'^\top V \tag{4.45}$$

The terms $U^\top U'\Sigma$ and $\Sigma V'^\top V$ are antisymmetric because $U^\top U'$ and $V'^\top V$ are anti-symmetric and Σ is just a diagonal matrix. Thus, Σ'_{nn} is equal to:

$$g'_{\text{svd}} = \Sigma'_{nn} = (U^\top J'V)_{nn} \tag{4.46}$$

The nn element of $U^\top J'V$ is a product of the bottom row of $U^\top J'$ and the last column of V.

Algorithm 4 Sensitivity of σ_{nn}

---

    function $\text{RS}(J', U, \Sigma, V)$
        $\sigma'_{nn} \leftarrow (U^\top J'V)_{nn}$
        return σ'_{nn}
    end function

Although the derivations for the gradient of g_{LU}, g_{QR} and g_{svd} are somewhat more involved in comparison of gradient of g_{det}, the complexity of implementations are comparable. In general, we propose three new transversality conditions $g_{\text{LU}}, g_{\text{QR}}$ and g_{SVD}, and improve on the g_{det} condition. Transversality enforced Newton-Raphson was implemented with each of these conditions and performance of the algorithm was evaluated in terms of time of convergence, scalability, numerical stability. These results were also compared with the classical vector based transversely choice i.e., g_{eig}.

4.7 Implementation

Apart from the calculations of the transversality condition and its sensitivity, all the steps of the proposed TENR algorithm are similar to traditional Newton-Raphson algorithm. This makes this algorithm simple in terms of implementation compared to CPF or some other methods. The academic prototype of the algorithm was implemented based on MATPOWER [74] package and standard MATLAB based implementation of numerical algebra. Standard IEEE data format was used from power system archives in [75]. Standard MATLAB library was used to compute LU, QR and SVD decompositions. The academic version of the TENR algorithm is available at a public domain [76] for reproducing all the results presented in this paper. For all the test cases, the algorithm was initialized with a base case solution corresponding to $\lambda = 0$ that was obtained from normal power flow equations.

There are several ways to assess the convergence of the algorithm to the boundary of feasibility and solvability sets. To allow for natural comparison between different algorithms and different models we use the universal stability index based on the singular value decomposition of the Jacobian matrix: $J = U \Sigma V^\top$ with orthogonal matrices U and V and diagonal matrix Σ. The smallest element $\sigma_{\min}$ of the matrix Σ becomes zero at the solvability boundary and is a natural and numerically stable measure of the distance to solvability boundary. To facilitate comparison between different models with highly different magnitudes of $\sigma_{\min}$ we use the relative value of $\sigma_{\min}$ yielding the following stability index:

$$\text{Stability Index} = \frac{\sigma_{\min}(\tau)}{\sigma_{\min}(0)} \tag{4.47}$$

Here τ denotes the number of a Newton-Raphson iteration. This stability index is equal to 1 when the algorithm is initialized and gradually decreases to zero as the system approaches the boundary of the solvability or feasibility set.

69

4.8 Summary

A standard formulation for calculating just a point on the solution boundary (i.e., either solvability or feasibility boundary) is provided. Then, a generalization is given to characterize the solution on the boundary of solvability or solvability through transversality condition. This chapter also introduces a novel algorithm referred to as "Transversality Enforced Newton-Raphson," with an explicit proof of convergence. Finally, different transversality choices are also proposed with better numerical stabilities, along with fast algorithms to compute their gradients as well.

Chapter 5

Numerical Studies I: Characterizing a Point on the Feasible Space

The framework of this chapter covers a detailed computational performance of the Transversality Enforced Newton-Raphson algorithm. A broad range of problems is considered, such as maximum loadability, transfer capability to assess the computational execution of the proposed TENR algorithm with a different choice of transversality conditions.

5.1 Three Bus System

In this first example, we consider a three bus system to validate the results reported in [13]. Let's consider a three bus test network as depicted in Fig.5-1 with the following settings. Bus 1 as slack bus with voltage phasor $\hat{V}_1 = 1.0\angle 0°$. Bus 2 as PV bus with voltage set point $\hat{V}_2 = 1.0\angle\delta_2$, while active and reactive power injections are P_2^{inj} and Q_2^{inj} respectively. Whereas the real and reactive power injections at bus 3 are represented by P_3^{inj} and Q_3^{inj}, with complex voltage phasor denoted as $\hat{V}_3 = V_3\angle\delta_3$. Also, all the line in the network are lossless with inductance set to $X_{12} = X_{13} = X_{23} = 1.0$ (p.u.). We have conceived two distinct scenarios based on the status of bus
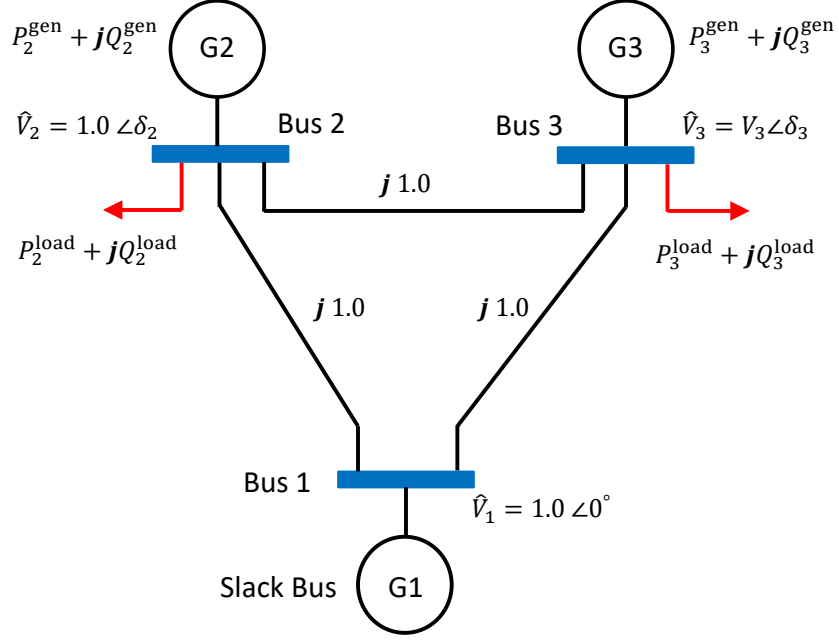
Figure 5-1: Three bus network.

3, first as PV and later as PQ bus.

5.1.1 First Scenario

In this scenario, bus 3 treated as PV bus with voltage set point $\hat{V}_3 = 1.05\angle\delta_3$. Based on the network settings discussed previously, the solution boundary is confined by $P_2^{\text{inj}} - P_3^{\text{inj}}$ space. Figure.5-2 shows the solvability boundary in P_2^{inj} P_3^{inj} plane. We first discretize the grid as,

$$P_3^{\text{inj}} = \lambda\cos\theta \tag{5.1a}$$

$$P_2^{\text{inj}} = \lambda\sin\theta \tag{5.1b}$$

and then for each discretize direction TENR algorithm was initiated to compute the point on the actual boundary. An approximate boundary is displayed in Fig.5-2; it is created by interpolating between boundary points.
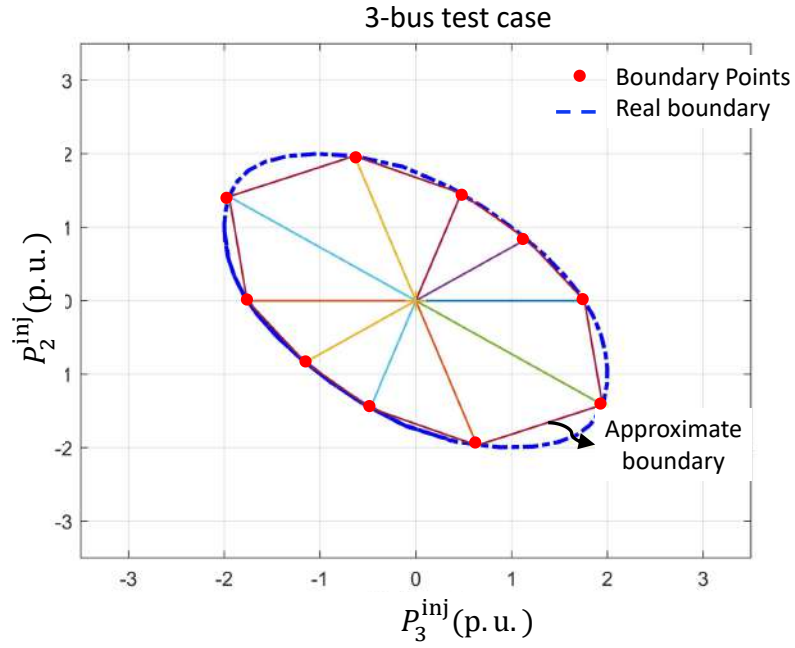
Figure 5-2: Approximate to solvability boundary in P_2^{inj} P_3^{inj} (scenario 1).
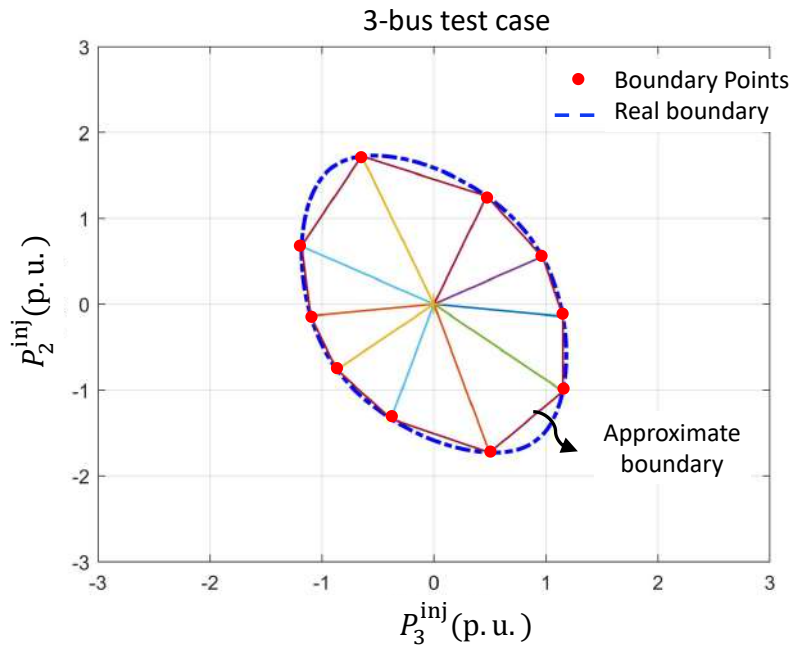
Figure 5-3: Approximate to solvability boundary in P_2^{inj} P_3^{inj} (scenario 2).

5.1.2 Second Scenario

In the second scenario, bus 3 is treated as PQ bus with voltage set point $\hat{V}_3 = V_3 \angle \delta_3$. Therefore, solution space is confined by $P_2^{\text{Inj}} - P_3^{\text{Inj}} - Q_3^{\text{Inj}}$. A similar procedure is adopted to compute boundary points in $P_2^{\text{inj}} P_3^{\text{inj}}$ space while restricting the $Q_3^{\text{inj}} = 0$. The Fig.5-3 shows approximate boundary, area confined by this boundary is smaller than the one from Fig.5-2, as the bus 3 is a PQ bus and thus the voltage magnitude at this bus is not fixed anymore.

To sum up, the TENR algorithm can find a point on the solution boundary, but the approach presented here in terms of discretization of the solution plane is not a systematic approach because of the following reasons. i) Inability to determine inner folds or different solution branches. ii) Computationally expensive may require a lot of discrete directions to capture the boundary curve fully. iii) It may not work well if the boundary is non-convex. iv) Finally, this approach is not tractable for large networks. Therefore, a more systematic procedure is essential to calculate the solution boundary curve with precision, speed, and better implementation.

The context of the numerical results presented here will focus on using the TENR algorithm to compute just a point on the feasible space. In subsequent sections, several sub-problems are devised for the IEEE test networks to demonstrate the computational performance of the TENR algorithm.

5.2 Maximum Loadability

First set of results are given for maximum loadability in the power system, it is defined as the ability of the network to operate with the maximum amount of power injections without compromising the stability and operational constraints [77, 78]. Experiments for maximum loadability considered the following settings, increasing active load and generation, and also reactive load at each bus in the network proportional to the base case. In a realistic operation, the maximum loadability problem requires enforcing a

positive loadability condition such that

$$f_i(x, \lambda) = 0, \qquad i = 1, 2, \ldots, n \tag{5.2a}$$

$$g(x) = 0 \tag{5.2b}$$

the solution of system of equation in (5.2) is obtained for loadability parameter $\lambda > 0$.

5.2.1 Enforcing positive loadability

There is a theoretical possibility that TENR algorithm might converge to undesirable solution, as system in (3.3) may have solutions at both positive and negative values of λ. In practical situations, typically only the $\lambda > 0$ is meaningful and desirable outcome of the analysis. These kind of issues have been reported in [38], although we never encountered such situations in our numerical experiments. Below, we propose two approaches for dealing with this problem.

- The first strategy is based on the modification of the transversality equation $g(x)$ to the form

$$e^{\rho(\lambda)} g(x) = 0 \tag{5.3}$$

with some weight function $\rho(\lambda)$. Obviously, this modification does not introduce any new solutions, and any solution of the new system is a solution of the original as well. In this case the equations for the Newton step modify into

$$f + J\Delta x + (\partial_\lambda f)\Delta \lambda = 0, \tag{5.4a}$$

$$g + (\partial_x g)^\top \Delta x + (\partial_\lambda \rho)\Delta \lambda = 0, \tag{5.4b}$$

and the solution for single step $\Delta \lambda$ becomes

$$\Delta \lambda = \frac{g - (\partial_x g)^\top J^{-1} f}{(\partial_x g)^\top J^{-1}(\partial_\lambda f) - \partial_\lambda \rho} \tag{5.5}$$

We see that the only difference with the original case is presence of $-\partial_\lambda \rho$ in the denominator. By choosing an appropriate function $\rho(\lambda)$ such that $-\partial_\lambda \rho$ is

sufficiently large we can make $\Delta\lambda$ positive at first few iterations. A possible convenient heuristic would be to choose $\rho = -\kappa\lambda$ with sufficiently large $\kappa > 0$ or increase it whenever the algorithms steps in the region of negative λ.

- An alternative strategy is based on the slack variables approach. In order to avoid the algorithm finding the negative loadability solutions, one can enforce an additional condition that ensures that only positive values of λ constitute a valid solution of the problem, i.e.

$$\lambda - t^2 = 0 \ . \tag{5.6}$$

Here t is a slack variable, which will have a real solution only if $\lambda > 0$.

5.2.2 IEEE 14 and 30-bus systems

Different loading scenarios were tested on an IEEE 30-bus network [75]. These scenarios were used to analyze performance, robustness and numerical instabilities encountered by the algorithm for different choices of transversality conditions i.e g_{det}, g_{LU}, g_{QR}, g_{svd} and g_{eig}. One of the scenarios following the analysis in [64] is described below.

In this case both active and reactive load were increased on each bus in the network proportional to the base case. To compensate for the growth of the load, the active generation was also increased on each bus proportional to the base case [33]. The stability limit was reached with $\lambda^* = 4.478$, confirming the results in [33]. It was also observed that for all loading scenarios, the TENR algorithm maintained stability for all the choices of transversality conditions: g_{LU}, g_{QR}, g_{svd} and g_{eig}. But g_{det} transversality choice resulted in more iterations. Results were also compared with the Continuation Power Flow (CPF) algorithm for validation.

Fig. 5-4 shows the trajectory of the stability index (4.47) for all five transversality conditions with respect to the number of Newton iterations. It can be observed that the number of iterations required for convergence based on LU, QR, SVD and eigenvector transversality conditions is smaller in comparison to one based on deter-

minant, which takes a slow start at the beginning and then takes large jumps near the solvability boundary. The large number of iterations in the determinant transversality choice is mainly due to the ill-conditioned nature of the Jacobian (i.e. $\mathcal{J}$) and thus requires an explicit matrix inversion techniques for computing a good inverse.

In conclusion the LU, QR, SVD and eigenvector transversality conditions perform
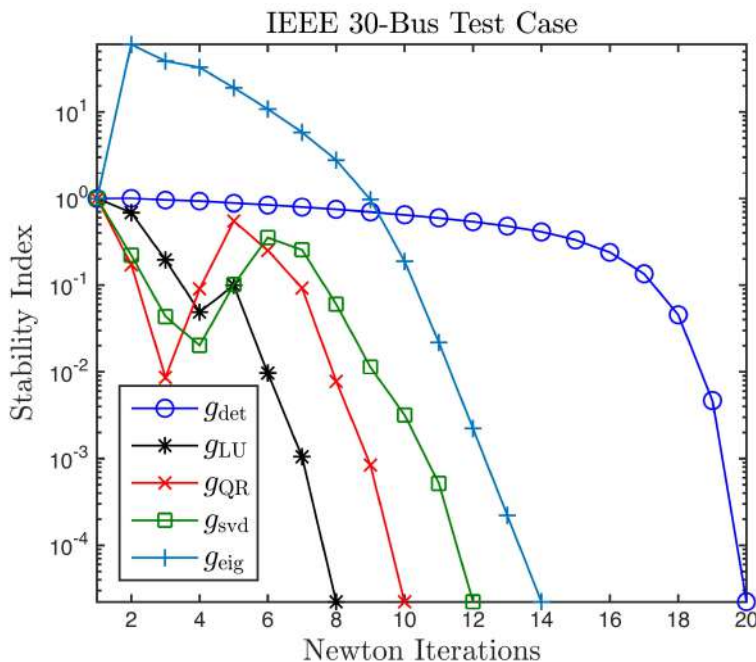
Figure 5-4: Convergence plot for IEEE 30-bus.

better than the determinant in terms of number of Newton iterations. During the simulations, it was also noticed that for g_{det} choice, an adjustment of Newton step size (i.e. α) was required for convergence, which was based on extensions of the ideas discussed in [59, 63]. Whereas, algorithm based on g_{LU}, g_{QR}, g_{svd} and g_{eig} transversality conditions didn't require any explicit adjustment for α.

Fig. 5-5 shows the convergence for an IEEE 14-bus system [75], which was analyzed with all transversality conditions and subjected to voltage magnitude constraints (3.24) as well. The bound to voltage magnitude limit was kept in $\pm 5\%$ to the nominal voltage magnitude. Fig. 5-5 shows that the algorithm still converges with fewer iterations, whereas LU, QR, SVD and eigenvector transversality choices are still better than the determinant. In the subsequent section, different large networks were

77
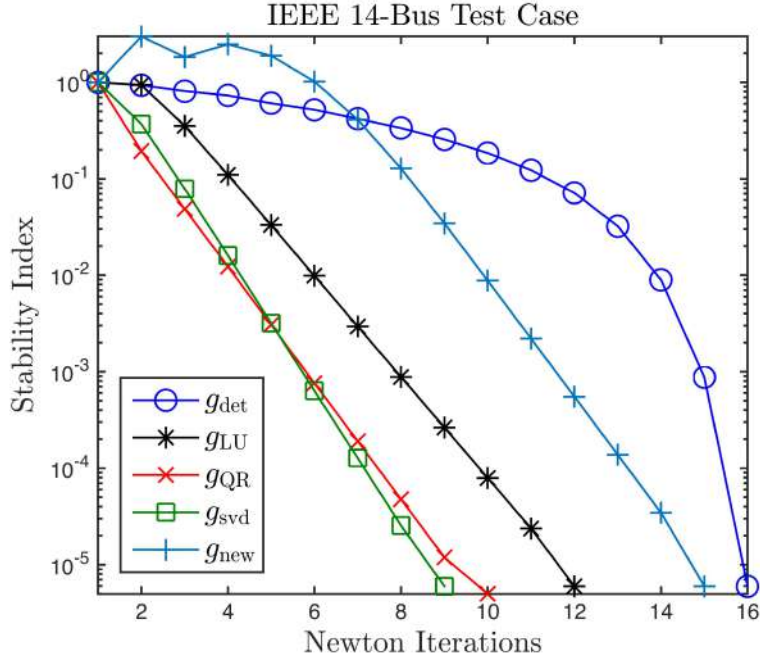
Figure 5-5: Convergence plot for IEEE 14-bus with voltage limit constraint.

also solved in order to observe the scalability and overall performance.

5.2.3 Large test networks

This section presents the results from different large test networks. These results were used to assess the scalability and the numerical stability of the TENR algorithm.

5.2.3.0.1 IEEE 118 and 300-bus system

Analysis of the 118 and 300-bus networks [75] is a natural way to assess the scalability of the algorithm. These systems were subjected to the same loading conditions as in the 30-bus case. Both active and reactive load and active generations were increased on each bus in the network proportional to the base case. The 118-bus test case was also subjected to the voltage magnitude limit bound of $\pm 5\%$ of the base level. Larger systems are more prone to numerical instabilities as a large number of equations are required to be solved, due to the size of the network. This causes the extended Jacobian matrix (i.e., $\mathcal{J}$) to become poorly conditioned for g_{det} choice of transversality. Likely this effect is related to numerical sensitivity of computing $\partial_x g$

based on Jacobi's formula (4.30).

Fig. 5-6 shows the trajectory of the stability index for 118-bus based on LU, QR, SVD and eigenvector transversality conditions, here Fig. 5-7 shows the trajectory of the stability index for 300-bus based on LU, QR and SVD transversality conditions. It was observed that, as the size of the network increases the convergence for g_{det} gets very bad such argument was also presented in [65], so the results for g_{det} are not included for 118 and 300-bus systems. This could be related to non-monotonic behavior of the determinant in the vicinity of loadability limits. Also for the further increase in the size of the network from 118 to 300-bus system, the performance for g_{eig} also suffers and requires a very good initial guess for the eigenvector for the convergence.
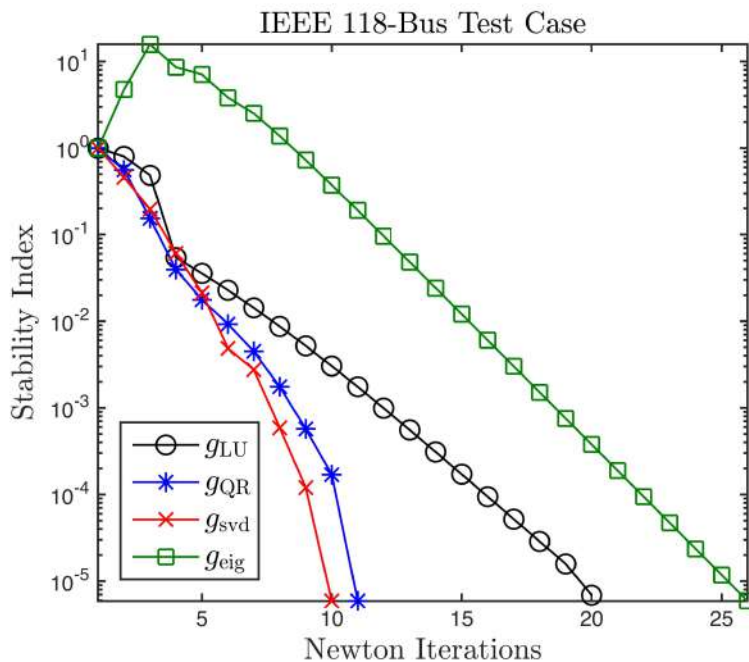
Figure 5-6: Convergence plot for IEEE 118-bus

5.2.3.0.2 Polish 2383-bus system

A large Polish 2383-bus test network was also analyzed for the assessment of the scalability and performance. The details about this Polish 2383-bus network can be found in [74]. The loading conditions were kept the same as for 30-bus test case.
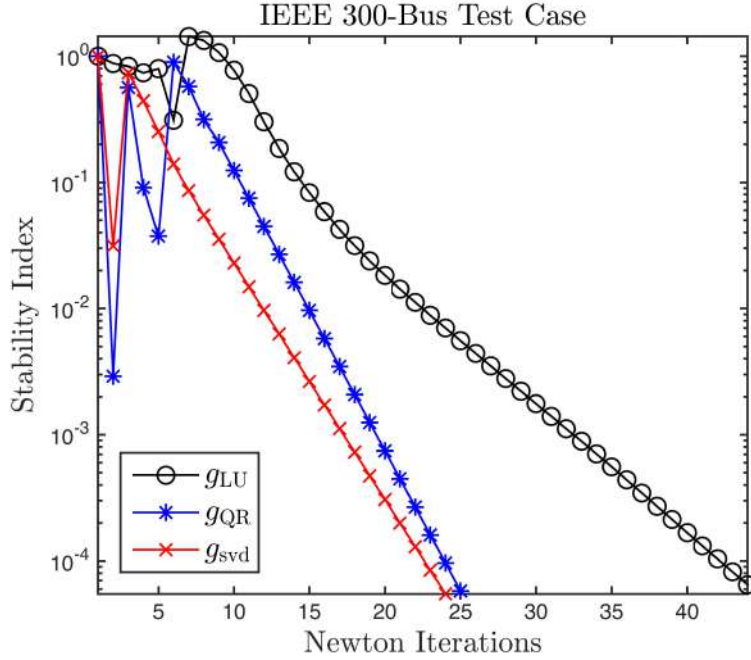
Figure 5-7: Convergence plot for IEEE 300-bus

Fig. 5-8 shows the trajectory of the stability index only for QR, SVD and eigenvector transversality conditions, as the other choices resulted in large number of iterations. From simulations, it was noticed that the LU transversality condition becomes gradually worse in terms of number of iterations as the size of the network increase, this behavior might be a result of computing sensitivity of g'_{LU} using (4.38). The behavior of g_{eig} was similar to LU condition, it was mainly because this transversality choice becomes more prone to good initial guess for the eigenvector, as the size of the system increases.

A brief summary of the results for different IEEE test cases is presented in Table 5.1 and Table 5.2 and all the experiments were performed with three digit precision. Table 5.1 shows the values of λ^* obtained for different IEEE networks without voltage feasibility constraints, in order to provide a comparison of accuracy of TENR algorithm with a CPF algorithm. Here τ_{LU}, τ_{QR}, τ_{svd} and τ_{eig} denote the number of iterations for TENR algorithm based on LU, QR, SVD and eigenvector transversality conditions respectively.

Results for g_{det} is not reported here as explained in section 4.6.2. All the test
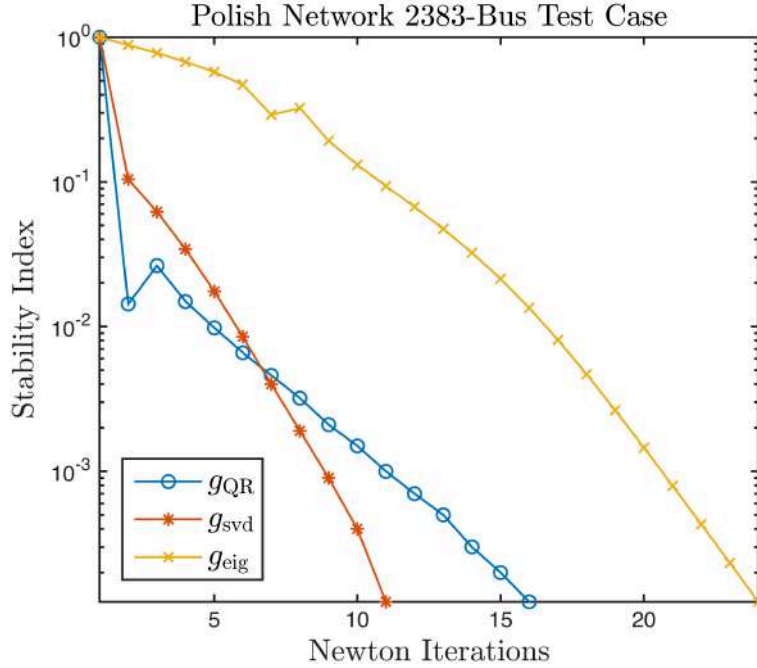
Figure 5-8: Convergence plot for Polish 2383-bus network.

cases in Table 5.2 were also subjected to voltage feasibility constraints of $\pm 5\%$ to the nominal voltage magnitude (i.e. 1 p.u.) for which the base regime (i.e $\lambda = 0$) also satisfies the $\pm 5\%$ voltage constraints. It can be observed from Table 5.1 and Table 5.2 that the size of the network greatly affects the rate of convergence for g_{LU} and g_{eig}, but for g_{QR} and g_{svd} the overall number of iterations and performance doesn't depend too much on the size of the network. Also, large test cases required an adjustment for Newton step size α for the convergence.

Table 5.1: Summary for different IEEE test networks (without voltage feasibility constraints)

IEEE Cases	λ^*	τ_{LU}	τ_{QR}	τ_{svd}	τ_{eig}
14 Bus	3.060	12	9	9	15
30 Bus	4.478	12	8	11	15
118 Bus	2.187	20	16	14	22
300 Bus	0.430	29	23	15	25
2383 Bus	0.894	37	16	11	24
3120 Bus	1.331	34	21	12	25

Table 5.2: Summary for different IEEE test networks (with voltage feasibility constraints)

IEEE Test Cases	λ^*	τ_{LU}	τ_{QR}	τ_{svd}	τ_{eig}
9 Bus	0.9275	14	11	13	16
14 Bus	2.3372	12	10	8	15
30 Bus	2.2909	16	7	10	17
39 Bus	1.03595	19	11	12	21
300 Bus	0.1355	22	11	10	27

5.2.4 Reactive Power Limits on Generators

In practical situations, the generators have some limits on the reactive power they can produce, and usually those limits are achieved before the system reaches the loadability limit. In this section, we describe the extension of the TENR algorithm that allows for natural incorporation of the generator reactive power constraints.

We have implemented the extension of our algorithm (see chapter 3) and tested it on the standard IEEE cases. Here we also discuss the implementation on a IEEE 14 bus test case [74], the loading conditions were kept the same as in section 5.2. The stability limit was reached with $\lambda^* = 0.778$ (with reactive power limit enforced) and all the generators buses violated the maximum reactive generation limit defined in (3.27). Table 5.3 shows the details for this 14-bus case, here $|\overline{V}_i|$ denotes voltage magnitude for generator buses with $\lambda = 0$ and $|\underline{V}_i|$ describes voltage magnitude for generator buses with $\lambda = \lambda^*$, while t_i, c_i are the slack variables from reactive power limits constraints.

Table 5.4 shows results for different IEEE test cases (for 118-bus test case slightly modified Q limits were used) when generator reactive power limits are considered (without bound on voltage magnitude on PQ buses), it was also observed that the overall number of iterations remains roughly the same as in the case when limits are ignored. The obtained values of λ^*_{TENR} (from TENR algorithm) match with λ^*_{CPF} obtained using CPF algorithm from the PSAT-CPF Toolbox [79].

Table 5.3: Summary of results for IEEE 14-bus cases (reactive power limit enforced)

Generator	$|\overline{V}_i|$	$|\underline{V}_i|$	c_i	t_i
2	1.0450	0.937	0.000	-0.144
3	1.0100	0.893	0.000	-0.222
6	1.0700	0.891	0.000	-0.351
8	1.0900	0.911	0.000	-0.359

Table 5.4: Comparison of λ^* obtained from TENR and Continuation Power Flow (reactive power limit enforced)

IEEE Test Cases	λ^*_{TENR}	λ^*_{CPF}
14 Bus	0.778	0.777
30 Bus	0.551	0.545
57 Bus	0.616	0.613
118 Bus	1.091	1.077
300 Bus	0.059	0.058
2383 Bus	0.052	0.082

5.3 Total Transfer Capability

Assessment of transfer capability margin plays a vital role in the economic part of the power system market [80, 81]. Generally, transfer capability term defines the amount of power that can be transferred through an electrical power system from one place to another, while transfer or capability margin describes the maximum amount of transferable power without compromising the security or feasibility constraints [82]. The problem formulation is conceptually similar to (5.2), except here the power injections are increased only at the source and sink buses in the network. Then, the Total Transfer Capability (TTC) is calculated through,

$$\text{TTC} = \sum_{i \in \text{sink}} P_i^{\text{load}}(\lambda^*) - \sum_{i \in \text{sink}} P_i^{\text{load}}(0) \tag{5.7}$$

In (5.7), $\sum_{i \in \text{sink}} P_i^{\text{load}}(\lambda^*)$ represents sum of load at sink area when $\lambda = \lambda^*$, while $\sum_{i \in \text{sink}} P_i^{\text{load}}(0)$ denotes the sum of load at sink area when $\lambda = 0$.

5.3.1 IEEE 14-bus system

A small test case is considered in details for better understanding and to illustrate the potential of TENR algorithm for calculating the transfer capability margin.The IEEE 14 bus test case consists of four generator (PV) buses, nine load (PQ) buses and bus one as slack/swing bus. Several scenarios were analyzed with different transfer directions and for each of these scenario problem defined by (5.2) was solved for finding λ^*. In this example, for a given transfer direction the problem described by (5.2) was solved i) first without any feasibility constraints and λ in this case is denoted by λ_1^*, ii) gradually adding only voltage magnitude constraint and λ for this is λ_2^*, iii) then both voltage magnitude and active power generation constraints were considered in (5.2) to solve for λ_3^* and iv) finally system in (5.2) was solved with all the feasibility constraints considered in this thesis (except line thermal limits) and λ in this case is described by λ_4^*. Constraints were added gradually, and different λ's were calculated to understand how the algorithm performs and to examine how the inclusion of feasibility impact the calculated transfer capability margin in general.

- Case 1: Here, transfer direction was considered for the generation at bus 2, 3 and 6 and power consumption at bus number 4, 9 and 10. This case was solved for different λ's. The scenario with no constraints resulted in largest margin i.e., $\lambda_1^* = 5.211$. Whereas the margin of the network to the boundary of the feasibility set was reduced gradually with the addition of constraints one by one. The addition of only voltage limits resulted in $\lambda_2^* = 4.110$, with addition of both voltage and active power generation constraints λ_3^* was 3.502 and finally the scenario with all the feasibility constraints resulted in the lowest bound with $\lambda_4^* = 0.843$. It was observed that addition of feasibility constraints gives a more precise margin for the transfer capability problem. The convergence of the TENR algorithm is depicted in Fig.5-9 for each of the scenarios considered here. It can be seen from Fig.5-9 the algorithm remains stable with the addition of feasibility constraints.

- Case 2: To validate the observation from Case 1, a slightly different transfer di-

84
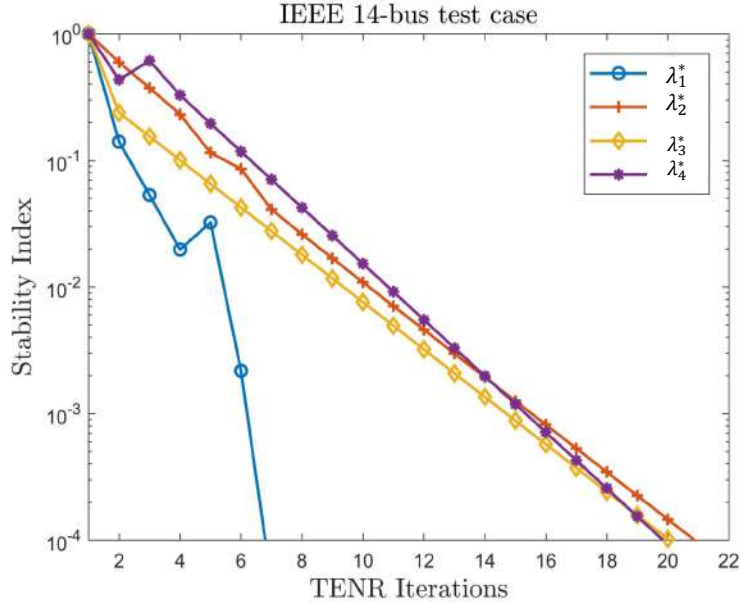
Figure 5-9: Convergence plot ieee 14 bus (Case 1)

rection was considered with generation at bus 2 and 6 while power consumption
was considered at bus 4, 9, 13 and 14. The observation in this settings were
the same as in Case 1, the highest margin was with no constraints, $\lambda_1^* = 5.320$,
then with only voltage constraints $\lambda_2^{\max} = 3.401$, with both voltage and active
power generation constraints λ_3^* was same as λ^{*2} i.e., 3.401 which means the
constraint on voltage limit violates before active power generation constraints.
While the case with all the feasibility constraint required relaxing the limit on
reactive generation at generators and λ_4^* resulted in 0.792. The convergence
plot for Case 2 is shown in Fig. 5-10 the convergence is similar to what was
observed in Case 1.

It was noticed that for each scenario or case with different combinations for λ's
the TENR algorithm remains stable and converged within fewer iterations and thus
adding constraints did not compromise the numerical stability or convergence. Results
obtained for λ_*'s of each case can be used to asses available transfer capability (ATC)
or total transfer capability (TTC). The summary of the results is given in Table.5.5.
The naive implementation of the CPF algorithm from [81] was also used to solve Case
1 and Case 2 with similar scenarios, though the results were similar but the algorithm

85
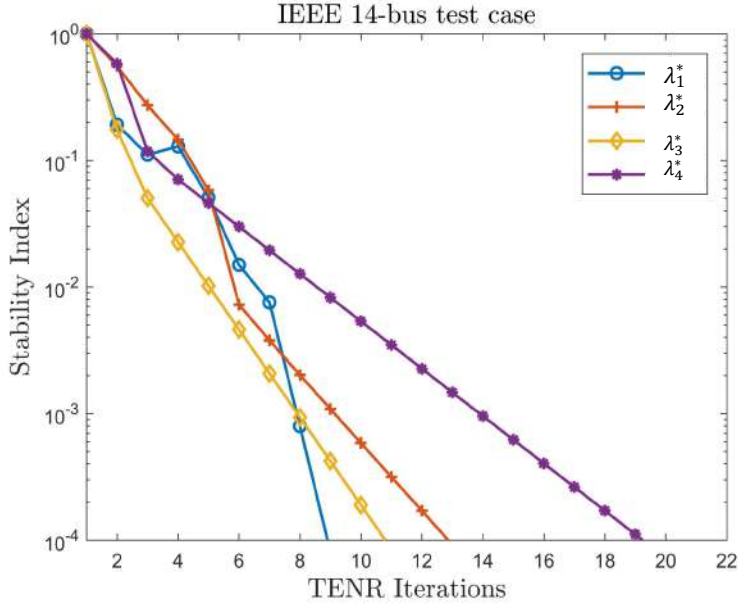
Figure 5-10: Convergence plot ieee 14 bus (Case 2)

Table 5.5: Summary of results for ieee 14-bus

Scenario	Source Buses	Sink Buses	λ_1^*	λ_2^*	λ_3^*	λ_4^*
Case 1	2, 3, 6	4, 9, 10	5.211	4.110	3.502	0.843
Case 2	2, 6	4, 9, 13, 14	5.320	3.401	3.403	0.792

suffered from a poor computational time to find a solution and required a complex implementation to detect the violation of the feasibility constraints. Whereas some other proposed approaches from literature did not give a precise bound on capability margins as lacked in the inclusion of some important constraints.

5.4   Computational Overhead

Incorporation of transversality conditions and evaluation of their sensitivities on every iteration step introduces additional computational overhead on top of the standard Newton-Raphson iterations. Specifically, the TENR algorithm attempts to solve an extended system of equations (3.3) with an extra variable λ^*. It does so by assembling an extended Jacobian matrix $\mathcal{J}$ with an additional row (i.e $\partial_x g$) and column

86

(i.e. $\partial_\lambda f$). Thus, the main computational overhead for this algorithm comes from the computation of $\partial_x g$.

The overhead is different for different choices of transversality conditions. For g_{det}, we need to compute $\partial_x g$ based on Jacobi's formula (4.30). The expensive step for this is to compute $\text{adj}(J)$ at each iteration. The computational cost for computing $\text{adj}(J)$ becomes higher as the size of the network increases. Also, this choice leads to a large number of iterations due to instability encountered in computing $\partial_x g$. At the same time, LU, QR, SVD and eigenvector transversality choices were observed to be more stable and converged in a small number of iterations for small networks. However, computing $\partial_x g$ is more expensive for the SVD, LU and eigenvector transversality choices, while the computational overhead for QR transversality choice is small. In case of SVD the most expensive step is to compute singular value decomposition of Jacobian at each Newton iteration. In our implementation the computational cost was dramatically reduced by computing SVD only for the lowest singular value using the built in MATLAB function. In case of LU the expensive step is to compute LU decomposition and also finding inverse of $\hat{L}$ and $\hat{U}$ matrices for the modified $\hat{L}D\hat{U}$ at each iteration. The higher computation overhead in case of eigenvector transversality condition is due the increase of dimension of the system variables by approximately twice.

The time required to execute this algorithm was compared with Continuation Power Flow (CPF). Several runs were performed on different IEEE cases and an average time is reported here in Table 5.6. Here t_{LU}, t_{QR}, t_{svd}, t_{eig} and t_{CPF} corresponds to time for algorithms based on g_{LU}, g_{QR}, g_{svd}, g_{eig} and CPF respectively. It can also be observed from Table 5.6 that for all the test cases the average time for g_{QR} and g_{svd} was small comparing to other choices. It is worth comparing the computational time for small and large test cases. For small test cases, LU and QR transversality choices did perform much better comparing to others as the computational cost of computing $\partial_x g$ was small. While in the case of large test networks the QR and SVD transversality choices performed better, while LU suffers from large number of iterations and the computational cost for computing $\partial_x g$ becomes higher. We ex-

pect that the SVD algorithm will likely be the most scalable for large systems, as modern implementations of partial SVD algorithm can efficiently find the few lowest singular values without the need for constructing the full decomposition. However, it is possible implementations of LU and QR algorithm, which are parallelizable, may become more effective utilizing modern manycore and GPU-based hardware architectures.Table 5.7 shows a summary of results of single iteration of TENR algorithm with different transversality choices presented in this paper. It can be observed that the SVD and QR perform better than all other choices.

From the theoretical complexity perspective, it should be noted that the LU and QR decompositions can naturally take advantage of the matrix sparsity and the low tree-width of the underlying network, and have the overall complexity that depends on the network structure, and is generally much better than the theoretical worst-case performance.

Table 5.6: Computational time for different IEEE cases (full run)

IEEE Cases	t_{LU} seconds	t_{QR} seconds	t_{svd} seconds	t_{eig} seconds	t_{CPF} seconds
14 Bus	0.004	0.004	0.022	0.023	1.165
30 Bus	0.005	0.005	0.039	0.034	4.009
118 Bus	0.042	0.042	0.058	0.101	8.389
300 Bus	0.212	0.142	0.124	0.255	3.450
2383 Bus	3.029	1.101	0.536	8.219	12.741
3120 Bus	5.091	1.651	0.798	10.713	14.364

Table 5.7: Computational time for different IEEE cases (single iteration)

IEEE Cases	t_{LU} milliseconds	t_{QR} milliseconds	t_{svd} milliseconds	t_{eig} milliseconds
14 Bus	0.3	0.4	2.4	1.5
30 Bus	0.4	0.6	3.5	2.3
118 Bus	2.1	2.6	4.1	4.6
300 Bus	7.3	6.2	8.2	10.2
2383 Bus	81.9	63.1	48.7	342.4
3120 Bus	149.4	78.6	66.5	428.5

5.5   Summary

This chapter provides an in-depth computational performance for the TENR algorithm for different choices of transversality conditions. Our numerical experiments have indicated that the algorithm compares favorably to alternatives and is characterized by a small computational overhead even in an academic implementation. It was observed that the algorithm could find a solution on the boundary of feasible with higher speed, better convergence, and scalability to large networks in comparison to traditional approaches.

Chapter 6

Calculating the Feasible Space

In this chapter, we will extend our discussion to determine the power flow feasible space. An overview of continuation methods is also provided here for tracing solution curves. In the end, an adaptive spherical continuation procedure is proposed to calculate the solution boundaries in multi-dimensional space.

6.1 Problem Formulation: Solution Boundaries

One can characterize the point of the power flow solution space boundary by following expression,

$$f_i(x, \lambda) = 0, \qquad i = 1 \dots n \tag{6.1a}$$

$$g(x) = 0. \tag{6.1b}$$

Here, $f_i(x, \lambda) \in \mathbb{R}^n$ represents a system of algebraic equations like power flows, technological constraints, together with one extra equation $g(x)$ that enforces the solution of $f_i(x, \lambda)$ on the solution space boundary. Whereas $x \in \mathbb{R}^n$ defines a vector of system variables like real and imaginary voltage set points, slack variables, while $\lambda \in \mathbb{R}^p$ describes the degree of free parameters. Following the same generalization, as we have $(n + 1)$ equations in $(n + p)$ variables, the solution boundary is a $(p - 1)$ manifold. If $p = 1$, then we have the same number of equations as variables, and thus the

solution of (6.1) is just a point on the solution manifold. The goal here is to explore the structure of solution boundary (both solvability and voltage feasibility boundary) with $p = 2$; this results in an undetermined system with $(n + 1)$ equations in $(n + 2)$ variables. Thus, the set of equations in (6.1) corresponds to a 1-manifold boundary curve. In the next section, we will have a look at the choice of transversality condition $g(x)$ based on the previous analysis.

6.1.1 Transversality condition $g(x)$

The condition that describes existence of the real solution for the set of equations in $f_i(x, \lambda)$ on the solution boundary, is referred to as "transversality condition" [56, 13]. The most natural way to enforce transversality is based on determinant as in (3.2), although this is rather simple to implement but at the same time sensitive to numerical perturbations and not scalable for the large test cases [65]. Normally, $g(x)$ is enforced by complementing the system in $f_i(x, \lambda)$ by a vector equation of the Jacobian kernel, which defines the right eigenvector corresponding to zero eigenvalue of the $\partial_x f(x, \lambda)$ as,

$$g_{\text{eig}}(x, y) = \begin{bmatrix} \partial_x f(x, \lambda)y \\ y^\top y - 1 \end{bmatrix} = 0 \tag{6.2}$$

In (6.2), y defines a non-zero right eigenvector corresponding to null space of Jacobian $\partial_x f(x, \lambda)$. Same condition can also be formulated in the form of the left eigenvector and vice versa. Enforcing $g(x)$ based on (6.2) may have the advantage to preserves the sparsity structure, but the convergence of this condition is sensitive to good initial guess of y. Also enforcing $g_{\text{eig}}(x, y)$ is not a computationally tractable choice as this results in increasing the system variables by twice.

Several possible choices of $g(x)$ are explore in chapter 4 and a detailed performance evaluation is provided in chapter 5. Thus, here we use one of the option for $g(x)$ based on singular value decomposition (SVD), due to the smaller computational burden, numerical stability, and scalability. Let us consider an $(n \times n)$ Jacobin matrix $J =$

$\partial_x f(x, \lambda)$, one can describe SVD of matrix J as,

$$J = U\Sigma V^\top = \sum_{i=1}^{n} \sigma_i u_i v_i^\top \tag{6.3}$$

In above expression, U and V are the orthogonal matrices same dimension as J. While Σ defines a diagonal matrix consisting of singular values such that $\sigma_i \geq 0, \quad i = 1, 2, \cdots, n$ [72]. As the Jacobin becomes degenerate at the boundary of power flow solution space, the minimum singular value also becomes equal to zero i.e., $\sigma_{nn} = 0$. Thus, one can enforce following necessary condition for characterizing the solution of $f_i(x, \lambda)$ on the boundary by,

$$g_{\text{svd}}(x) = u_n^\top J v_n = 0 \tag{6.4}$$

Here, u_n and v_n correspond to the nth left and right singular vectors. Although, for zero eigenvalue and singular value, the corresponding eigenvectors and singular vectors are equal. But, enforcing the transversality condition (i.e., $g(x) = 0$) through (6.4) has following benefits over (6.2), i) small computational burden as the dimension of system variables is increased only by 1, ii) does not require any guess for initialization in comparison to g_{eig}, iii) and the singular values are less sensitive to numerical perturbations. iv) And better scalability as this condition requires computing SVD only for the lowest singular value, which can be computed with an exceptionally fast speed for sparse structured matrices just like Jacobian matrix J.

Thus, we can describe the system of equations representing the points on the solution manifold as follow,

$$f_i(x, \lambda) = 0, \quad i = 1, 2, \ldots, n \tag{6.5a}$$

$$g_{\text{svd}}(x) = 0 \tag{6.5b}$$

In next section we discuss numerical methods for solving underdetermined system decribed in (6.7).

6.2 Homotopy Continuation Method

We can describe the problem for calculating the power flow solution boundary (either solvability or voltage feasibility boundary) in a compact form as,

$$h(z) = 0, \tag{6.6}$$

While,

$$h(z) = \begin{bmatrix} f_i(x, \lambda) \\ \\ g_{\text{svd}}(x) \end{bmatrix} \in \mathbb{R}^{n+1}, \quad z = \begin{bmatrix} x \\ \\ \lambda \end{bmatrix} \in \mathbb{R}^{n+2} \tag{6.7}$$

As stated earlier, the system considered in (6.6) is underdetermined with one more unknown than the equations. Thus, the solution of (6.6) will be a 1-manifold curve rather than just a point. Generally, the homotopy continuation techniques are used for tracing solution curves, with some suitable path-tracking algorithms. Such path tracking algorithms are divided into two categories; Euler homotopy approach based on the predictor-corrector algorithms [83], or Simplicial continuation based on the piecewise-linear algorithms [84]. These algorithms are robust, sophisticated, and efficient but are not widely acknowledged in practical applications due to the difficulties primarily linked to the implementation of the theory and programming [84, 85]. Here, we describe a Euler homotopy approach to trace the homotopy path of (6.6) using spherical continuation algorithm [84] with some modification to improve the robustness and speed.

6.2.1 Spherical Continuation

Normally, the Euler homotopy or predictor-corrector algorithms use tangents as predictors and hyperplanes as correctors [13]. Demerits of such approach is linked to difficult implementation, step size adjustment for convergence, and slow performance near the sharp turning points of the solution curves [84]. We describe a spherical continuation approach that uses hyperspheres or spheres as correctors instead of hy-
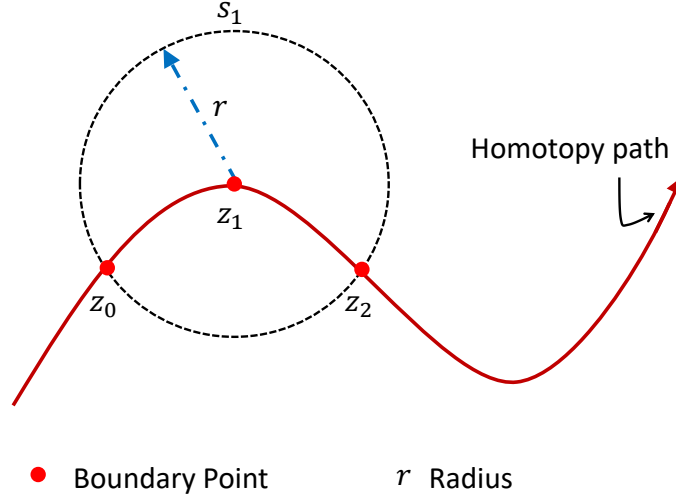
Figure 6-1: Intersection of sphere s_1 with homotopy path.

perplanes for clear geometrical interpretation, ease of implementation and fast convergence. The subsequent sections also discuss strategies to improve overall robustness and speed of the spherical continuation algorithm.

For simplification, let us consider a sphere s_1 of radius r and center z_1 is located on the homotopy path, its outline must intersect the curve at least at two points, i.e., z_2 and z_0 as shown in Fig.6-1. The formulation of a homotopy system in (6.6) has $(n+1)$ equations and $(n+2)$ variables, it means that we should include an extra equation representing a hypersphere of $(n+2)$ dimensions to trace the homotopy path by,

$$\sum_m (z_i^m - z_{i-1}^m)^2 - r^2 = 0, \tag{6.8}$$

In (6.8), the index i denotes the points on the solution boundary, while index m corresponds to the dimension of vector z. A clear graphical interpretation about the spherical continuation is illustrated in Fig.6-2. Algorithm is initiated from a starting point let z_1 that satisfy $h(z_1) = 0$ on the boundary by freeing only one parameter and then the subsequent points $z_2, z_3, ..., z_n$ on the curve are traced when second parameter

95
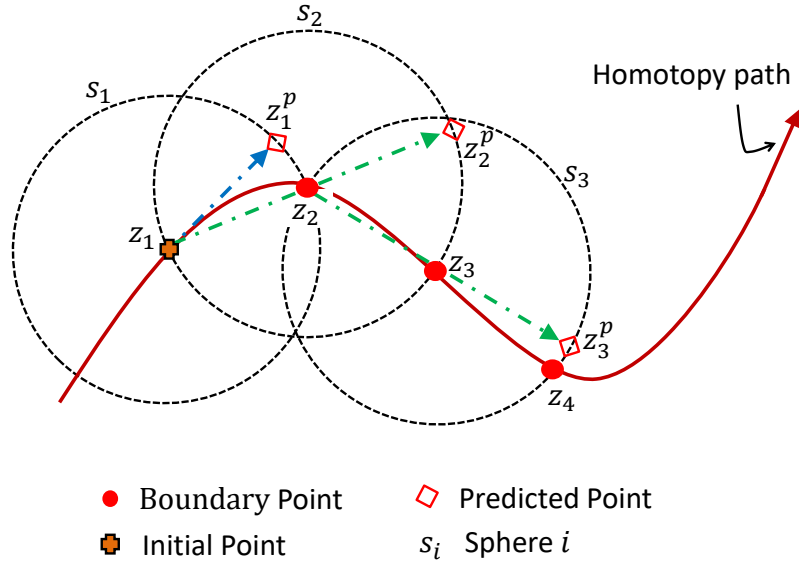
Figure 6-2: Spherical continuation, path tracking procedure.

is also free to vary, by successively solving the following system of non-linear equations at each continuation step i,

$$h(z_i) = 0 \tag{6.9a}$$

$$\sum_m (z_i^m - z_{i-1}^m)^2 - r^2 = 0, \tag{6.9b}$$

In (6.9) r is the radius of sphere. System in (6.9) can be solved using a standard technique such as Newton–Raphson. During the continuation procedure, the previous solution is used as a center of the new sphere, as depicted in Fig.6-2. This eliminates the requirement for an explicit tangent based predictor, and thus reduces the overall computational burden as the predicted point z_i^p at each continuation step can be computed by extrapolating between centers of the consecutive spheres.

Although, the spherical continuation is rather simple, computationally efficient, with ease of implementation. Still, some modifications are required to improve the robustness and computational time. At the corrector step, adjustment for the radius of sphere r is needed in case of a problem with Newton-Raphson convergence. Consequently, an adaptive sphere strategy is proposed to avoid such situations and also to

reduce the overall computational time. Also, from (6.8), it is clear that each corrector equation has at least two solutions see Fig.6-1, one in the forward and another one in the backward direction. Thus, there is a possibility that at the corrector step, Newton-Raphson can converge to a backward solution for the system in (6.9). This phenomenon is referred to as reversion phenomena. Some of the numerical examples did exhibit such behavior and were corrected by a strategies presented in [84, 86].

6.2.2   Adaptive sphere strategy

Homotopy methods are characterized by slowness to the path tracking. The radius r for spheres is fixed for the algorithm, but in order to fast track, the boundary and also the boundary with non-smooth region requires an approach with adaptive sphere sizes. The proposed approach is based on understanding the curvature of the homotopy path [85], the algorithm calculates the radius of curvature (ρ) at each continuation steps i using:

$$\rho = \left|\frac{(1 + (z_i')^2)^{\frac{3}{2}}}{z_i''}\right| \tag{6.10}$$

Here z_i' and z_i'' are first and second order derivatives, which are calculated using finite difference approximation. Then, we use the arithmetic mean for the radius of curvature as:

$$\rho_{av} = \frac{\rho_{x_1} + \rho_{x_2} + ... + \rho_{x_n} + \rho_{\lambda_1} + \rho_{\lambda_2}}{n} \tag{6.11}$$

The radius of the sphere expressed as the variable r is calculated using the hyperbolic tangent function:

$$r = \tanh(\rho_{av}) = \frac{e^{\rho_{av}} - e^{-\rho_{av}}}{e^{\rho_{av}} + e^{-\rho_{av}}} \tag{6.12}$$

It was observed that the algorithm becomes fast and also more adaptive for tracing the boundary in case of sharp turns/edges.

6.3   Implementation

The computation of a solution boundary first requires calculating an initial point on the boundary and then tracking the homotopy path using continuation procedure. Therefore, a two-stage implementation is proposed.

The first stage solves the system described by (6.6) by releasing only one free parameter, i.e., λ_1 while keeping the second free parameter, i.e., λ_2 constrained. This results in $(n+1)$ equations in $(n+1)$ unknowns, thus solution of (6.6) is just a point on the boundary. Standard Newton-Raphson iterations are used to solve such a system. As the system in (6.6) consists of non-linear algebraic equations, this means multiple roots exists for solution of (6.6). Each of these roots corresponds to a different solution branch. Relaxed Newton iterations are used to determine multiple roots, to use as an initial point for tracing various branches.

In the second stage, the second free parameter λ_2 is also free to vary; this results in the underdetermined system with $(n+1)$ equations in $(n+2)$ variables. Thus, the solution of (6.6) is a 1-manifold curve; such curves are traced by the proposed spherical continuation that uses the initial point from the first stage to trace the corresponding branch.

6.4   Summary

Here, we present a mathematical framework to calculate the solution boundaries, details of different contributions within this context is also provided here. In the end, an adaptive spherical correction algorithm is proposed to trace the solution manifold with ease of programming and computational tractability.

Chapter 7

Numerical Studies II: Calculating the Feasible Space

This chapter presents the numerical studies related to solvability and feasibility boundaries in higher dimensions. The discussion here also covers the structure of the feasibility manifold for a verity of test cases. Detailed performance of the proposed continuation algorithm is also provided.

7.1 Three Bus System

First, a small three bus network is given similar to one in [13]. Even though, it is a small test case, it illustrates the complexity of the power flow feasible space. Figure.7-1 shows the three bus network with the following settings. Bus 1 as slack bus with voltage phasor $\hat{V}_1 = 1.0\angle 0°$. Bus 2 as PV bus with voltage set point $\hat{V}_2 = 1.0\angle\delta_2$, while active and reactive power injections are P_2^{inj} and Q_2^{inj} respectively. Whereas the real and reactive power injections at bus 3 are represented by P_3^{inj} and Q_3^{inj}, with complex voltage phasor denoted as $\hat{V}_3 = V_3\angle\delta_3$. Also, all the line in the network are lossless with inductance set to $X_{12} = X_{13} = X_{23} = 1.0$ p.u. Based on the network settings, there is only one PQ and and one PV bus. Thus, the solution manifold is confined in $P_2^{\text{inj}} - P_{inj}^2 - Q_3^{\text{inj}}$ space. Two scenarios conceived here are as follow,

- First, the solution manifold in constructed in the the space of $P_2^{\text{inj}} - P_3^{\text{inj}} - Q_3^{\text{inj}}$
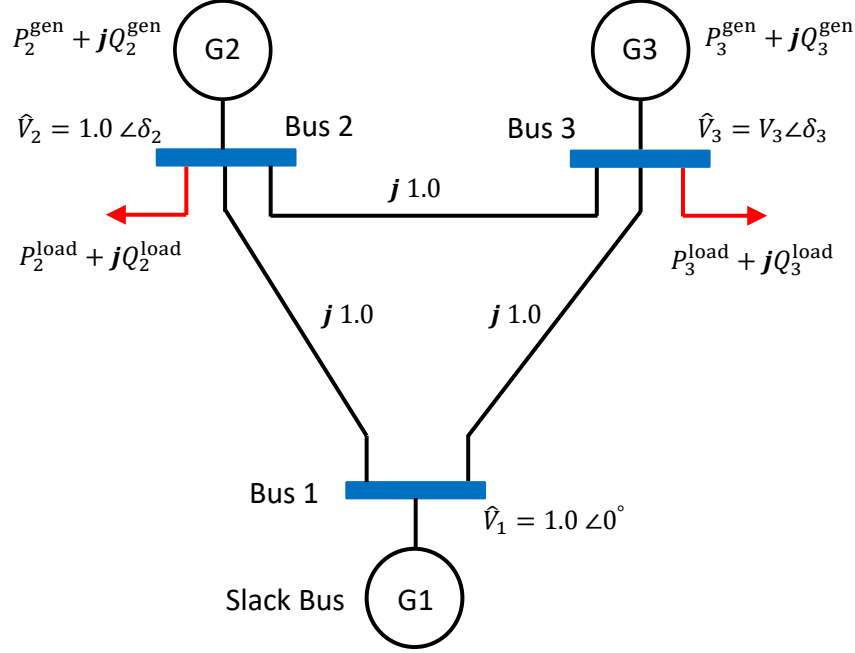
Figure 7-1: Three bus network.

without enforcing any technological constraints.

- In the later case, solution manifold is constructed in $P_2^{\mathrm{inj}} - P_3^{\mathrm{inj}} - Q_3^{\mathrm{inj}}$ by enforcing voltage constraint on bus 3.

7.1.1 Solvability manifold

Figure.7-2 shows the slice of the solution space in $P_2^{\mathrm{inj}} \ P_3^{\mathrm{inj}}$ plane with $Q_3^{\mathrm{inj}} = 0.2$ p.u. Solvability boundary curves are depicted in Fig.7-2, as no technological constrained are introduced yet. We can see three distinct boundaries $\boldsymbol{\gamma}^1$, $\boldsymbol{\gamma}^2$, and $\boldsymbol{\gamma}^3$, at each of these boundaries system in (6.6) is valid. Since the system of equations in $f_i(x, \lambda)$ are non-linear; therefore, multiple solution boundaries exist. For a given starting point in $P_2^{\mathrm{inj}} \ P_3^{\mathrm{inj}}$ plane, the algorithm first tries to find a starting point for each of these curves, and then the proposed continuation is initiated to trace all these curves. It is also worth mentioning that $\boldsymbol{\gamma}^1$ is the outer boundary, as no real solution to power flows exist beyond this curve. While $\boldsymbol{\gamma}^2$ and $\boldsymbol{\gamma}^3$ are the inner folds in the solution space sometimes referred to as inner boundaries. In comparison to the outer
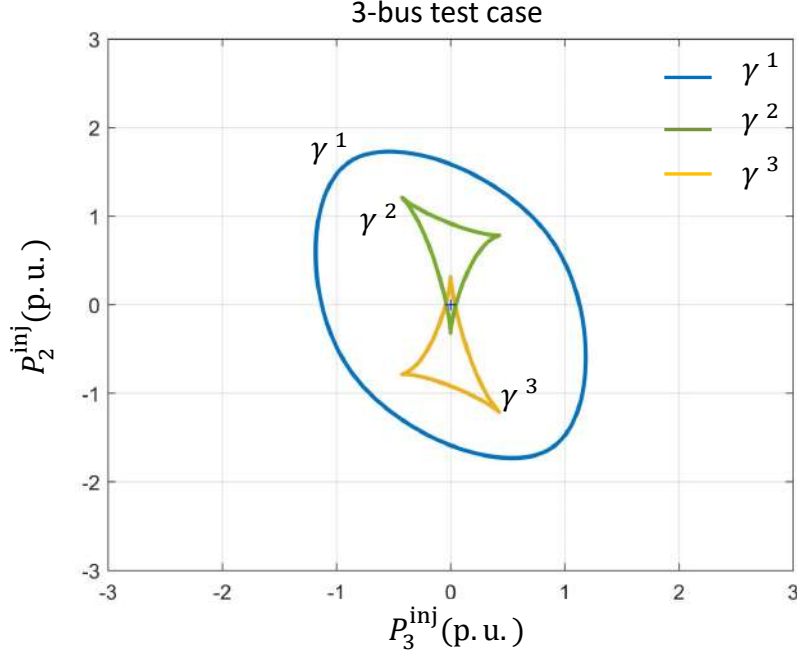
Figure 7-2: Solvability boundaries in P_2^{inj} P_3^{inj}, with $Q_3^{\text{inj}} = 0.2$ p.u.

boundary curve $\boldsymbol{\gamma}^1$, the solution curves $\boldsymbol{\gamma}^2$ and $\boldsymbol{\gamma}^3$ corresponds to low voltage levels for bus 3. Therefore, it was concluded that the inner boundaries correspond to a low voltage branch of the solution manifold [13]. A complete solvability space is provided in Fig.7-3, each boundary curve is drawn in $P_2^{\text{inj}} - P_3^{\text{inj}}$ plane as contours of Q_3^{inj}. For simplicity, the inner boundaries corresponding to each slice in Fig.7-3 are not shown here. From Fig.7-3, it is also clear that the solvability is an open space with no maximum bound on Q_3^{inj}, while the minimum bound on $Q_3^{\text{inj}} = -0.5$ p.u.

7.1.2 Feasibility manifold

In this case, a feasible space is explored in $P_2^{\text{inj}} - P_3^{\text{inj}} - Q_3^{\text{inj}}$ with constraint on voltage level at bus 3 such that $0.9 \leq |V_3| \leq 1.1$ p.u. This eliminates the chances for the algorithm to compute boundaries where inequality on V_3 is violated. Following analysis is performed,

- First, the solution manifold in constructed in the space of P_2^{inj} and P_3^{inj} by constructing boundary curves in $P_2^{\text{inj}} - P_3^{\text{inj}}$ plane as contours of Q_3^{inj}.

101
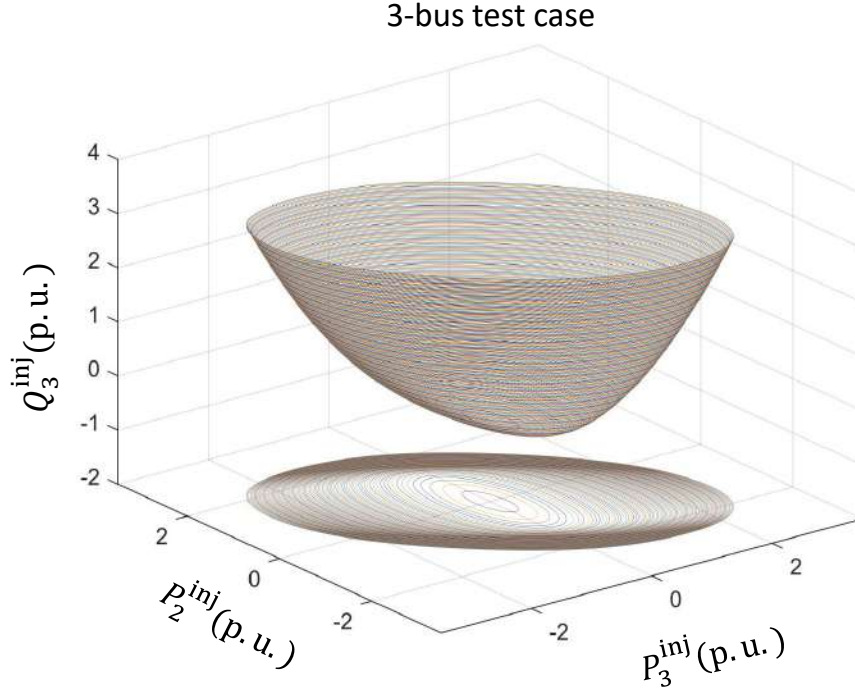
Figure 7-3: Power flow solvability space in $P_2^{inj} - P_3^{inj} - Q_3^{inj}$. Also, projection of the solvability manifold is provided in $P_2^{inj} - P_3^{inj}$ as contours of Q_3^{inj}.

- In the later case, solution manifold is constructed in P_2^{inj} and Q_3^{inj} by constructing boundary curves in $P_2^{\text{inj}} - Q_3^{\text{inj}}$ plane as contours of P_3^{inj}.

- Finally a connection between these two cases will be examined.

7.1.2.0.1 Projection in $P_2^{\text{inj}} - P_3^{\text{inj}}$

Figure.7-4 shows a slice of the feasible space in $P_2^{\text{inj}} - P_3^{\text{inj}}$ plane with $Q_3^{\text{inj}} = 0.2$ p.u. The voltage feasibility boundary within this slice is depicted by curve $\boldsymbol{\beta}$. From the Fig.7-4, it is noticeable the area enclosed by curve $\boldsymbol{\beta}$ is smaller than the $\boldsymbol{\gamma}^1$ as voltage level is constrained on bus 3. The projection of the feasibility manifold in P_2^{inj} and P_3^{inj} is given in Fig.7-5. Each curve in Fig.7-5 corresponds to a distinct value of Q_3^{inj}. From this projection, it is also observable that solution space is clearly bounded with some folding as well.
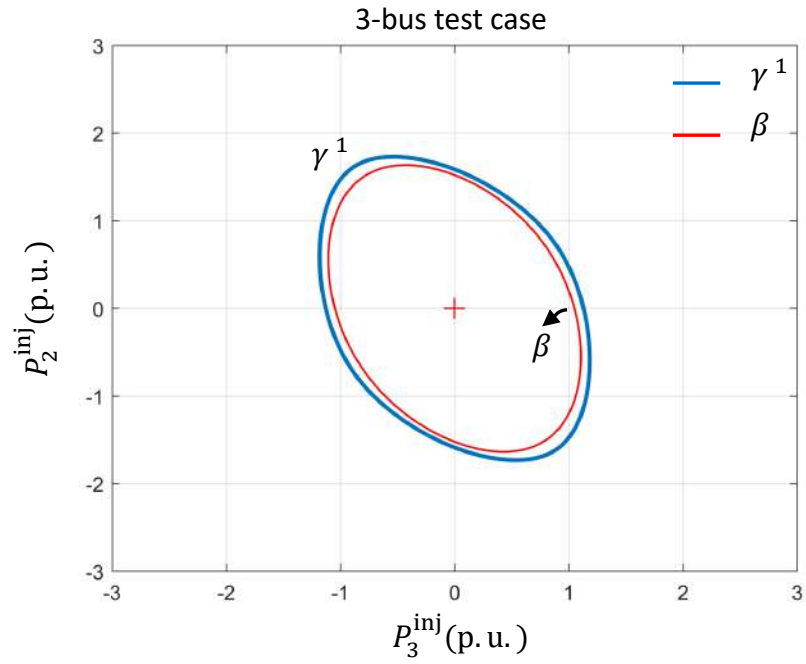
Figure 7-4: Feasibility boundary in P_2^{inj} P_3^{inj}, with $Q_3^{\text{inj}} = 0.2$ p.u
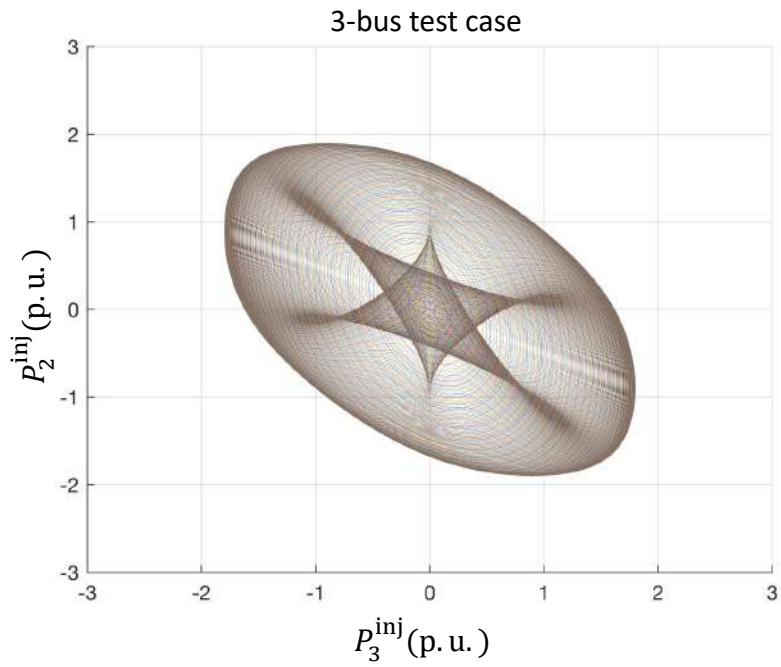
Figure 7-5: Projection of feasible space in P_2^{inj} P_3^{inj} as contours of Q_3^{inj}.
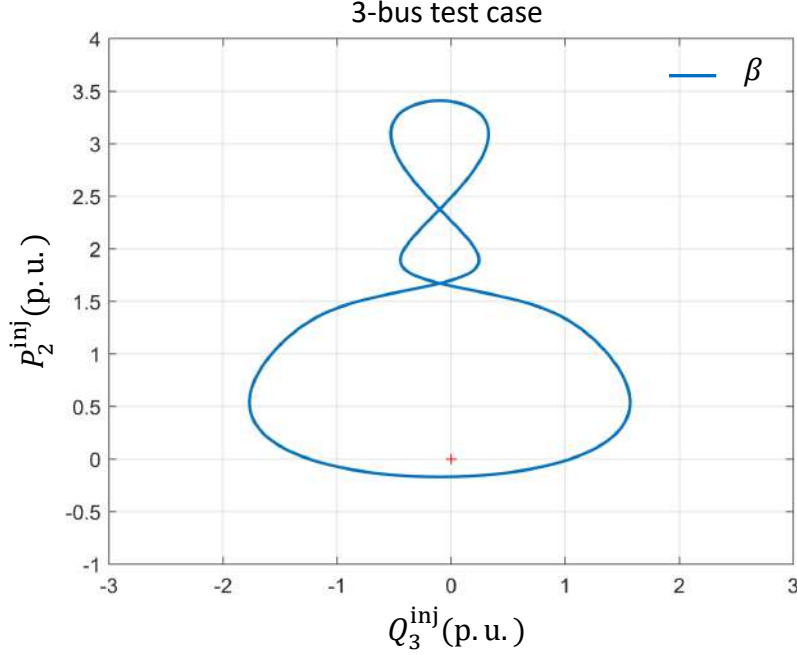
Figure 7-6: Feasibility boundary in P_2^{inj} Q_3^{inj}, with $P_3^{\text{inj}} = 0.2$ p.u

7.1.2.0.2   Projection in $P_2^{\text{inj}} - Q_3^{\text{inj}}$

In this case, a slice of feasible space is drawn in $P_2^{\text{inj}} - Q_3^{\text{inj}}$ plane with $P_3^{\text{inj}} = 0.2$ p.u. In Fig.7-6, boundary curve $\boldsymbol{\beta}$ shows the slice within this framework. The $\boldsymbol{\beta}$ curve is non-convex and it is also folded. The projection of the feasibility manifold in P_2^{inj} and P_3^{inj} is given in Fig.7-7. Each curve in Fig.7-7 corresponds to a distinct value of P_3^{inj}, folding in the power flow feasible space is also evident from this figure.

7.1.2.0.3   Connection between $P_2^{inj} - P_3^{inj}$ and $P_2^{inj} - Q_3^{inj}$ spaces

The projections of the power flow feasible space given by Figs.7-5 and 7-7 can be combined to show the solution space in the three dimensional $P_2^{inj} - P_3^{inj} - P_3^{inj}$ space. Fig. 7-8 shows this surface, together with its $P_2^{inj} - P_3^{inj}$ and $P_2^{inj} - Q_3^{inj}$ projections. Although the 3-bus system is small, the complexity of the problem is easier to see. In next example will consider a five bus network and will also explore examples of voltage feasibility boundaries.
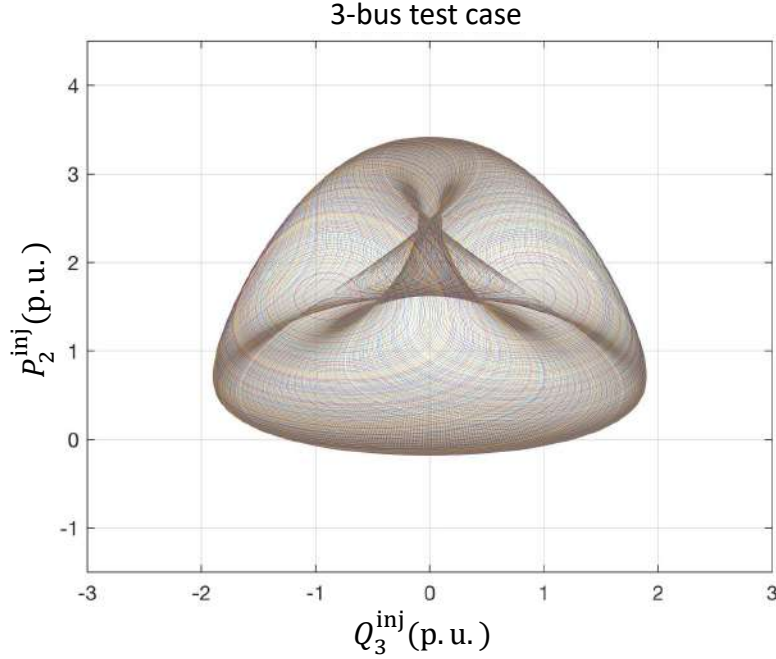
Figure 7-7: Projection of feasible space in P_2^{inj} Q_3^{inj} as contours of P_3^{inj}.

7.2 Five Bus System

In this section a five bus example is provided, as illustrated in Fig.7-9. Bus 1 is the slack bus. While all other buses in the network are PV buses, except bus 3 which is a PQ bus with voltage set point $|V_3|\angle\delta_3$. On PV bus 4 and 5, voltage magnitudes are constrained to 1.05 p.u. The characteristics of the lines are specified in Fig.7-9. The bus 2 and 3 have non-zero active power injections, while the bus 4 and 5 are synchronous condensers with zero active power injections. Based on the network settings, there is only one PQ and and one PV bus with non-zero power injections. Thus, the solution manifold is confined in $P_2^{\text{inj}} - P_{inj}^2 - Q_3^{\text{inj}}$ space.

- First, the solution manifold in constructed in the the space of $P_2^{\text{inj}} - P_3^{\text{inj}} - Q_3^{\text{inj}}$ without enforcing any technological constraints.

- In the later case, solution manifold is constructed in $P_2^{\text{inj}} - P_3^{\text{inj}} - Q_3^{\text{inj}}$ by enforcing voltage constraint on bus 3.

105
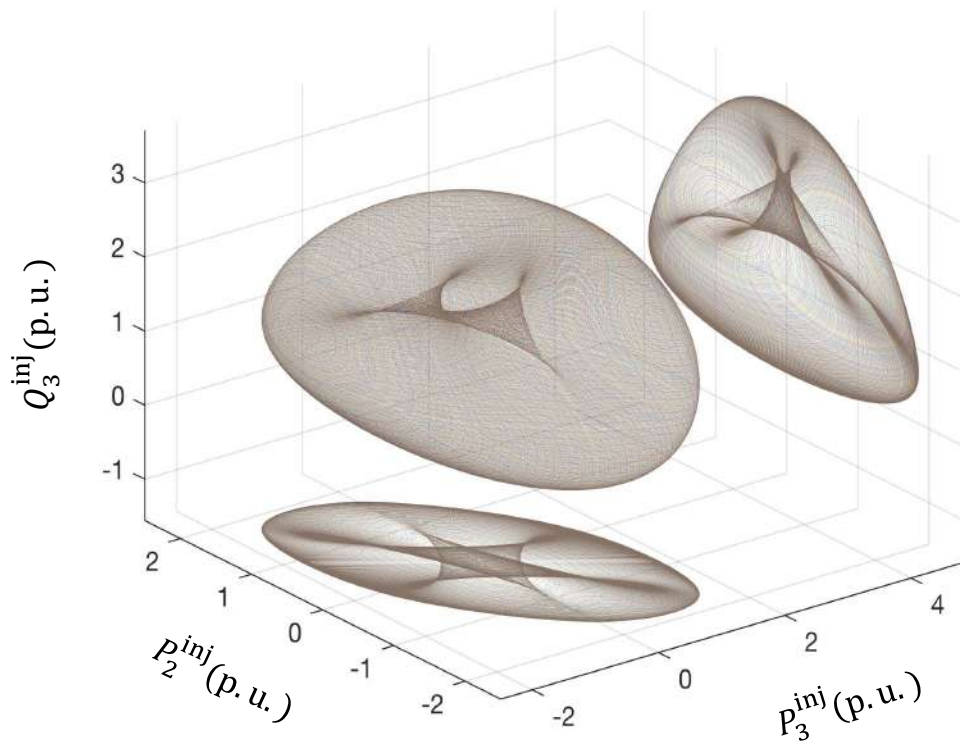
Figure 7-8: Power flow feasible space for a 3-bus network. Here P_2^{inj}, P_3^{inj} represents active power injection at bus 2 and 3. While Q_3^{inj} is the reactive power injection at bus 3. Also, projection of the feasible manifold is provided in $P_2^{inj} - P_3^{inj}$ as contours of Q_3^{inj}. Another projection of the feasible manifold is in $P_2^{inj} - Q_3^{inj}$ space as contours of P_3^{inj}
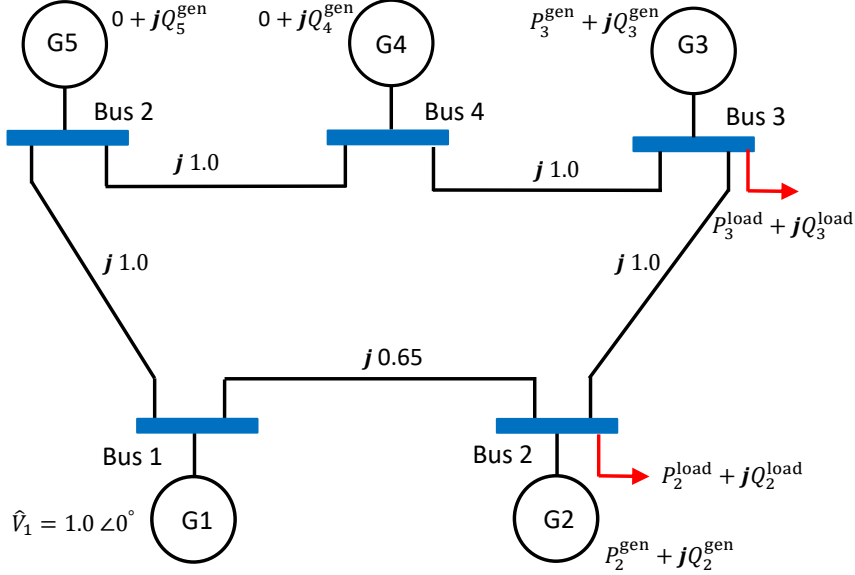
Figure 7-9: Five bus test system.

7.2.1 Solvability manifold

Similar to 3-bus test case, first scenario considers a solvability manifold in $P_2^{\text{inj}} - P_3^{\text{inj}}$-$Q_3^{\text{inj}}$ space (no constraints are included). Figure.7-10 shows the three distinct boundaries highlighted as $\boldsymbol{\gamma}^1$, $\boldsymbol{\gamma}^2$ and $\boldsymbol{\gamma}^3$. At each of these boundaries the solution to system in $f_i(x, \lambda)$ exist with the condition that gradient $\partial_x f(x, \lambda)$ is also singular. The $\boldsymbol{\gamma}^1$ curve is the outer boundary, as any operating point outside $\boldsymbol{\gamma}^1$ is unsolvable. Whereas the $\boldsymbol{\gamma}^2$ and $\boldsymbol{\gamma}^3$ curves are inner boundaries with low voltage solutions, such curves divide the solution space into regions where different numbers of equilibria exist [13, 87]. Figure.7-11 provides a complete description about about solvability space in $P_2^{\text{inj}} - P_3^{\text{inj}} - Q_3^{\text{inj}}$. The solvability manifold is an open space with no maximum bound on Q_3^{inj}, while the minimum bound on $Q_3^{\text{inj}} = -0.5$ p.u.

7.2.2 Feasibility manifold

Here, a feasibility space is explored in $P_2^{\text{inj}} - P_3^{\text{inj}} - Q_3^{\text{inj}}$ with constraint on voltage level at bus 3 such that $0.9 \leq V_3 \leq 1.1$ p.u. A similar analysis was performed here as follow,

- First, the solution manifold in constructed in the space of P_2^{inj} and P_3^{inj} by
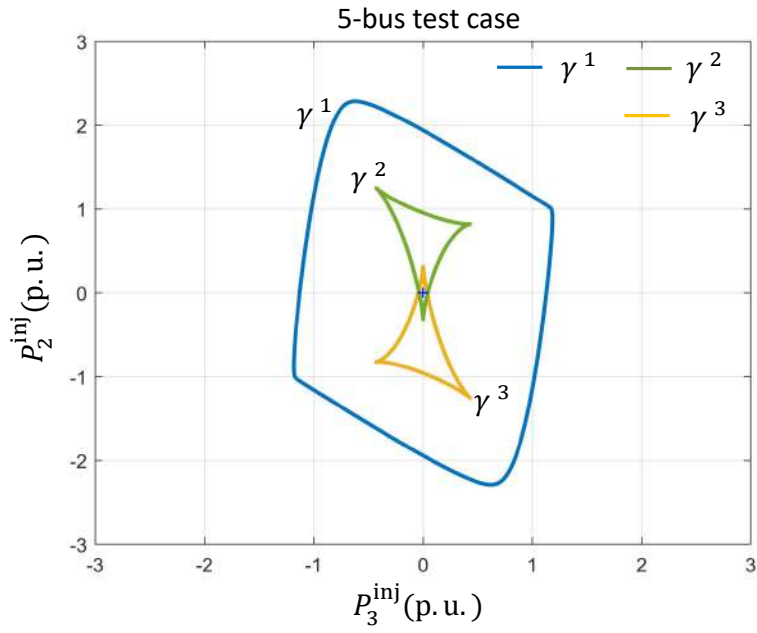
Figure 7-10: Solvability boundaries in P_2^{inj} P_3^{inj}, with $Q_3^{\text{inj}} = 0.2$ p.u.
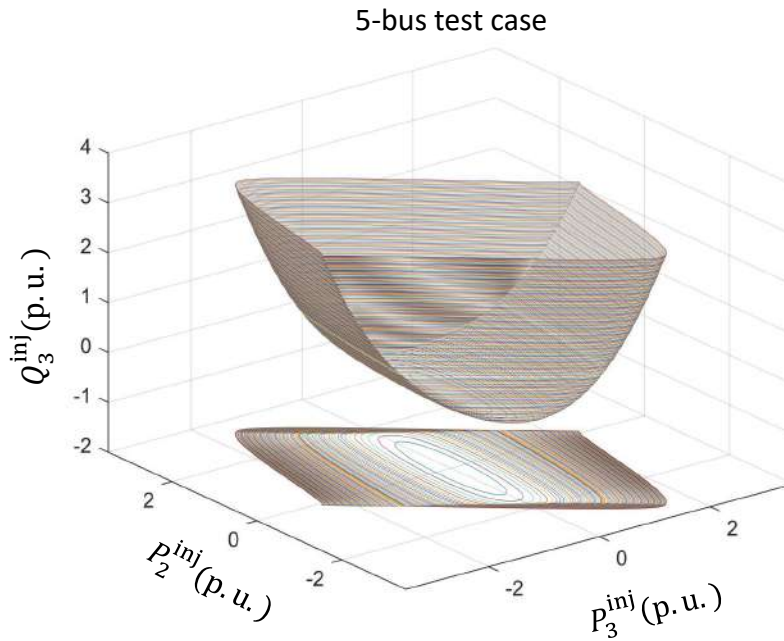
Figure 7-11: Power flow solvability space in $P_2^{inj} - P_3^{inj} - Q_3^{inj}$. Also, projection of the solvability manifold is provided in $P_2^{inj} - P_3^{inj}$ as contours of Q_3^{inj}.
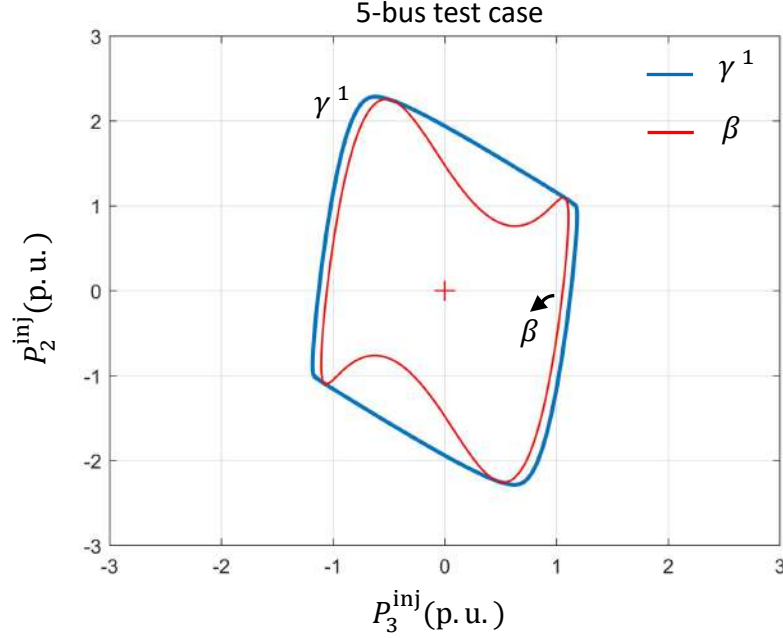
Figure 7-12: Feasibility boundary in P_2^{inj} P_3^{inj}, with $Q_3^{\text{inj}} = 0.2$ p.u.

constructing boundary curves in $P_2^{\text{inj}} - P_3^{\text{inj}}$ plane as contours of Q_3^{inj}.

- In the later case, solution manifold is constructed in P_2^{inj} and Q_3^{inj} by constructing boundary curves in $P_2^{\text{inj}} - Q_3^{\text{inj}}$ plane as contours of p_3^{inj}.

- Finally a connection between these spaces will be analyzed.

7.2.2.0.1 Projection in $P_2^{\text{inj}} - P_3^{\text{inj}}$

A slice of feasibility space is constructed in $P_2^{\text{inj}} - P_3^{\text{inj}}$ plane with $Q_3^{\text{inj}} = 0.2$ p.u. The corresponding feasibility slice is shown by voltage feasibility boundary curve $\boldsymbol{\beta}$ (see Fig.7-12). It is evident from the Fig.7-12, the boundary curve $\boldsymbol{\beta}$ is non-convex and region enclosed by $\boldsymbol{\beta}$ is smaller than the solvability boundary curve γ^1. The projection of the feasibility manifold in $P_2^{\text{inj}} - P_3^{\text{inj}}$ space is constructed by drawing boundary boundary curve in $P_2^{\text{inj}} - P_3^{\text{inj}}$ plane as contours of Q_3^{inj}, as shown in Fig.7-13.

7.2.2.0.2 Projection in $P_2^{\text{inj}} - Q_3^{\text{inj}}$

A slice of feasibility manifold is also drawn in $P_2^{\text{inj}} - Q_3^{\text{inj}}$ plane with $P_3^{\text{inj}} = 0.2$ p.u. From Fig.7-14, it is clear that the boundary curve $\boldsymbol{\beta}$ within this slice is non-
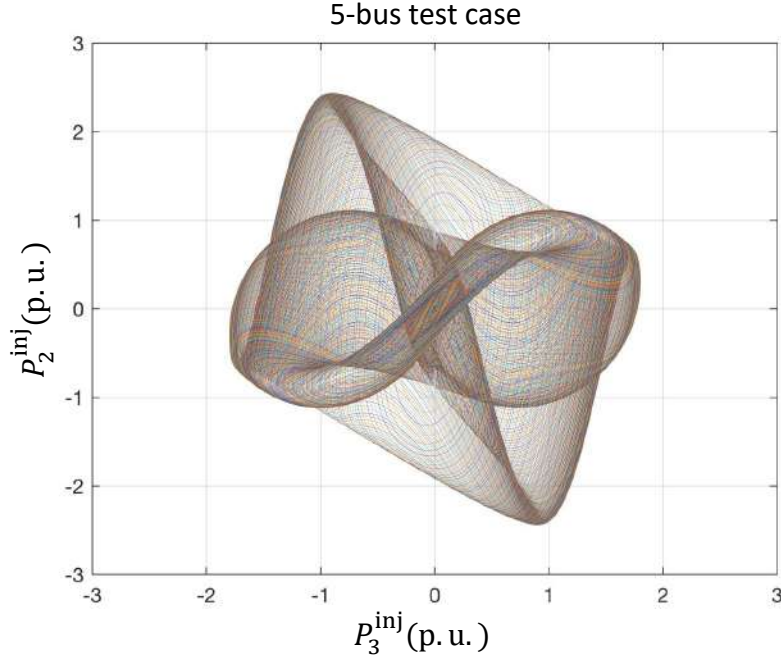
Figure 7-13: Projection of feasible space in P_2^{inj} P_3^{inj} as contours of Q_3^{inj}.

convex and it is also provide an indication about folding in the feasible space. The projection of the feasibility space in P_2^{inj} and P_3^{inj} is given Fig.7-15. Each curve in Fig.7-15 corresponds to a distinct value of P_3^{inj}.

7.2.2.0.3 Connection between $P_2^{\text{inj}} - P_3^{\text{inj}}$ and $P_2^{\text{inj}} - Q_3^{\text{inj}}$ spaces

Finally, fig.7-16 shows the complete feasibility surface in $P_2^{\text{inj}} - P_3^{\text{inj}} - P_2^{\text{inj}}$, which was constructed by combining the power flow feasible space given by Figs.7-13 and 7-15 together with its $P_2^{inj} - P_3^{inj}$ and $P_2^{inj} - Q_3^{inj}$ projections. Although the settings considered in this network in terms of power injections were similar to a 3-bus system, this resulted in a more complex geometry of the feasibility space. As the network topology also influences the shape and complexity of the feasibility manifold.

Both 3-bus and 5-bus networks show that feasibility space is quite complicated, and also challenging to compute. The proposed spherical continuation with the adaptive sphere strategy worked great to construct the results presented above.

110
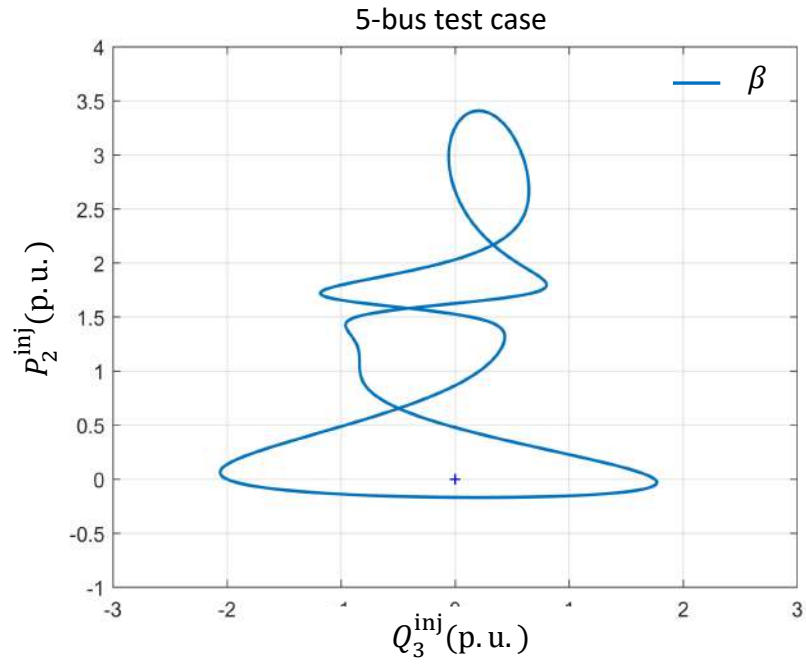
Figure 7-14: Feasibility boundary in P_2^{inj} Q_3^{inj}, with $P_3^{\text{inj}} = 0.2$ p.u.
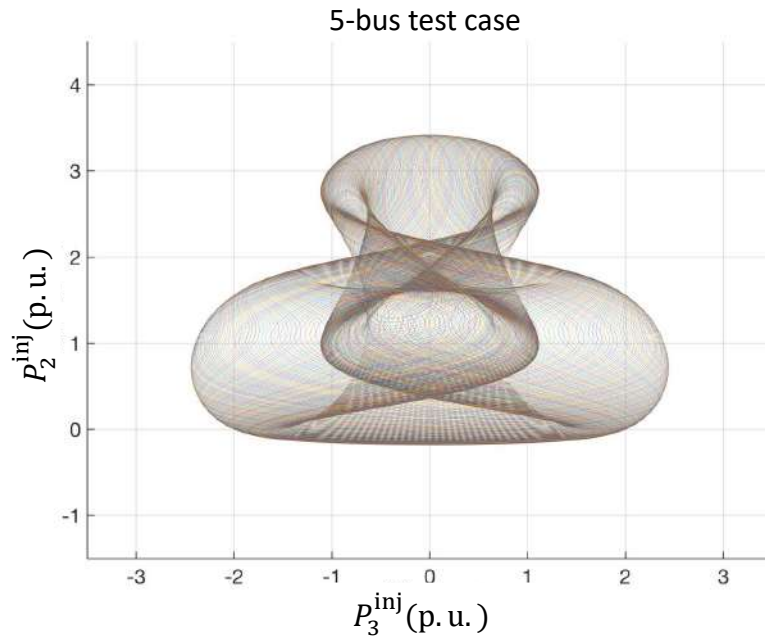
Figure 7-15: Projection of feasible space in P_2^{inj} Q_3^{inj} as contours of P_3^{inj}.

5-bus test case
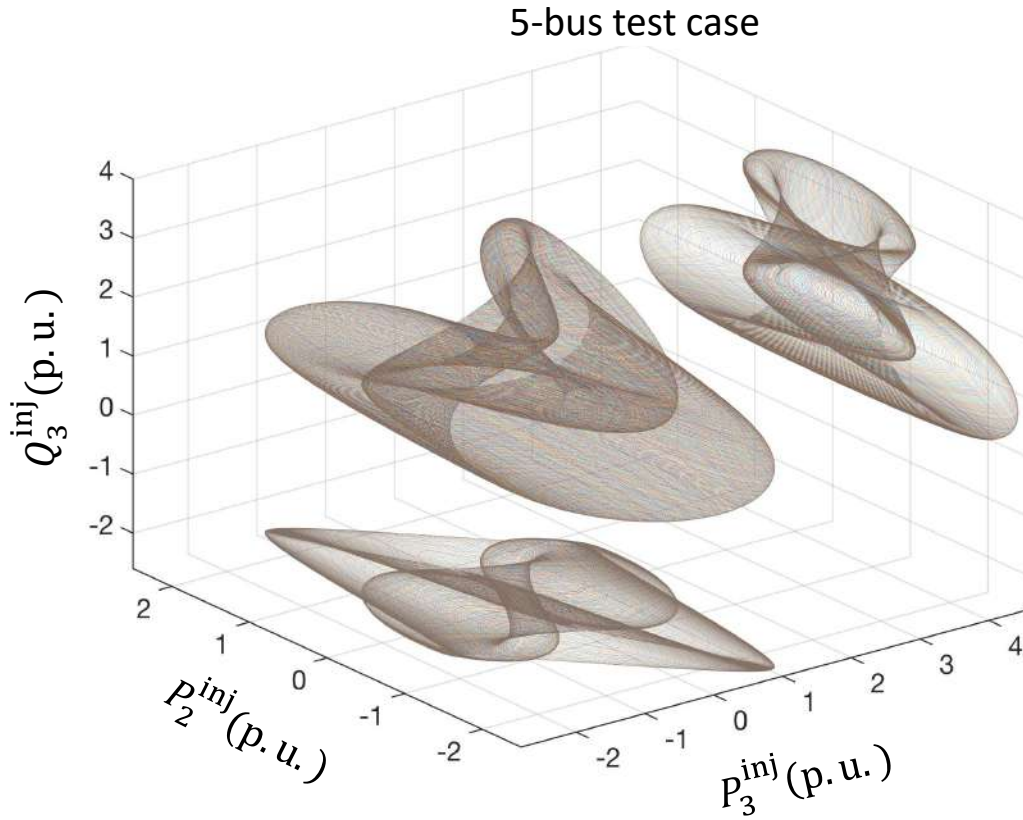
Figure 7-16: Power flow feasible space for a 5-bus network. Here P_2^{inj}, P_3^{inj} represents active power injection at bus 2 and 3. While Q_3^{inj} is the reactive power injection at bus 3. Also, projection of the feasible manifold is provided in $P_2^{inj} - P_3^{inj}$ as contours of Q_3^{inj}. Another projection of the feasible manifold is in $P_2^{inj} - Q_3^{inj}$ space as contours of P_3^{inj}

7.3 IEEE Cases

This section covers plenty of examples for different IEEE test networks, to evaluate the computational performance of the proposed spherical continuation procedure. For simplicity, we will consider only a two dimensional slice of the solution manifold.

7.3.1 IEEE 9-bus test case

First example presents an IEEE 9-bus test case [75], with bus 1 as slack bus. While rest of the buses in the network are PQ buses, except bus number 2 and 3 which are PV buses.

7.3.1.0.1 Solvability space

Here, a solvability manifold is considered in the space of P_2^{inj} (active power injections at bus 2), P_5^{inj} (active power injection at bus 5) and Q_5^{inj} (reactive power injection at bus 5). This means power injections at all the other buses are constrained. The Fig.7-17 shows the 2-dimensional slice of the feasibility space in $P_2^{\text{inj}} - P_5^{\text{inj}}$ plane with $Q_5^{\text{inj}} = 0$ p.u. The outer boundary is outlined as $\boldsymbol{\gamma}^1$, while the inner folds are highlighted by $\boldsymbol{\gamma}^2$ and $\boldsymbol{\gamma}^3$. Some of the points on the inner boundaries $\boldsymbol{\gamma}^2$ and $\boldsymbol{\beta}^3$ had voltage magnitudes on PQ buses as low as 0 p.u., thus such curves represents low voltage branches of the solution space.

7.3.1.0.2 Feasibility space

In Fig.7-18, a feasibility boundary $\boldsymbol{\beta}$ is also shown such that all the buses $i \in \mathcal{L}$ also satisfy voltage magnitude limits defined by $0.9 \le |V_i| \le 1.1$ p.u. Here $\mathcal{L}$ represents the set of PQ buses in the network. It is noticeable that the feasibility curve within this 2-dimensional slice enclosed a small convex region. Figure.7-18 also highlights a point "A"; at this point, the conventional spherical continuation algorithm experienced the reversion phenomenon, which was avoided by the strategy proposed in the previous chapter.
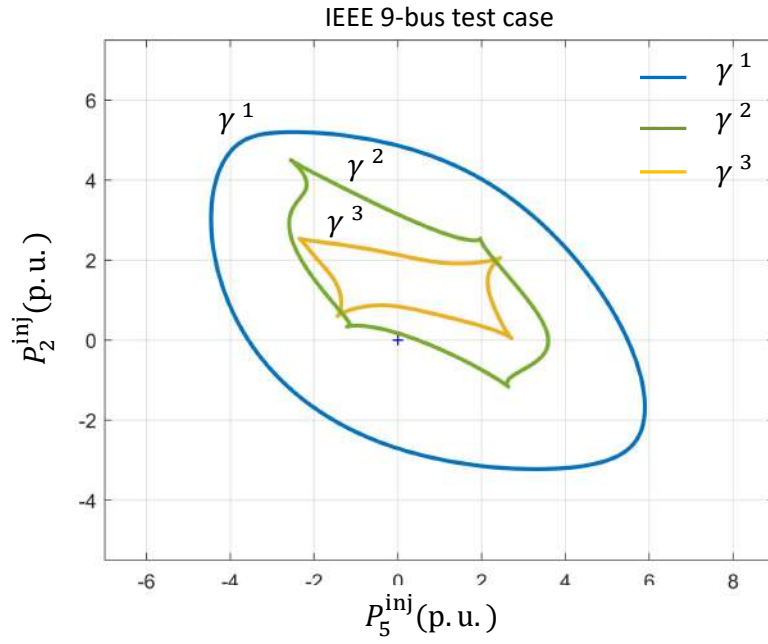
Figure 7-17: Solvability boundaries in P_2^{inj} P_5^{inj}, with $Q_5^{\mathrm{inj}} = 0$ p.u.
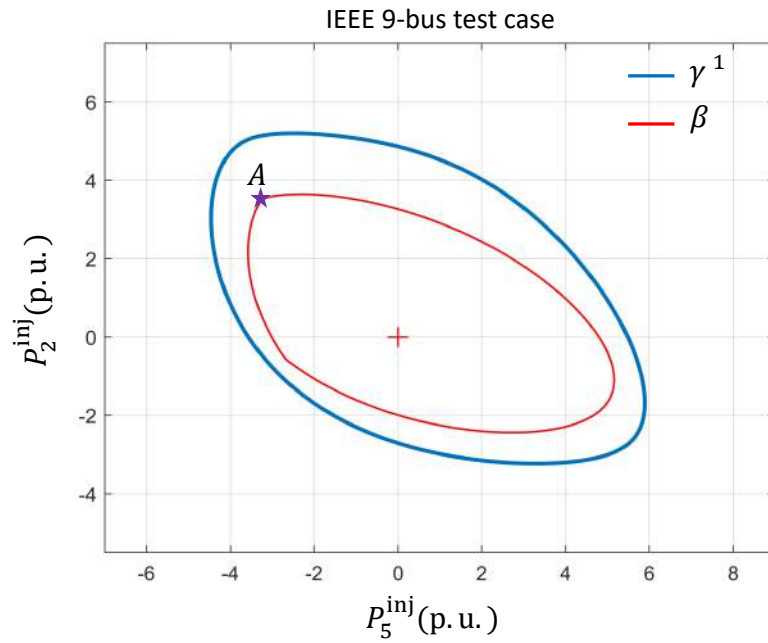
Figure 7-18: Voltage feasibility boundaries in P_2^{inj} P_5^{inj}, with $Q_5^{\mathrm{inj}} = 0$ p.u.
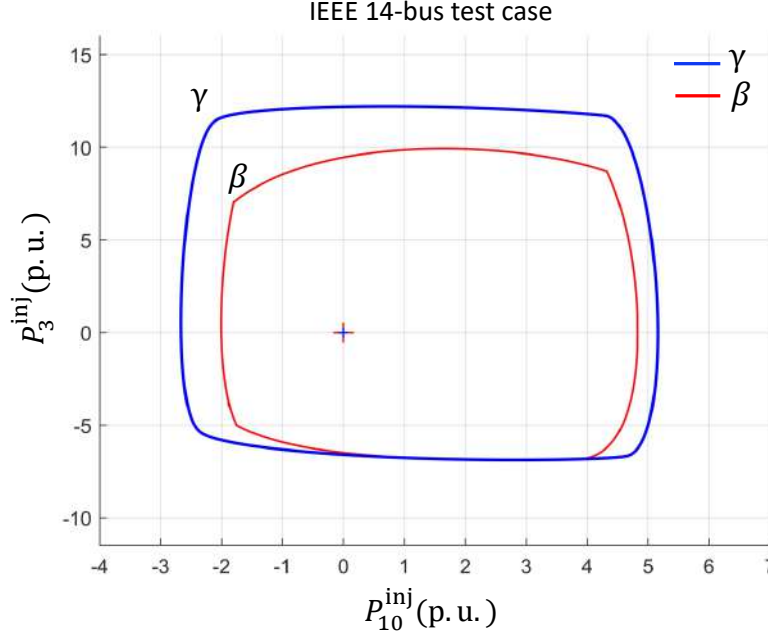
Figure 7-19: Solvability and voltage feasibility boundary in P_2^{inj} P_{10}^{inj} space, with $Q_{10}^{\text{inj}} = 0$ p.u.

7.3.2 IEEE 14-bus test network

A similar analysis is performed on an IEEE 14-bus network from [75]. All the buses are PQ or load buses in this network, except buses 2, 3, 6, and 8, which represent PV buses. A 2-dimensional slice of the solvability and feasibility space is provided in P_3^{inj} (active power injection at bus 3), P_{10}^{inj} (active power injection at bus 10) and Q_{10}^{inj} (reactive power injection at bus 10) space.

Figure.7-19 shows an outer boundary $\boldsymbol{\gamma}$ and voltage feasibility boundary $\boldsymbol{\beta}$ in space of $P_3^{\text{inj}} - P_{10}^{\text{inj}}$ plane with $Q_{10}^{\text{inj}} = 0$ p.u. Although, inner boundaries exist but are presented here for ease of illustration. The boundary curve $\boldsymbol{\gamma}$ separates the unsolvable region where the solution to power flows disappears. While boundary curve $\boldsymbol{\beta}$ encompass an area where at each bus $i \in \mathcal{L}$ satisfy the following constraint on voltage levels,

$$0.9 \leq |V_i| \leq 1.1 \text{ p.u} \tag{7.1}$$

Here $\mathcal{L}$ represents the set of PQ buses in the network.

7.3.3 IEEE 300-bus test network

A test on an IEEE-300 bus network is given, to access the scalability of the proposed continuation. There are 68 PV buses and 231 PQ buses in the network. Larger systems are more prone to numerical instabilities as a large number of equations are required to be solved, due to the size of the network.

The solvability boundary γ and voltage feasibility boundary β is drawn in the space of P_8^{inj} (active power injection at bus 8), P_{14}^{inj} (active power injection at bus 9) and Q_{14}^{inj} (reactive power injection at bus 9). Figure.7-20 shows the 2-dimensional slice of the solvable and feasible space in the plane of P_8^{inj} P_{14}^{inj} with $Q_{14}^{\text{inj}} = 0$ p.u. All the operating points in the feasible region (enclosed by curve β) satisfy the constraints on voltage magnitudes,

$$0.9 \leq |V_i| \leq 1.1 \text{ p.u} \tag{7.2}$$

Here $\mathcal{L}$ represents the set of PQ buses in the network. While the infeasible region is described by the area enclosed by curve γ. From the computational context, the proposed continuation with the adaptive sphere strategy worked well with an average time of 3.7 seconds, while the hyperplanes continuation 35.3 seconds.

7.3.4 Russian United Energy System

This section provides a test network from Russian Far-East, which is situated on the outskirts of the Russian power grid. From one side, it operates in synchronization with the Russian United Energy System (RUES), while the other side it is connected with the northern part of the Chinese System (CES) by a 220 kV transmission lines. Generally, the whole Far-East network is spanned over four regional parts, such as Amurskaya, Primorskaya, Khabarovskaya, and Yakutskaya.

Network topology for Primorskaya Energy System (PES) is shown in Fig. 7-21. The test system consists of 64 buses in total, with 11 generator buses and 40 load buses. It is the most prominent area in terms of the future developments of the Far-East territory. Within the next ten to twenty years, rapid growth is projected
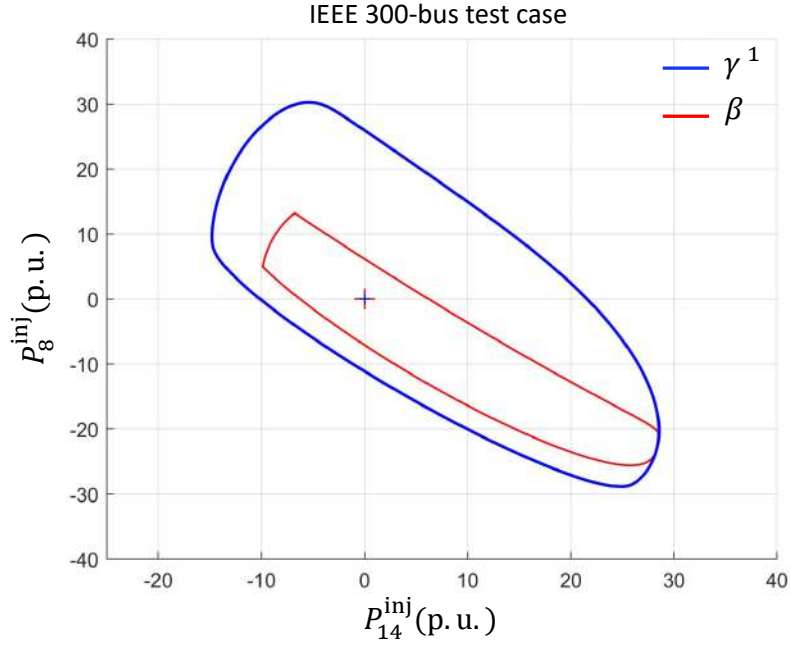
Figure 7-20: Solvability and voltage feasibility boundary in P_8^{inj} P_{14}^{inj} space, with $Q_{14}^{\text{inj}} = 0$ p.u.

in the industrialization like the construction of shipbuilders and shipyards, with an exponential rise in the agricultural urbanization. From, the context of the Asian Super Grid project, the PES will server as the connecting link with the South Korea electric grid.

7.3.5   Development plans for the Far-East

According to the investment plan in the next five years, the Primorsky region will be transformed into an industrial area. More than a hundred investment projects are scheduled, such as two shipbuilding yards, seaport terminal, several fuels, and petrochemical refineries, and two Priority Social and Economic Development Areas (PSEDA). Therefore, Primorskaya ES ought to handle the increasing load. In this section, we will check the maximum boundness on several important buses from the industrial development point of view. Examples of such buses and corresponding loads are represented in the Table.7.1.

Figure.7-22, 7-23 and 7-24 show the solvability boundary $\boldsymbol{\gamma}$, and feasibility boundary $\boldsymbol{\beta}$ (with only voltage limits on PQ buses) for the pair of buses from Table.7.1.
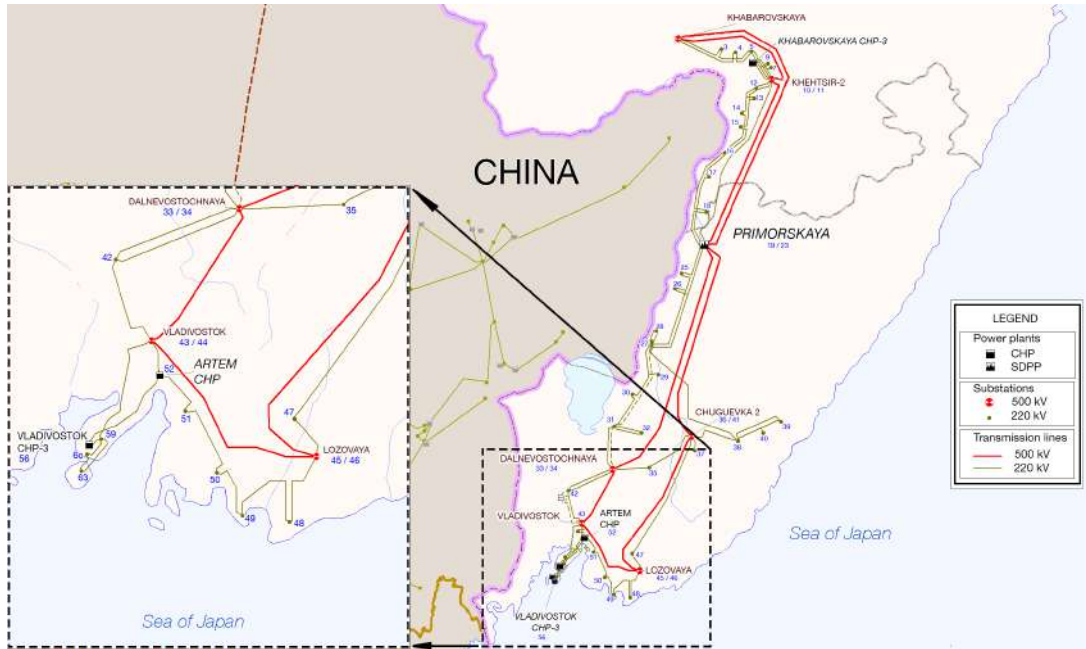
Figure 7-21: Primorskaya Energy System.

These boundaries are computed by, first finding an initial point on the solution boundary, and then the proposed spherical continuation is initiated for tracing each curve.

These boundaries are provided for given network topology and base case power injections. For a given power injection space, the area enclosed by boundary β is the feasible region, while γ encompass the infeasible region where the system can still operate. Results presented in Fig.7-22, 7-23 and 7-24 can be concluded as follow, i) System operator can avoid implementing powers that compromise the system's stability. ii) From the development context, it allows optimal placement of future loads at these pair of buses. iii) Finally, feasibility boundaries β are crucial for optimal power flow calculations.

Table 7.1: The largest upcoming scheduled power consumers

Load Name	Bus Numbers	Load, MW
Shipbuilding yard "Zvezda"	50, 51	63.1
Shipbuilding yard "Raffls"	50, 51	37.0
PSEDA "Nadezhdinskaya"	43, 44	48.1
PSEDA "Michailovskaya"	35, 42	56.7

118
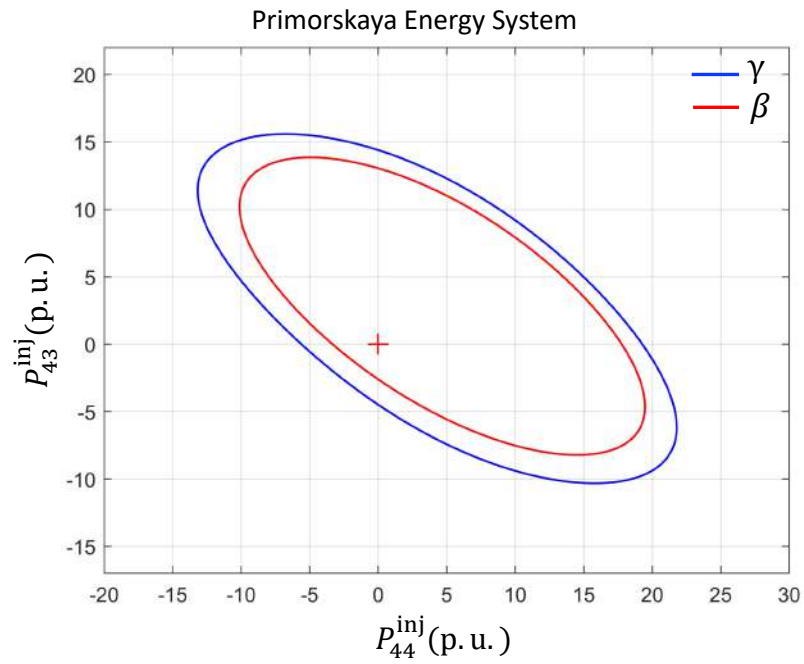
Figure 7-22: Solvability and voltage feasibility boundary in P_{43}^{inj} P_{44}^{inj} space, with $Q_{44}^{\mathrm{inj}} = 0$ p.u.
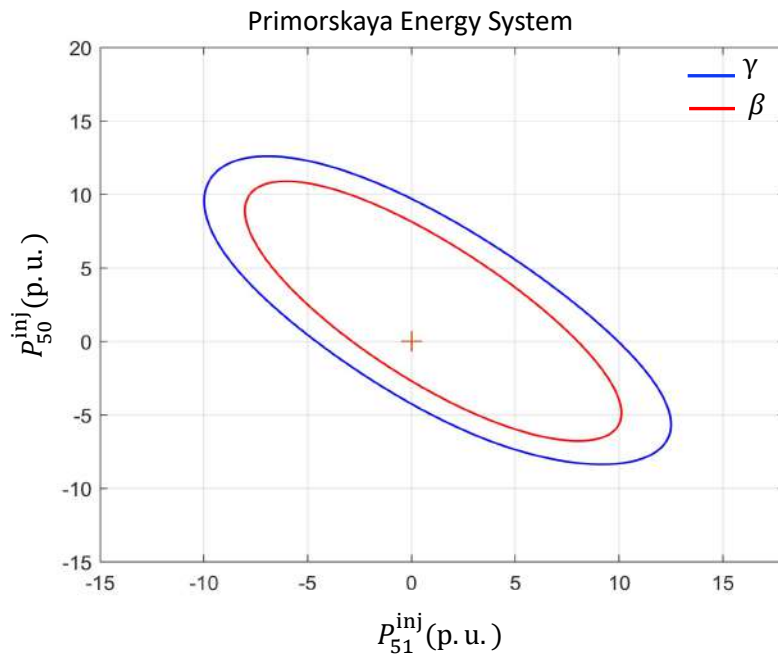
Figure 7-23: Solvability and voltage feasibility boundary in P_{50}^{inj} P_{51}^{inj} space, with $Q_{51}^{\mathrm{inj}} = 0$ p.u.
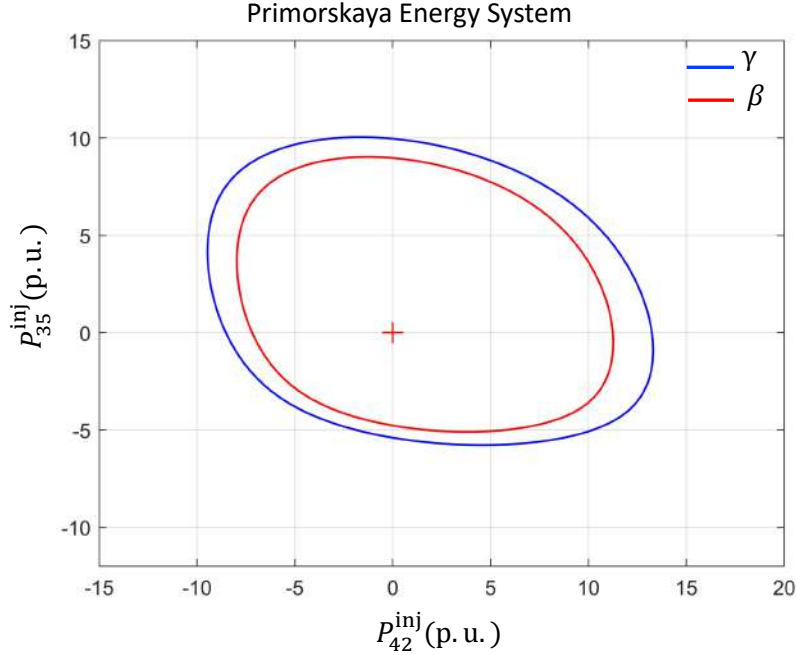
Figure 7-24: Solvability and voltage feasibility boundary in P_{35}^{inj} P_{42}^{inj} space, with $Q_{42}^{\text{inj}} = 0$ p.u.

7.3.6 Computational performance

A computational assessment is provided in this section. The time required to execute the algorithm was compared with the algorithms proposed in [13] and [84]. Several runs were performed on different IEEE cases, and an average time is listed in Table.7.2. In the table, λ_1 and λ_2 represent the pair of buses for which solvability boundaries were computed. Here t_{hc}, t_{sc} and t_{sc}^* corresponds to time for algorithms based on hyperplane continuation, spherical continuation, and the proposed spherical continuation with adaptive sphere strategy respectively.

It can also be observed that in terms of computational performance, the adaptive spherical continuation algorithm outperforms the hyperplane continuation from [13], and the traditional spherical continuation from [84]. For some test examples, the boundary curves were non-convex, and the hyperplane continuation failed to converge. Thus, an explicit adjustment was required for the continuation step length for global convergence.

Table 7.2: Computational time for different IEEE cases (full run)

IEEE cases	λ_1	λ_2	t_{hc} seconds	t_{sc} seconds	t_{sc}^* seconds
14 Bus	P_2	P_{10}	3.2	1.6	1.1
14 Bus	P_2	P_3	–	1.9	1.3
30 Bus	P_2	P_3	5.4	2.1	1.7
57 Bus	P_8	P_{10}	3.9	1.8	1.2
118 Bus	P_{103}	P_{109}	–	4.3	2.3
300 Bus	P_8	P_{14}	35.3	11.1	3.7

7.4   Summary

Numerical results illustrate the complexity of the feasibility space in multi-dimensional space. A verity of numerical examples is presented to access the computational performance of the proposed continuation procedure.

Chapter 8

Conclusions and Future Work

The knowledge of power flow solvability and voltage feasibility boundaries play a vital role in power system security analysis. Calculating such boundary curves helps in determining the robustness of operating points, assessment of system maneuverability in time, and assistance for the decision-making process for improving robustness. The computational part of calculating boundaries of power flow solution space is a challenging task, due to the non-convex structure. The complexity of the power flow feasible space is illustrated in small test network examples. The main contribution of the thesis first presents a mathematical framework for calculating just a point on the solution manifold, while the latter part focuses on constructing the solution manifold in multi-dimensional space.

The first effort of this work was to demonstrate a computationally efficient and numerically stable technique for the identification of a point on the power flow solution space. The algorithm proposed here offers several advantages in comparison to the traditional approaches to the problem. First, it allows for the natural incorporation of feasibility constraints that are usually violated before the steady-state voltage stability is compromised. Second, the algorithm is numerically stable and is based on common matrix decompositions, thus having limited computational overhead in comparison to the standard power flow analysis. Third, it avoids the need for initialization heuristic employed by algorithms that track the eigenvectors. Our numerical experiments have indicated that the algorithm compares favorably to alternatives and is characterized

by a small computational overhead even in an academic implementation. There are several possible extensions of this idea that can be explored in future studies. First, as shown in this work, there are many ways of enforcing transversality, each having a different effect on the convergence rate and overall numerical stability. But, it was observed that SVD and QR transversality conditions work better compared to other choices in the following settings: number of iterations, numerical stability, robustness, and scalability. It was also observed in our experiments, adjustment of the Newton step size α was necessary to ensure the convergence of the algorithm. Industrial-grade implementations of the algorithm require some robust step choice strategy that would provide fast convergence without operator intervention. It should be noted that actual power systems have a lot of elements that experience switching behavior as the load increases. These include generators subject to reactive power limit constraints, tap changing transformers, and others. The incorporation of this kind of behavior is critical for practical applications of the algorithm. The switching action can be naturally incorporated in algebraic formulations via additional slack variables and complementarity equations.

The later part of the thesis presents an adaptive spherical continuation algorithm for tracing power flow solution boundaries with ease of implementation, computational tractability, speed, and scalability to large networks. The mathematical framework of the algorithm uses SVD based transversality conditions to characterize the solution on the feasibility boundary due to i) small computational burden, ii) does not suffer from initialization issues like in g_{eig}, and iii) scalability for large systems. In the numerical experiments, it was observed that tracing solution boundaries is a complicated and challenging task, as these boundaries exhibit a complicated structure, plus many solution branches may exist due to the non-linear nature of the system of equations. The proposed algorithm allows us to trace such curves computationally faster, with numerical stability, ease of programmability, and finally, the scalability to large networks. The future plans include using information from these boundary curves for other potential applications such as contingency analysis, improving local optima in relaxed OPF problems, and also for transfer capability problems.

Bibliography

[1] T. P. Hughes *et al.*, "The evolution of large technological systems," *The social construction of technological systems: New directions in the sociology and history of technology*, vol. 82, 1987.

[2] M. Amin and J. Stringer, "The electric power grid: Today and tomorrow," *MRS bulletin*, vol. 33, no. 4, pp. 399–407, 2008.

[3] T. L. Vu and K. Turitsyn, "A framework for robust assessment of power grid stability and resiliency," *IEEE Transactions on Automatic Control*, vol. 62, no. 3, pp. 1165–1177, 2016.

[4] "Overview of the North American Electric Power System and Its Reliability Organizations." https://www.ferc.gov/industries/electric/indus-act/reliability/blackout/ch1-3.pdf, April 2004.

[5] T. Gönen, *Electric power distribution system engineering.* McGraw-Hill New York, 1986.

[6] GENI, "National Enegy Grid." https://www.geni.org/globalenergy/library/national_energy_grid/united-states-of-america/.

[7] D. L. Morton Jr, "Reviewing the history of electric power and electrification," *Endeavour*, vol. 26, no. 2, pp. 60–63, 2002.

[8] E. Skjong, E. Rødskar, M. M. Molinas Cabrera, T. A. Johansen, and J. Cunningham, "The marine vessel's electrical power system: From its birth to present day," 2015.

[9] J. M. Carrasco, L. García Franquelo, J. T. Bialasiewicz, E. Galván, R. C. Portillo Guisado, M. d. l. Á. Martín Prats, J. I. León, and N. Moreno-Alfonso, "Power-electronic systems for the grid integration of renewable energy sources: A survey," *IEEE Transactions on Industrial Electronics, 53 (4), 1002-1016.*, 2006.

[10] J. J. Grainger, W. D. Stevenson, W. D. Stevenson, *et al.*, *Power system analysis.* 2003.

[11] P. Kundur, N. J. Balu, and M. G. Lauby, *Power system stability and control*, vol. 7. McGraw-hill New York, 1994.

[12] K. Morison, L. Wang, and P. Kundur, "Power system security assessment," *IEEE power and energy magazine*, vol. 2, no. 5, pp. 30–39, 2004.

[13] I. A. Hiskens and R. J. Davy, "Exploring the power flow solution space boundary," *Power Systems, IEEE Transactions on*, vol. 16, no. 3, pp. 389–395, 2001.

[14] T. J. Overbye, "A power flow measure for unsolvable cases," *IEEE Transactions on Power Systems*, vol. 9, no. 3, pp. 1359–1365, 1994.

[15] D. K. Molzahn, V. Dawar, B. C. Lesieutre, and C. L. DeMarco, "Sufficient conditions for power flow insolvability considering reactive power limited generators with applications to voltage stability margins," in *Bulk Power System Dynamics and Control-IX Optimization, Security and Control of the Emerging Power Grid (IREP), 2013 IREP Symposium*, pp. 1–11, IEEE, 2013.

[16] S. Yu, H. D. Nguyen, and K. S. Turitsyn, "Simple certificate of solvability of power flow equations for distribution systems," in *Power & Energy Society General Meeting, 2015 IEEE*, pp. 1–5, IEEE, 2015.

[17] D. K. Molzahn, "Computing the feasible spaces of optimal power flow problems," *IEEE Transactions on Power Systems*, vol. 32, no. 6, pp. 4752–4763, 2017.

[18] J. Jarjis and F. Galiana, "Quantitative analysis of steady state stability in power networks," *IEEE Transactions on Power Apparatus and Systems*, no. 1, pp. 318–326, 1981.

[19] Y. V. Makarov, Z.-y. Dong, and D. J. Hill, "On convexity of power flow feasibility boundary," *Power Systems, IEEE Transactions on*, vol. 23, no. 2, pp. 811–813, 2008.

[20] D. Mehta, D. K. Molzahn, and K. Turitsyn, "Recent advances in computational methods for the power flow equations," in *2016 American Control Conference (ACC)*, pp. 1753–1765, IEEE, 2016.

[21] H. Le Nguyen, "Newton-raphson method in complex form [power system load flow analysis]," *IEEE transactions on power systems*, vol. 12, no. 3, pp. 1355–1359, 1997.

[22] V. M. da Costa, N. Martins, and J. L. R. Pereira, "Developments in the newton raphson power flow formulation based on current injections," *IEEE Transactions on power systems*, vol. 14, no. 4, pp. 1320–1326, 1999.

[23] C. Fuerte-Esquivel, E. Acha, and H. Ambriz-Perez, "A comprehensive newton-raphson upfc model for the quadratic power flow solution of practical power networks," *IEEE Transactions on power systems*, vol. 15, no. 1, pp. 102–109, 2000.

[24] C. Vournas and T. Van Cutsem, "On-line voltage security assessment," *Realtime stability in power systems*, pp. 119–146, 2006.

[25] S. C. Savulescu, *Real-time stability in power systems: techniques for early detection of the risk of blackout.* Springer, 2014.

[26] M. Ali, E. Gryazina, and K. S. Turitsyn, "Methodology for computation of online voltage stability assessment," in *2018 IEEE International Conference on Environment and Electrical Engineering and 2018 IEEE Industrial and Commercial Power Systems Europe (EEEIC/I&CPS Europe)*, pp. 1–5, IEEE, 2018.

[27] P. Kundur, J. Paserba, V. Ajjarapu, G. Andersson, A. Bose, C. Canizares, N. Hatziargyriou, D. Hill, A. Stankovic, C. Taylor, *et al.*, "Definition and classification of power system stability," *IEEE transactions on Power Systems*, vol. 19, no. 2, pp. 1387–1401, 2004.

[28] S. Kamalasadan, D. Thukaram, and A. Srivastava, "A new intelligent algorithm for online voltage stability assessment and monitoring," *International Journal of Electrical Power & Energy Systems*, vol. 31, no. 2-3, pp. 100–110, 2009.

[29] G. Morison, B. Gao, and P. Kundur, "Voltage stability analysis using static and dynamic approaches," *IEEE transactions on Power Systems*, vol. 8, no. 3, pp. 1159–1171, 1993.

[30] T. Van Cutsem and C. Vournas, *Voltage Stability of Electric Power Systems.* Kluwer (Springer), 1998.

[31] S. Abe, Y. Fukunaga, A. Isono, and B. Kondo, "Power system voltage stability," *IEEE Transactions on Power Apparatus and Systems*, no. 10, pp. 3830–3840, 1982.

[32] V. Ajjarapu, *Computational techniques for voltage stability assessment and control.* Springer Science & Business Media, 2007.

[33] V. Ajjarapu and C. Christy, "The continuation power flow: a tool for steady state voltage stability analysis," *Power Systems, IEEE Transactions on*, vol. 7, no. 1, pp. 416–423, 1992.

[34] F. Milano, "Continuous newton's method for power flow analysis," *IEEE Transactions on Power Systems*, vol. 24, no. 1, pp. 50–57, 2008.

[35] S. D. Rao, D. J. Tylavsky, and Y. Feng, "Estimating the saddle-node bifurcation point of static power systems using the holomorphic embedding method," *International Journal of Electrical Power & Energy Systems*, vol. 84, pp. 1–12, 2017.

[36] C. Gómez-Quiles, A. Gómez-Expósito, and W. Vargas, "Computation of maximum loading points via the factored load flow," *IEEE Transactions on Power Systems*, vol. 31, no. 5, pp. 4128–4134, 2016.

[37] S. Chandra, D. Mehta, and A. Chakrabortty, "Locating power flow solution space boundaries: A numerical polynomial homotopy approach," *arXiv preprint arXiv:1704.04792*, 2017.

[38] C. A. Canizares and F. L. Alvarado, "Point of collapse and continuation methods for large AC/DC systems," *Power Systems, IEEE Transactions on*, vol. 8, no. 1, pp. 1–8, 1993.

[39] A. J. Flueck, H.-D. Chiang, and K. S. Shah, "Investigating the installed real power transfer capability of a large scale power system under a proposed multi-area interchange schedule using CPFLOW," *Power Systems, IEEE Transactions on*, vol. 11, no. 2, pp. 883–889, 1996.

[40] M. H. Gravener and C. Nwankpa, "Available transfer capability and first order sensitivity," *Power Systems, IEEE Transactions on*, vol. 14, no. 2, pp. 512–518, 1999.

[41] A. M. Kontorovich, A. V. Kryukov, and Y. V. Makarov, *Methods of stability indices computations for complicated power systems*. House of the Irkutsk University, 1988.

[42] A. Gómez-Expósito, A. J. Conejo, and C. Cañizares, *Electric energy systems: analysis and operation*. CRC Press, 2016.

[43] F. Milano, *Power system modelling and scripting*. Springer Science & Business Media, 2010.

[44] A. Trias, "The Holomorphic Embedding Load Flow method," *Power and Energy Society General Meeting, 2012 IEEE*, pp. 1–8, 2012.

[45] B. I. Ayuev, V. V. Davydov, and P. M. Erokhin, "Fast and reliable method of searching power system marginal states," *IEEE Transactions on Power Systems*, vol. 31, pp. 4525–4533, Nov 2016.

[46] R. J. Avalos, C. A. Cañizares, F. Milano, and A. J. Conejo, "Equivalency of continuation and optimization methods to determine saddle-node and limit-induced bifurcations in power systems," *IEEE Transactions on Circuits and Systems I: Regular Papers*, vol. 56, no. 1, pp. 210–223, 2009.

[47] J. Lavaei and S. H. Low, "Zero Duality Gap in Optimal Power Flow Problem," *Power Systems, IEEE Transactions on*, vol. 27, no. 1, pp. 92–107, 2012.

[48] D. K. Molzahn, B. C. Lesieutre, and C. L. DeMarco, "A Sufficient Condition for Power Flow Insolvability With Applications to Voltage Stability Margins," *Power Systems, IEEE Transactions on*, vol. 28, no. 3, pp. 2592–2601, 2013.

[49] N. G. Sakellaridis, M. E. Karystianos, and C. D. Vournas, "Local and global bifurcations in a small power system," *International Journal of Electrical Power & Energy Systems*, vol. 33, no. 7, pp. 1336–1347, 2011.

[50] S. Bolognani and S. Zampieri, "On the Existence and Linear Approximation of the Power Flow Solution in Power Distribution Networks," *Power Systems, IEEE Transactions on*, no. 99, pp. 1–10, 2015.

[51] C. Wang, A. Bernstein, J. Y. L. Boudec, and M. Paolone, "Explicit conditions on existence and uniqueness of load-flow solutions in distribution networks," *IEEE Transactions on Smart Grid*, vol. PP, no. 99, pp. 1–1, 2016.

[52] C. D. Vournas, M. Karystianos, and N. Maratos, "Bifurcation points and loadability limits as solutions of constrained optimization problems," in *2000 Power Engineering Society Summer Meeting (Cat. No. 00CH37134)*, vol. 3, pp. 1883–1888, IEEE, 2000.

[53] M. E. Karystianos, N. G. Maratos, and C. D. Vournas, "Maximizing power-system loadability in the presence of multiple binding complementarity constraints," *IEEE Transactions on Circuits and Systems I: Regular Papers*, vol. 54, no. 8, pp. 1775–1787, 2007.

[54] Y. V. Makarov, D. J. Hill, and Z.-Y. Dong, "Computation of bifurcation boundaries for power systems: a new/spl delta/-plane method," *IEEE Transactions on Circuits and Systems I: Fundamental Theory and Applications*, vol. 47, no. 4, pp. 536–544, 2000.

[55] D. Mehta, H. D. Nguyen, and K. Turitsyn, "Numerical polynomial homotopy continuation method to locate all the power flow solutions," *IET Generation, Transmission & Distribution*, vol. 10, no. 12, pp. 2972–2980, 2016.

[56] M. Ali, A. Dymarsky, and K. Turitsyn, "Transversality enforced newton raphson algorithm for fast calculation of maximum loadability," *IET Generation, Transmission & Distribution*, 2017.

[57] O. I. Elgerd, "Electric energy systems theory: an introduction," 1982.

[58] H. Saadat *et al.*, *Power system analysis*, vol. 50. MCGRAW-HILL, 1999.

[59] J. E. Tate and T. J. Overbye, "A comparison of the optimal multiplier in polar and rectangular coordinates," *Power Systems, IEEE Transactions on*, vol. 20, no. 4, pp. 1667–1674, 2005.

[60] M. Ali, E. Gryazina, and K. S. Turitsyn, "Fast calculation of the transfer capability margins," in *2019 IEEE Milan PowerTech*, pp. 1–6, IEEE, 2019.

[61] R. Bacher, "Power system models, objectives and constraints in optimal power flow calculations," in *Optimization in planning and operation of electric power systems*, pp. 217–263, Springer, 1993.

[62] I. Dobson and L. Lu, "Voltage collapse precipitated by the immediate change in stability when generator reactive power limits are encountered," *IEEE Transactions on Circuits and Systems I: Fundamental Theory and Applications*, vol. 39, no. 9, pp. 762–766, 1992.

[63] S. Iwamoto and Y. Tamura, "A load flow calculation method for ill-conditioned power systems," *Power Apparatus and Systems, IEEE Transactions on*, no. 4, pp. 1736–1743, 1981.

[64] V. Ajjarapu and C. Christy, "The continuation power flow: a tool for steady state voltage stability analysis," *Power Systems, IEEE Transactions on*, vol. 7, pp. 416–423, Feb. 1992.

[65] J. P. Abbott, "An efficient algorithm for the determination of certain bifurcation points," *Journal of Computational and Applied Mathematics*, vol. 4, no. 1, pp. 19–27, 1978.

[66] G. Moore and A. Spence, "The calculation of turning points of nonlinear equations," *SIAM Journal on Numerical Analysis*, vol. 17, no. 4, pp. 567–576, 1980.

[67] A. Griewank and G. W. Reddien, "Characterization and computation of generalized turning points," *SIAM journal on numerical analysis*, vol. 21, no. 1, pp. 176–185, 1984.

[68] T. F. Chan, "On the existence and computation of lu-factorizations with small pivots," *Mathematics of computation*, vol. 42, no. 166, pp. 535–547, 1984.

[69] Y. Saad and H. A. Van Der Vorst, "Iterative solution of linear systems in the 20th century," *Journal of Computational and Applied Mathematics*, vol. 123, no. 1, pp. 1–33, 2000.

[70] T. A. Davis, "Algorithm 915, suitesparseqr: Multifrontal multithreaded rank-revealing sparse qr factorization," *ACM Transactions on Mathematical Software (TOMS)*, vol. 38, no. 1, p. 8, 2011.

[71] L. N. Trefethen and D. Bau III, *Numerical linear algebra*, vol. 50. Siam, 1997.

[72] P. Löf, T. Smed, G. Andersson, and D. Hill, "Fast calculation of a voltage stability index," *Power Systems, IEEE Transactions on*, vol. 7, no. 1, pp. 54–64, 1992.

[73] G. H. Golub and C. F. Van Loan, *Matrix computations*, vol. 3. JHU Press, 2012.

[74] R. D. Zimmerman, C. E. Murillo-Sanchez, and R. J. Thomas, "MATPOWER: Steady-state operations, planning, and analysis tools for power systems research and education," *Power Systems, IEEE Transactions on*, vol. 26, no. 1, pp. 12–19, 2011.

[75] R. Christie, "Power systems test case archive," *Electrical Engineering dept., University of Washington*, 2000.

[76] M. Ali, "Matlab Implementation of TENR Algorithm." `https://github.com/mazharalipak/TENR$\_\mathrm{Final}$`, 2017.

[77] G. Irisarri, X. Wang, J. Tong, and S. Mokhtari, "Maximum loadability of power systems using interior point nonlinear optimization method," *IEEE transactions on Power Systems*, vol. 12, no. 1, pp. 162–172, 1997.

[78] P. W. Sauer, B. Lesieutre, and M. Pai, "Maximum loadability and voltage stability in power systems," *International Journal of Electrical Power & Energy Systems*, vol. 15, no. 3, pp. 145–153, 1993.

[79] F. Milano, "An open source power system analysis toolbox," *IEEE Transactions on Power systems*, vol. 20, no. 3, pp. 1199–1206, 2005.

[80] S. Greene, I. Dobson, and F. L. Alvarado, "Sensitivity of transfer capability margins with a fast formula," *IEEE Transactions on Power Systems*, vol. 17, no. 1, pp. 34–40, 2002.

[81] G. C. Ejebe, J. Tong, J. Waight, J. Frame, X. Wang, and W. Tinney, "Available transfer capability calculations," *IEEE Transactions on Power systems*, vol. 13, no. 4, pp. 1521–1527, 1998.

[82] I. Dobson, S. Greene, R. Rajaraman, C. L. DeMarco, F. L. Alvarado, M. Glavic, J. Zhang, and R. Zimmerman, "Electric power transfer capability: concepts, applications, sensitivity and uncertainty," *PSERC Publication*, no. 01-34, 2001.

[83] E. L. Allgower and K. Georg, *Numerical continuation methods*, vol. 33. Springer-Verlag Berlin, 1990.

[84] K. Yamamura, "Simple algorithms for tracing solution curves," *IEEE Transactions on Circuits and Systems I: Fundamental Theory and Applications*, vol. 40, no. 8, pp. 537–541, 1993.

[85] D. Torres-Muñoz, L. Hernandez-Martinez, and H. Vázquez-Leal, "Spherical continuation algorithm with spheres of variable radius to trace homotopy curves," *International Journal of Applied and Computational Mathematics*, vol. 2, no. 3, pp. 421–433, 2016.

[86] J. M. Oliveros-Muñoz and H. Jiménez-Islas, "Hyperspherical path tracking methodology as correction step in homotopic continuation methods," *Chemical Engineering Science*, vol. 97, pp. 413–429, 2013.

[87] R. Seydel, "Numerical computation of branch points in nonlinear equations," *Numerische Mathematik*, vol. 33, no. 3, pp. 339–352, 1979.